Utrecht University
Faculty of Physics

The development of a GEANT based Monte Carlo simulation framework for the R&D process of the FoCal calorimeter

Peter-Jan Blenkers
August 30, 2012

Supervisor: Prof. Dr. T.Peitzmann
Institute of Subatomic Physics

Abstract

In this thesis the development of a general simulation framework for particle detectors based on the GEANT3 software is described. This framework consists of multiple C++ classes and running scripts containing the different functionalities of the framework. Several basic user interfaces were constructed to allow for a relatively simple manipulation of the detector geometry, the detection chip pixel structure and the primary particles.

The description of the simulation framework is followed by several consistency checks of said framework in order to establish the reliability of the simulation results in the context of the FoCal project. More specifically the FoCal prototype geometry was implemented in several electromagnetic shower simulations. The results of these simulations were used to investigate features of the FoCal detector like the sampling fraction, the electromagnetic shower shape and the energy deposition in thin silicon layers. Subsequently a comparison of these features to theoretical predictions was made as a consistency check of the simulation framework. Finally simulation results on the total response and energy resolution of the FoCal prototype are presented.

Contents

1. Introduction

1.1 Calorimetry in particle physics

Particle physics is the field in physics that studies the constituents of matter and their interactions at the most fundamental level. This kind of investigation requires the detection of extremely small particles and their properties in order to obtain an insight in the physics processes that rule the structure of matter at this low level. The methods that are applied in this field have undergone significant alterations in the last 70 years. The earliest experiments that can be considered the origin of modern particle physics were the studies on cosmic rays. Though still conducted today the focus of particle physics has shifted from these cosmic ray experiments to accelerator based experiments. The application of accelerators provided a more controlled environment for the experiments. In addition the accelerators allowed much higher rates of data acquisition, which was essential as the processes of interest became more and more rare and high amounts of statistics were needed to distinguish them amongst a rich variety of other physical mechanisms.

The physical processes under investigation in particle experiments are reconstructed from the created particles and their momenta in individual events. In the early days bubble chambers were used for the determination of these quantities, however as the processes under investigation became more exotic and statistics increased the bubble chamber was no longer an efficient way of extracting the data from the event primarily because of the time it took to analyze the pictures by hand. To overcome this problem wire chambers and shower counters were introduced to respectively track the charged particles in a magnetic field and absorb and measure the energy of neutral reaction products. Though the accuracy of the data acquired by these methods was by far inferior to that of the bubble chamber pictures the high frequency at which this data could be processed was a decisive advantage.

As accelerators became increasingly powerful the application of shower counters or calorimeters as they are called today took a flight. The main reason for this was the high energy resolution of calorimeters for high energy particles, while the determination of the momentum of particles by tracking them in a magnetic field becomes increasingly difficult at high energies since the curvature of the tracks is diminished. Also the combination of the tracking data with the calorimeter data allowed for the identification of certain particles, which is one of the main purposes of particle detection in the first place. This way calorimetry consolidated its position as an essential tool in high energy particle experiments.

1.2 Calorimetric methods

The primary purpose of a calorimeter is the energy measurement of particles traversing its structure. In calorimetry there are several physical processes that enable these measurements. It is important at this point to differentiate between so called electromagnetic calorimeters and the hadronic calorimeters. Electromagnetic calorimeters are optimized for energy measurement of leptons (mainly electrons and positrons) and photons. The showers caused by these particles are fully described by QED and well understood. The more involved hadronic showers that occur in hadronic calorimeters are only partially described by QED since the strong interaction plays an important role there. The effects that are described in the next paragraph describe the functionality of most electromagnetic calorimeters while being only a small part of the story for hadronic calorimeters.

First of all the so called scintillation process can be used to detect charged particles. One of the processes by which these particles lose their energy when traversing matter is the excitation of atoms or molecules of the medium. These excitations are caused by electromagnetic interactions of the charged particles with the charged constituents of the medium. When the excited particles return to their ground state photons are emitted. This process is referred to as scintillation if the emitted photons are in the visible part of the spectrum. Subsequently the photons present in the medium are converted to an electrical signal using a photomultiplier tube. Scintillators are used to great extent for they are relatively cheap and can be read out at high frequencies.

Upon entering a certain medium it is also possible for a charged particle to exceed the speed of light in that medium. If this scenario occurs the particle will lose energy by radiating photons. This radiation is called Cerenkov radiation and can be used to determine the velocity of the traversing particle. This process is instantaneous and thus even faster then the scintillation process, that depends on the lifetime of the excited states, offering ultimate readout speeds.

A third process by which charged particles can lose energy in a material that is of direct use for detection purposes is energy loss through ionization of the medium. In addition to exciting the atoms or molecules of the medium a traversing particle can ionize these constituents through electromagnetic interactions. In calorimeters that employ gasses or liquids as ionizing medium these electrons can then be separated from the ions by applying an electric field. Next the electrical signal caused by the charge collection at the electrodes will be proportional to the number of freed electrons and hence be a measure of the energy deposition in the medium. Semiconductors can also be applied as a solid ionizing medium. In these detectors the electrons are excited from the valence band into the conduction band. Once in the conduction band they are transported to the cathode under the influence of an electric field yielding an electrical signal.

1.3 Electromagnetic showers

The main goal of this thesis is the simulation of electromagnetic showers in a specific new type of calorimeter. Therefore the basics of electromagnetic shower development are concisely considered in this section. The constituents of an electromagnetic shower are photons, electrons and positrons. The electromagnetic processes responsible for their energy loss in a material are the following.

1.3.1 Electron and positron energy loss processes

When electrons or positrons with energy of several tens of MeV's get decelerated by the Coulomb fields of the atoms in a medium they will emit photons. The majority of these photons is very soft. This radiation is known as bremsstrahlung and is the main energy loss mechanism for charged particles at high energies. The screening of the nuclear electric fields by the electron clouds in a material is an important parameter influencing this phenomenon.

At lower energies charged particles are more likely to ionize the atoms of the medium. The ionization of the atoms is caused by electromagnetic interactions of the charged particles and the electrons in the outer shells of the atom. This effect depends strongly on the electron density Z of the medium and the mass of the charged particle. The Bethe-Bloch formula accurately describes the energy loss of charged particles due to ionization. However this formula does not directly apply to electrons or positrons as a consequence of their relatively low mass. Ionization is also the process through which the majority of the energy is eventually deposited in the material, since high numbers of low energy electrons and positrons are produced by the other processes in a shower. Note that the energy transfer in this scenario is only very small. Ionization resulting in free electrons with a higher energy is also possible and is called Bhabha scattering or Møller scattering for respectively positrons or electrons. The energy loss through these two mechanisms is however very small compared to the regular ionization losses. Figure 1 shows the relative size of the different energy loss processes for electrons and positrons.

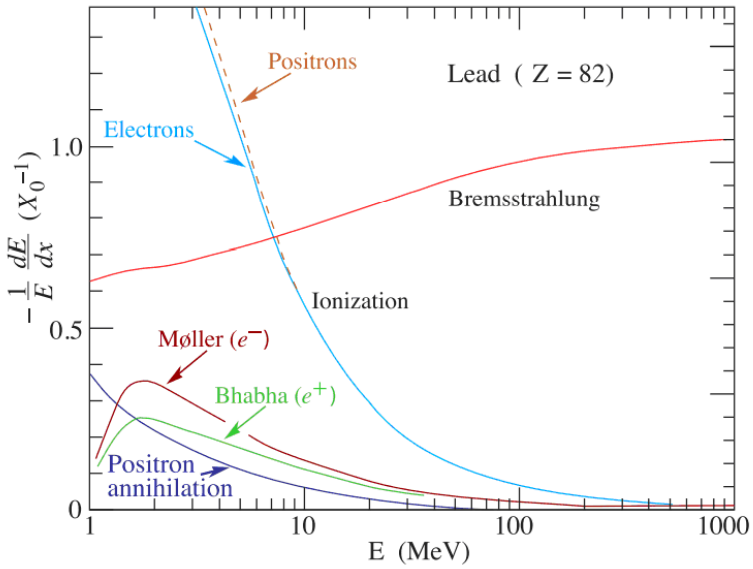

Figure 1: Fractional energy loss per radiation length due to the processes relevant to electrons and positrons

1.3.2 Photon energy loss processes

Photons with energy below one MeV can be absorbed by the atoms of a medium followed by the emission of an electron. The electron subsequently loses its energy through ionization processes. As the vacancies in the lower shells caused by the electron emission are neutralized by electrons from higher shells X-rays and Auger electrons will be emitted. This is called the photo-electric effect.

Photons with energy between approximately one and ten MeV depending on the material can scatter off atomic electrons causing the electrons to be ejected from their atom. The energy transfer of the photon to the electron is substantial and the electron will thereafter lose its energy again by ionization. This process is called Compton scattering.

High energy photons above roughly ten MeV primarily lose their energy through pair production. In this process the photon is converted to an electron positron pair. This reaction is triggered by the interaction of the photon with the coulomb field of the atoms in a medium. This interaction is essential since it allows for momentum conservation and without it pair production does not occur.

1.3.3 Other energy loss processes

Instead of ionizing the constituents of a medium a traversing particle can merely excite the atoms in the material. This process generates photons that will in general be absorbed in photo-electric processes. However in specific transparent materials under the right conditions these photons can be collected directly as is the case for scintillators. As previously mentioned the emission of Cerenkov radiation by charged particles is also an

option at high energies, however the energy loss through this process is orders of

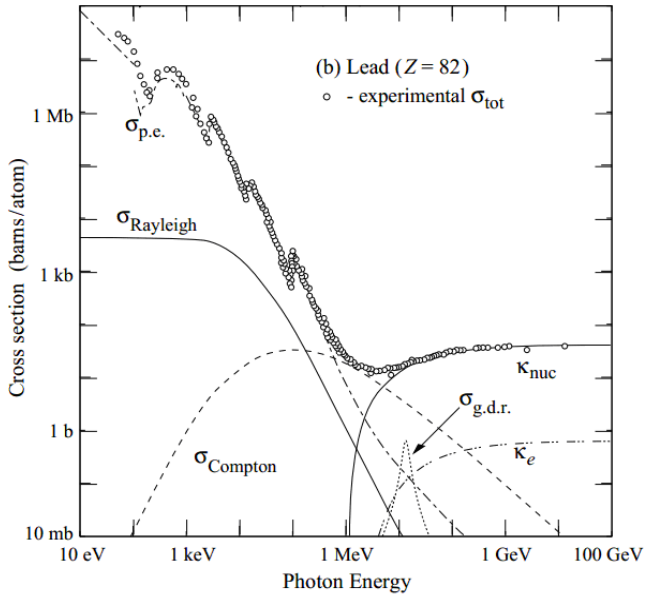

Figure 2: Cross section of the physical processes relevant to photons

magnitude smaller then the other effects. In addition at high energies δ-rays can be produced. These consist of electrons that have been struck from their atoms at high energies. Finally at extremely high energies the electromagnetic interactions of charged particles with the nuclei might induce nuclear reactions. There exist so called compensating calorimeters that use this phenomenon however in most materials the occurrence probability of this class of effects is extremely slim in the relevant energy regime. Figure 2 shows the cross section of the different energy loss mechanisms for photons. In this figure also the cross section for Rayleigh scattering is depicted. This process is however the elastic scattering of photons of the constituents of the medium, so technically speaking it is not an energy loss mechanism however it does influence the spatial development of the shower.

1.4 Shower development

In the early phases of an electromagnetic shower the electrons and positrons radiate off large numbers of mainly soft photons that are subsequently absorbed through the photo-electric effect and Compton scattering. The photons with enough energy on the other hand will produce electron positron pairs that in turn emit bremsstrahlung photons. Through these two mechanisms the number of particles in the shower increases exponentially and this increasing number of photons, electrons and positrons travelling through the material is referred to as an electromagnetic cascade or shower. The particle multiplication continues until the average energy of the charged shower particles reaches values were they lose approximately the same amount of energy through ionization as through radiation. At these energies the photons are also more likely to free one electron

through Compton or photo-electric interactions then to produce an electron positron pair. From this point on the ionization process takes over and bremsstrahlung and pair production are diminished. The low energy photons are absorbed as described earlier and the low energy positrons annihilate with atomic electrons generating more relatively low energy photons.

1.5 Detector properties

Finally there are several important concepts that need to be introduced. These concepts are used later on to describe the shower characteristics in an approximately material independent way. This is useful for comparison purposes, since the development of electromagnetic showers depends strongly on the atomic number of the involved materials.

1.5.1 Radiation length

The radiation length is the distance over which a high energy (E>1GeV) electron or positron loses 63.2% (i.e. 1-e^{-1}) of its energy to bremsstrahlung [1]. This definition is based on high energy electrons or positrons since at these energies the losses due to ionization are negligible. The radiation length depends largely on the Z-value of a material. As the Z-value increases the electron density rises and the radiation cross section grows with it. This causes higher bremsstrahlung emission resulting in a shorter radiation length. The expression for the radiation length of a mixture of materials is

$$\frac{1}{X_0} = \sum_i V_i / X_i \tag{1.1}$$

where V_i and X_i are respectively the volume fraction and the radiation length of the different materials that constitute the mixture. This formula is very useful in the description of sampling calorimeters that consist of alternating active and passive layers of different materials. It is also called the effective radiation length. Thus for the FoCal detector the effective radiation length is calculated as follows

$$\frac{1}{X_0} = \frac{V_w}{X_w} + \frac{V_{si}}{X_{si}} + \frac{V_{cu}}{X_{cu}} = \frac{0.87}{3.5mm} + \frac{0.04}{93.6mm} + \frac{0.01}{14.3mm} \tag{1.2}$$

The contribution of the air gap, glue layer and fibreglass layers are neglected, for their contribution is very small. Concluding the effective radiation length of FoCal is 4.0mm.

1.5.2 Critical Energy

The critical energy of a certain material is defined as the energy at which the ionization loss per radiation length equals the electron energy [1].

$$(\Delta E)_{ion} = \left[\frac{dE}{dx}\right]_{ion} X_0 = E \tag{1.3}$$

This definition is based on the behaviour of electrons and is therefore primarily relevant in the context of electromagnetic showers. So at this energy the ionization and radiation losses are roughly equal. Moreover this implies that as the energy of an electron or positron falls below the critical energy the particle is more likely to lose its energy through ionization then through the emission of radiation. Therefore the charged particles in the electromagnetic shower will no longer cause a multiplication of particles. Furthermore for high-Z materials below the critical energy the photons are more likely to lose their energy due to the photo-electric effect then through Compton scattering. So also the photons will stop contributing to the increasing particle multiplicity. Summarizing as the average energy of the shower particles reaches the critical energy the particle multiplicity levels out and the shower reaches its maximum. As Z increases the electron density in the associated material increases as well. This induces a rise in the bremsstrahlung cross section that is much more pronounced than the increase of the ionization cross section. This causes the critical energy to diminish, since the particles will lose their energy mainly due to radiation till lower energies.

1.5.3 Molière radius

Where the radiation length is an important scaling variable for the longitudinal shower characteristics the Molière radius is a scaling variable that deals with the transversel shower development. It is defined as [1]

$$\rho_M = E_s \frac{X_0}{\varepsilon_c} \tag{1.4}$$

with E_s the scale energy, defined as

$$E_s = m_e c^2 \sqrt{4\pi/\alpha} = 21.2\text{MeV} \tag{1.5}$$

On average 90% of the shower energy is deposited in a cylinder with radius ρ_M around the shower axis. The Moliere radius for a mixture of materials is calculated in the same manner as the radiation length. So the Molière radius of FoCal becomes

$$\frac{1}{\rho_M} = \frac{V_w}{\rho_{M,w}} + \frac{V_{si}}{\rho_{M,si}} + \frac{V_{cu}}{\rho_{M,cu}} = \frac{0.87}{9.3mm} + \frac{0.04}{48mm} + \frac{0.01}{15.2mm}$$

The contribution of the air gap, glue layer and fibreglass layers are neglected, for their contribution is very small. Concluding the effective Molière radius of FoCal is 10.5mm. The

Molière radius is much less Z dependent then the radiation length, since an increase in Z diminishes both the radiation length and the critical energy. The definition of the Molière radius can be derived from the average angular deflection by Coulomb scattering at the critical energy.

1.6 Monte Carlo simulations

When designing an electromagnetic calorimeter particle physicists want to optimize all aspects relevant to its performance. In this process a thorough understanding of the shower development in their proposed designs is of utmost importance. Analytical calculations of average shower behaviour is not sufficient for this purpose since aspects like the energy or position resolution depend strongly on fluctuations between individual events. Luckily the physical processes involved in electromagnetic showers are very well understood and described by QED. Therefore computer simulations can be implemented in the design process or even to get an insight in the inner workings of electromagnetic showers themselves. A tremendous advantage of the computer models in the design process is the relative ease with which different kinds of geometries can be tested and adjusted. This is something that would be very costly and time consuming to do with real prototypes.

In a Monte Carlo simulation the particles are transported through the different media constituting the geometry in small steps. Each step the probability on the occurrence of one of the relevant physical processes is calculated and given this probability distribution a process is picked randomly. This way it's possible to obtain consistent and accurate results at least for electromagnetic showers by averaging over about a thousand events. The major limitation of these simulations is caused as with all computer models by the available simulation time. As showers develop the number of particles to be transported can reach numbers on the order 10^6 for 100GeV electromagnetic showers. This number of particles is strongly related to the energy tracking cut off values. These parameters determine the minimal energy till which particles are tracked. When these cut off values are lowered by a factor of 10 the number of particles roughly increases by a factor of 10 dramatically extending the necessary simulation time.

Common simulation packages for em-showers are codes like FLUKA, GEANT and EGS4. The simulations described in this thesis were all conducted in GEANT3, because of its accessible interface for handling geometries and its convenient interfaces in the ROOT data analysis framework.

1.7 Focal

Focal is the name of the proposed forward electromagnetic calorimeter to be added to the existing ALICE detectors. The main goals of this specific detector will be:

- measuring neutral pions and photons to study particle yields and correlations in the

high rapidity range 2.5<η<4.5 and in a large transverse momentum range, in order to study possible gluon saturation effects.
- the measurement of direct photons and jets from parton-parton scattering to be used in gamma-jet correlation studies of jet quenching effects.
- the measurement of thermal photons of the hypothetical QGP state for elliptic flow studies.
- the general improvement of ALICE detection capabilities of photons and neutral hadrons in the high rapidity range.

1.7.1 Physics motivation

The parton density function or PDF of the proton and larger nuclei is an important tool in nuclear collision research. For protons the PDF's of the quarks are pretty well known however for gluons there is some ambiguity. According to perturbative QCD the PDF increases dramatically with the decrease of the momentum fraction (x) of the gluon. However this increase cannot continue indefinitely since the total cross section for the strong interaction is known to be finite in proton-nucleus scattering while an ever increasing number of gluons with a finite cross section would render the total cross section infinite. This fact combined with the theoretical prediction that non-linear QCD effects like gluon fusion will start to play a role at high gluon densities led to the conclusion that a global maximum of the gluon PDF at a certain small value of x has to exist. This effect is referred to as gluon saturation. In addition a thorough knowledge on the exact nature of the PDF's and with that the initial state of the particles in any experiment is of utmost importance to the interpretation of particle yields and other observables.
The following reasoning shows how FoCal allows ALICE to access the low x-values in a broad p_T range where the saturation effect is likely to occur. As the rapidity increases at any given p_T value the reaction products of parton-parton scattering at increasingly low x-values are considered. At these lower x-values the parton density will increase and the gluon cross section needed to accomplish saturation is diminished. Since this cross section is proportional to $1/Q^2$ it is possible at this higher rapidity to use higher Q^2 values effectively increasing the p_T range for which saturation effects should be present. Thus FoCal would greatly enhance ALICE's low x capabilities by measuring at high rapidities. This is also why FoCal stands for Forward Calorimeter.

If the gluon saturation effect is indeed present it is expected to manifest itself in one of the following ways.

- a suppression of the particle yields in comparison to the perturbative QCD expectations simply through the absence of an increasing number of gluons available for parton-parton scattering processes.
- a decrease of the correlation between direct and recoiling jets from parton-parton scattering.

Signs of these two effects have already been detected at RHIC, however, the p_T range over which the effects are measured is considered too small to exclusively point to the gluon

saturation effect as explanation. The effects should be more pronounced at LHC because of its higher rapidity coverage probing even lower x and its higher centre of mass energy extending the saturation zone towards higher p_T.

The simplest way of conducting the low x measurements is by using single hadrons. The hadron production process however is strongly influenced by secondary processes. Hadron jets can be used to reduce this uncertainty; however these are only formed at high Q^2, which is of no use to saturation investigations. The solution to this inherent problem is the use of direct photons. These photons will not interact as strongly with the surrounding quarks and gluons as the hadrons and can hopefully be detected at much lower Q^2. Therefore photons are considered much better candidates for small x probing purposes. It's important to note here that the majority of the photons originates from the fragmentation process of high energy hadrons, nevertheless by applying stringent isolation cuts this source of uncertainty can be suppressed.

In Pb-Pb collisions at LHC a so called quark gluon plasma is believed to occur. The quark gluon plasma is a state in which the quarks are no longer bound to their hadron but can roam around the volume of the QGP freely, due to the extremely high hadron densities reached in these collisions. An indication of the presence of a QGP is believed to be the suppression of jets in comparison to pp-collisions due to secondary strong interactions of the jets with the QGP upon traversal. This effect is called jet quenching. One of the ways in which this effect is investigated is the through gamma-jet correlations. In specific first order parton-parton scattering processes a parton and photon are created with opposite p_T. The photon can traverse the QGP relatively unharmed since it's not strongly interacting while the jet causes by the parton might be suppressed in the presence of a QGP. The great photon measurement capabilities of FoCal will now offer opportunities in the field of these gamma-jet correlation studies.

In high energy decentral heavy-ion collisions the volume in which the two nuclei interact is elliptically shaped. Each individual scattering event produces its reaction products in an isotropic manner. It turns out however that the flow of energy, momentum and particle multiplicities is not isotropic in the plane perpendicular to the beam line, but rather elliptically proportioned. This effect is called elliptic flow and is considered to be strong evidence for the existence of the quark gluon plasma in which hydrodynamic behaviour causes the observed anisotropy. The initial conditions imposed on the models that exist for this effect strongly influence the predictions of these models. Therefore a thorough knowledge of the PDF's is essential to the adequate interpretation of elliptic flow. Furthermore the measurement of direct thermal photons of the QGP is a very interesting subject given that recent discoveries indicate a substantial difference between the flow of these photons and for example pions.

1.7.2 Current design

Summarizing the last section FoCal should be capable of the performing the following tasks:

- measurement of direct photons and jets from parton-parton scattering for jet quenching studies
- measurement thermal photons for elliptic flow studies
- distinguishing neutral pions and photons in a large transverse momentum range for saturation studies as well as for the other studies

The most important requirement that is imposed by these conditions is a high granularity. In the first place high granularity will allow for better isolation cuts. These isolation cuts are needed to distinguish between the direct and fragmentation photons and are therefore essential to the first two tasks mentioned above. Secondly the high p_T ranges required for the third task imply high overall momenta of the involved photons and hadrons. At these high energies the opening angle of the characteristic two photon decay of neutral pions becomes very small. In order to distinguish such a gamma pair from a single photon also high spatial resolution is needed.

Other important requirements of course involve the rapidity range that is accessible to FoCal. This range depends strongly on the distance between the interaction point and the detector given the beam pipe has a fixed diameter. At a given perpendicular distance from the beam line an increase in distance to the interaction point directly implies a rapidity increase. For FoCal still two scenarios are envisioned by the ALICE collaboration. The first one being a single detector at approximately 3.5m from the interaction point covering a rapidity range from 2.5 to 4.3. While the second option would be to locate the detector approximately 8m from the interaction point effectively covering a rapidity range up to 5.0. This scenario however would imply modifications to existing structures while the first scenario does not.

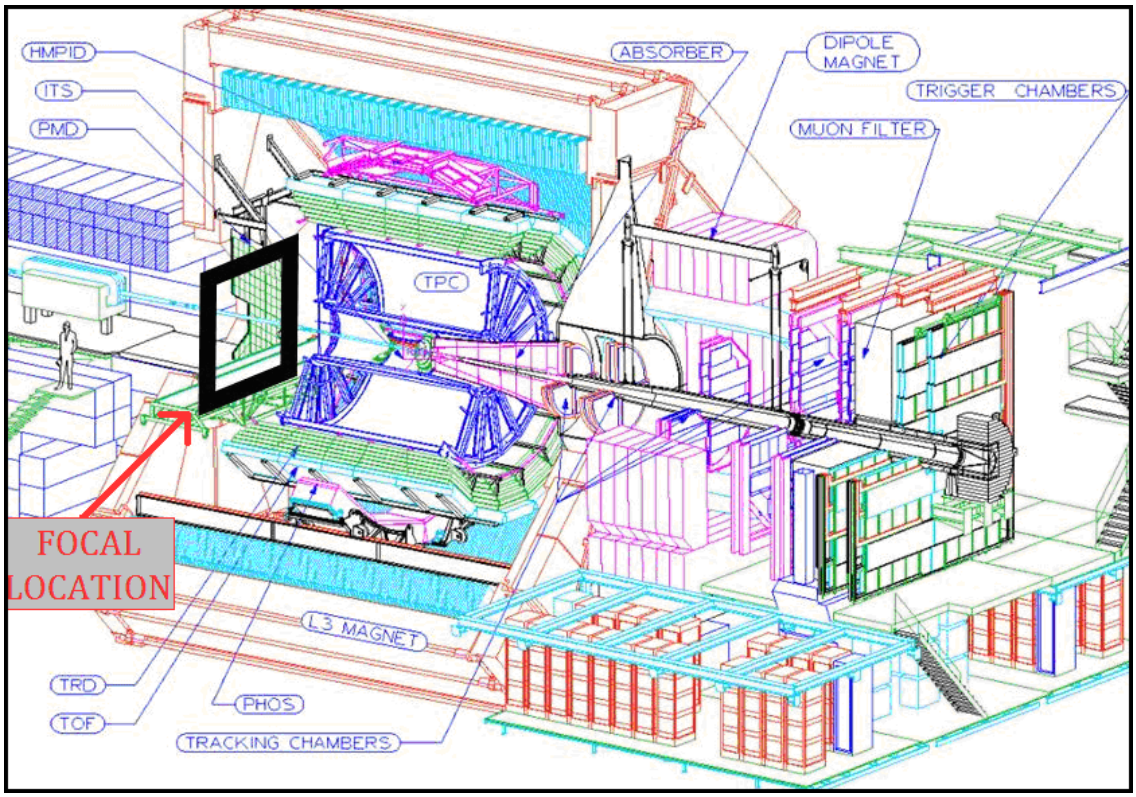

Figure 3: Location of FoCal in the ALICE setup

The condition of a high granularity can only be satisfied in a detector with a small Molière radius. The Molière radius is the distance from the shower axis in which on average 90% of the energy is deposited. If this radius is too large the showers will quickly broaden within the detector effectively rendering showers of tracks at small spatial separations indistinguishable. Tungsten provides an extremely small Molière radius of merely 9mm. In addition tungsten is a high-Z material which makes it suited as absorber material in a compact electromagnetic calorimeter. In order to keep the Molière radius this small the active layers between the tungsten should be as thin as possible. In these layers the application of silicon sensors is proposed for they can be made very thin and at the same time offer ultimate spatial resolution. A structure of alternating tungsten and silicon layers is thus ideally suited for the requirements of FoCal.

The studies and Monte Carlo simulations conducted so far on the silicon-tungsten geometry have suggested a pixel size on the order of $1mm^2$ should be sufficient to meet the requirements. In the silicon sensor layers this pixel size can be accomplished by using one of the following technologies:

- Conventional silicon sensors with pixel sizes of 1 mm^2 and analogue readout
- Monolithic active pixel sensors (MAPS)

The first solution is a proven concept however the precise implementation of this kind of sensors in FoCal still requires some research. The MAPS chips offer even higher granularities with pixel sizes in the order of a few tens of microns. However a drawback of these chips is the relatively slow readout and the huge amount of data they generate when

implemented at such a large scale. Current investigations concern the online aggregation of multiple adjacent pixels to form larger so called multipixels, which would greatly compress the data stream.

The primary purpose of any calorimeter is of course the measurement of particle energies. An essential aspect of these measurements is the energy resolution that can be obtained. Therefore a lot of the simulation efforts have focussed on this resolution for the proposed geometry. These Monte Carlo simulations have demonstrated that a high granularity detector like FoCal offers great additional potential to the ALICE experiment.

1.7.3 FoCal group of Utrecht University

The FoCal collaboration consists of several research and development groups world wide. These groups are investigating different sensor technologies, small scale prototypes or simulations of the FoCal concept as described above. The group that is supported by Utrecht University is working on a small scale prototype that should proof the applicability of the MAPS technology in FoCal. The first beam test of the prototype has recently taken place at DESY measuring electrons up to 5GeV and currently a beam test at SPS CERN is being conducted in order to gather more data. The analysis of the data is still in a very early stage, however individual events have already been successfully isolated from the data.

1.7.3.1 FoCal geometry

The geometry of the Utrecht FoCal concept consists of 24 layers. Each layer contains:

- 2 square tungsten slabs on which the printed circuit boards (pcb's) are mounted
- 4 L-shaped printed circuit boards on which the sensor chips are mounted
- 4 2x2cm MIMOSA chips
- 4 stainless steel spacers
- 2 tungsten filler slabs

In the assembly procedure the MIMOSA chips are glued to the pcb's after which the fine electrical connections between the read-out zone and pcb are established. The pcb's consist of alternating thin copper and FR4 layers. FR4 is a mixture of fibreglass and epoxy resin. Next two of these pcb assemblies are glued to a tungsten absorber plate. The pcb's are positioned tightly together minimizing the gap between the chips. However, due to a 320μm wide column of row drivers on the chip that are described in more detail in the next section a narrow dead strip in the detection area is inevitable. Subsequently two stainless steal spacers are positioned on the absorber plate alongside the pcb's.

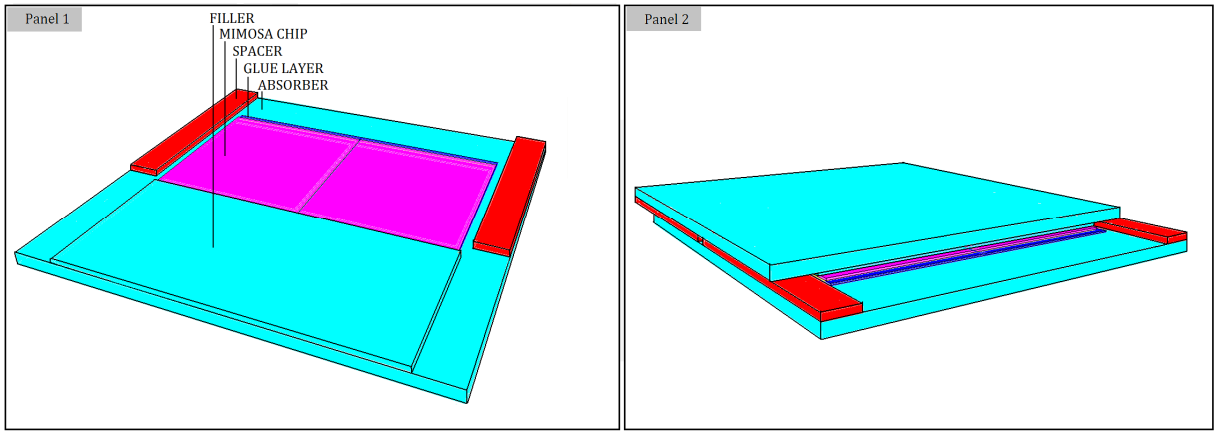

Figure 4: Panel 1, bottom half of single detector layer. Panel 2, single detector layer

The spacers maintain exactly enough space between the tungsten plates preventing the chips from touching the adjacent absorber. Finally the tungsten filler slab is glued on the tungsten base plate. This tungsten plate will prevent the presence of relatively large air gaps that would increase the Molière radius. The setup as described so far is the bottom half of a single layer and is depicted in Figure 4. To complete the layer the top half that is identical to the shown assembly is put up-side-down on top of the bottom half with the L-shaped pcb's sticking out of the tower opposite to the bottom assembly pcb's as is shown in Figure 4. Finally 24 of these layers are stacked and compressed to enhance heat conduction throughout the structure. In Figure 5 a schematic cross section of the centre of two adjacent layers is shown. In this picture is clearly visible how the active areas slightly overlap to prevent dead areas in the detection region. The absorber and filler plates respectively 1.5mm and 0.3mm thick effectively constitute a 3.3mm tungsten layer between the active layers, which is very close to the 3.5mm radiation length in tungsten.

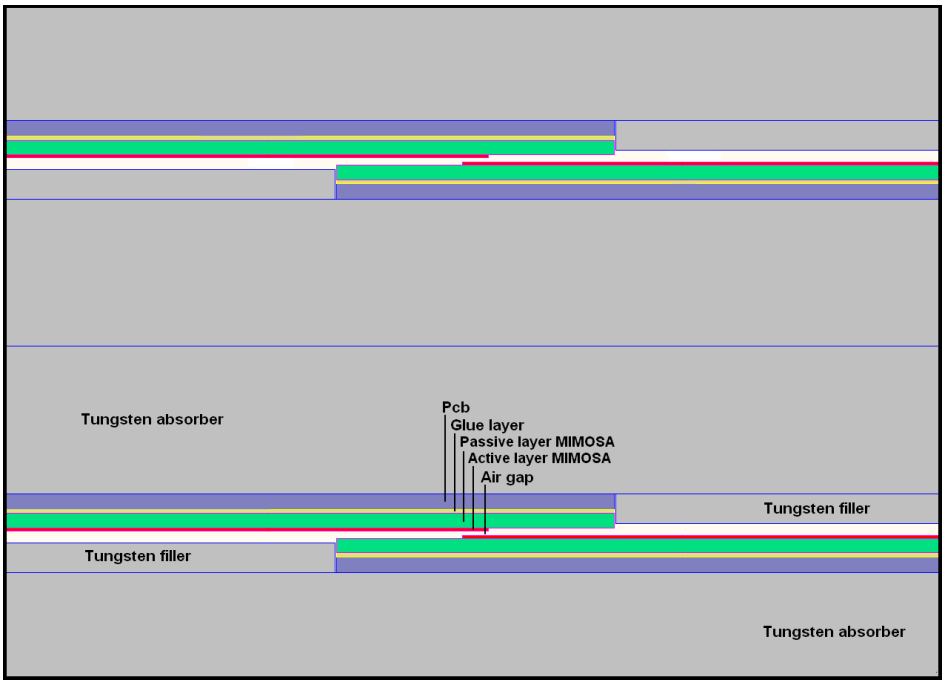

Figure 5: Schematic layout of the centre of two adjacent detector layers

1.7.3.2 MIMOSA chip

The MIMOSA chip is a so called Monolithic Active Pixel Sensor. It is a family of CMOS chips designed for the measurement of ionizing radiation. The MIMOSA chips used in the prototype have an epitaxial layer of approximately 30µm and a passive layer of 150µm. In Figure 6 the front view of the implemented MIMOSA type is shown. The active area contains 640x640 square 30µm pixels. On the left a 320µm wide strip contains the row drivers that manage the readout process and at the bottom a 2mm wide strip is dedicated to the readout logic. In this zone each column is connected to an adjustable discriminator that converts the collected charge of a pixel to a single bit. At the bottom edge of the readout zone one finds the electrical connections to the pcb of the readout channels, power supply etc. . These connections are the most delicate part of the setup.

As an ionizing particle traverses the epitaxial layer a charge is created. A minimal ionizing particle (MIP) liberates approximately 80e- per µm in silicon. This results in 2400e- for a 30micron layer, while the noise at room temperature is merely in the order of 10e-. After its creation the charge spreads through the epitaxial layer through thermal diffusion and is finally collected by the pixel diodes. Because of this charge spreading effect only about 25% on average of the liberated charge in a pixel is collected by the diode of that pixel. The rest of the charge is collected in adjacent pixels. This effect plays a crucial role in the comparison of the total response of the detector in simulations to the response in reality.

The readout mechanism of the pixel array is quite specific for the MIMOSA chip. This

mechanism is referred to as the rolling shutter mechanism. In this mechanism one row at a time is read out. So all the pixels on a row are read out simultaneously at the bottom generating 640 bits, after which the next row is read out. It is important to mention that the rolling shutter starts its cycle when the power supply of the chip is turned on. Given the current readout time of the used MIMOSA chip is still relatively long (~700µs) the following scenario can occur. Suppose the rolling shutter is halfway through its cycle when a shower occurs on the chip. All the hits on the chip of a single shower occur almost simultaneously compared to the readout time of a single row. This will cause the bottom half of the shower hits to be stored prior to the top half. This effect especially complicates the reconstruction of events from the prototype data when showers of separate events occur close together in time.

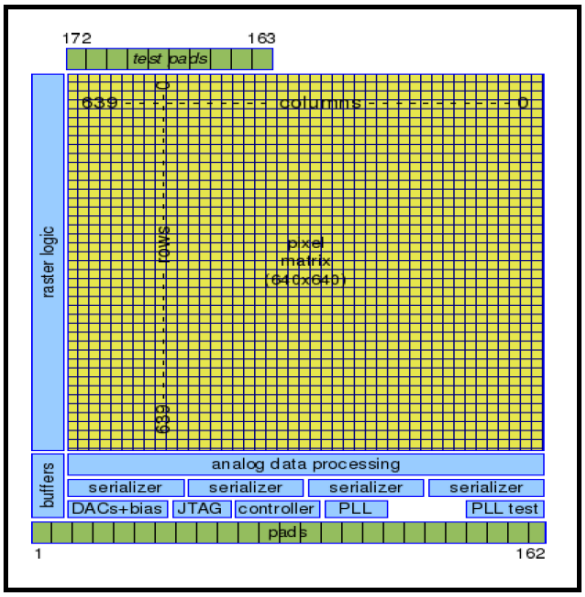

Figure 6: Schematic representation MIMOSA chip

1.7.3.3 Data acquisition

Every individual MIMOSA chip has 4 output channels. Every channel is connected to 4 subgroups of 40 columns of the pixel array. So every channel represents 160 columns. Now the first 4 bits on a channel are the bits in the first column of every group. The next 4 bits are the second column of each group etc. etc. . The 96 channels of every 24 chips are connected to a specific FPGA system called a Spartan. The Spartans synchronize the data streams of the different chips. Given the total of 96 chips of the FoCal prototype 4 Spartans are implemented in total. After processing by the Spartans the 96 channels continue to a Virtex board. Every set of 2 Spartans is connected to its own Virtex board. The Virtex board is another FPGA system that sequences the data streams from the Spartans and redirects it to memory. The Virtex board stores and sequences the simultaneously arriving 96 bits of both Spartans 4 times after which it combines 128 bits of both Spartans 3 times and sends this to final storage in the memory of the DAQ. The Virtex board also handles the trigger data. This elaborate readout mechanism is schematically shown in Figure 7. The readout

frequency of every channel is 160MHz, so the readout time of all the rows in the pixel array is 640µs. The frame readout frequency of the detector is therefore in the order of 1kHz, which is still too low for the eventual FoCal purposes. However promising research on the MIMOSA chips is currently carried out.

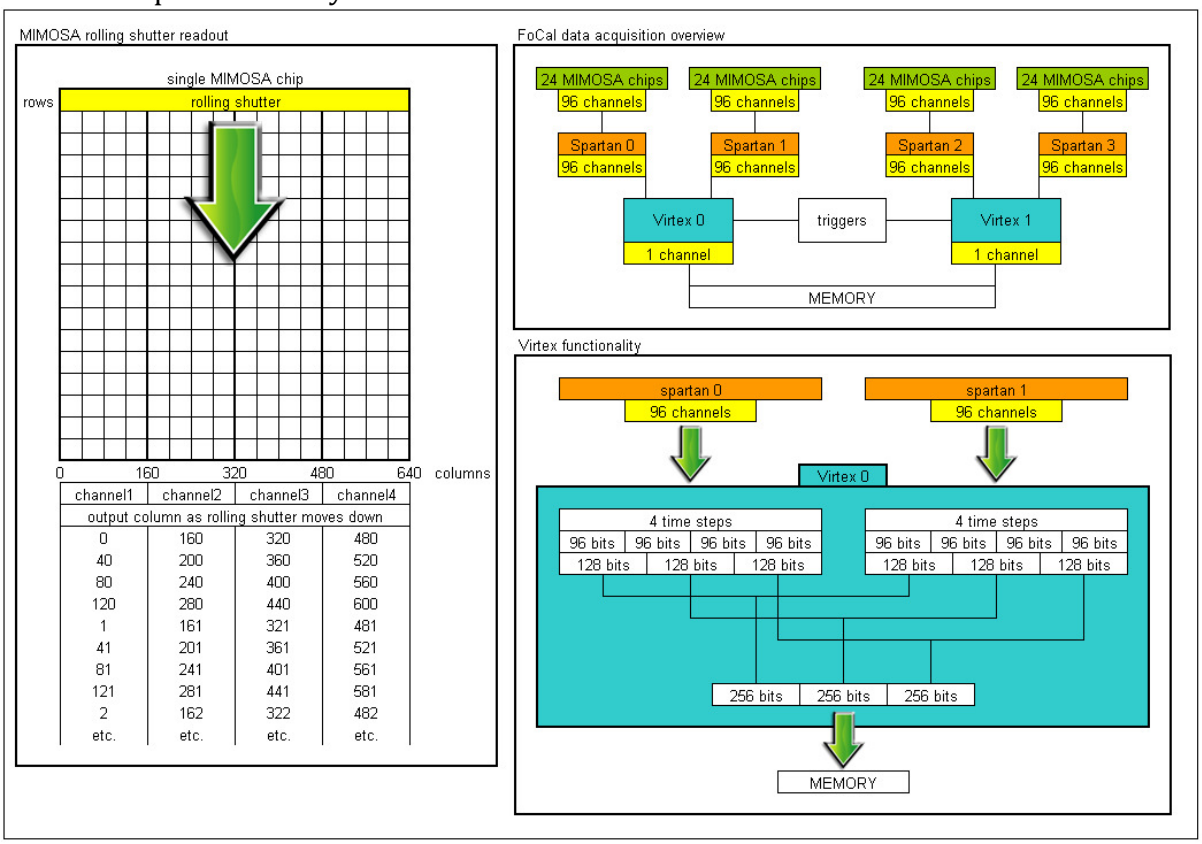

*Figure 7:*data acquisition scheme

1.7.3.4 FoCal simulations

The focus of this thesis is on the development of a simulation framework for the FoCal concept as envisioned by the University of Utrecht group. Flexibility of this framework was reached through the implementation of several interfaces allowing relatively new users to quickly conduct simulations to their liking, while still being able to control all the aspects of the simulation in great detail. The rest of this thesis includes the description of the simulation framework and some demonstrations of its major features followed by a verification of its proper functioning by comparison to other simulations and theoretical estimates. Finally some results on shower development and the expected total response of the prototype are included.

2. The FoCal simulation framework

The simulation framework was written for the ALIROOT environment. This environment is based on the C++ object oriented language and consists of a large collection of classes. The objects of these classes offer all kinds of functionalities varying from linear algebra calculations to data visualizations. Of specific importance to the simulation framework are the abstract classes that function as interface to GEANT3. These offer a direct control over the GEANT3 framework that is based on the FORTRAN language. In addition the GeoManager class of ALIROOT functions as a flexible interface to the more obscure GEANT3 geometry construction functions and has proven to be particularly useful.

The simulation framework can be split up in several versions that all have their own specific purpose. However each version runs through one or more of the following phases:

- GEANT3 simulation by the Monte Carlo application
- Frame reconstruction by the FocalPixelManager or the FocalPixelManagerPhysical
- Hit reconstruction by the FocalReconHitGenerator
- Data reconstruction by the FocalDataManager

These different phases will be treated in detail in the following sections. The phases use ROOT files as format for both their input and output. These ROOT files are either output from previously executed phases or generated from the user interfaces that use text files as format. These user interfaces greatly simplify matters for new users of the framework and allow them to focus on the analysis of the output of the simulation. The user interfaces are also treated in the following sections.

2.1 User interfaces

The Geometry interface sets the geometry to be used by GEANT3 in the simulation. The geometryfile.txt contains in a compact and accessible way the geometry description. In this file first the different media are defined. Next volumes can be created of all kinds of shapes consisting of one of the previously defined media. Then the volumes can be composed to form bigger structures. Finally individual volumes or compositions can be misaligned, set sensitive and given a unique name and layer number. In addition the energy cut off values of the different particles and the step size parameters of the GEANT simulation can be set in the geometry file. These parameters can not be set for each volume individually. The user manual of the geometry file can be found in APPENDIX 6.2.

The primaryfile.txt contains the definition of the primary particles that will be impinging on the geometry in the simulation. This is done by defining parameters like the particle type, origin, angular distribution, momentum and polarization. All parameters can be chosen exact or according to a certain distribution. In addition the PYTHIA and HIJING event generators can be switched on and configured in the primary file. The HIJING event

generator simulates heavy ion collisions and the PYTHIA generator simulates proton-proton collisions. The particles that are produced in these collisions can be used as background to the user defined particles. The manual of the primary interface can be found in APPENDIX 6.3.

The analysis file contains all of the information about the exact pixel structure of the chips in the detector. This information is used by the pixelmanager class in the frame reconstruction phase. During this phase the pattern of energy depositions in the detector is converted to an actual hit pattern on the different chips. This phase is described in more detail below. The manual of the analysisfile can be found in APPENDIX 6.4.

The drawfile.txt contains information about what data of the simulation should be depicted on screen. This can be useful to check whether a simulation functions properly and to check whether the geometry is correct. Data from all three major phases can be drawn. The energy depositions from the GEANT simulation, the frames from the frame reconstruction phase and the reconstructed hits from the hit reconstruction phase. The manual of the draw interface is located in APPENDIX 6.5.

2.2 Simulation phases

2.2.1 GEANT simulation

The GEANT3 simulation is always the first phase of any simulation. When the simulation is run first an instance of the class FocalMCapplication is created. This object functions as interface to the GEANT3 program. It contains functions that are called by GEANT3 in a specific order. These functions define the parameters of the simulation and allow the user to extract data from the simulation. Upon creation of the FocalMCapplication object the following objects are created:

- AliStack: This object manages the particles that are transported by GEANT3. At the start of each event the PrimaryGenerator (described below) pushes the primary particles on the stack after which GEANT will pop them from the stack and transport them through the predefined geometry. When secondary particles are created in for example a bremsstrahlung processes these are pushed on the stack as well.
- FocalHitGenerator: This object manages the FocalHitArray and the SensitiveVolumeArray. The SenstiveVolumeArray contains SensitiveVolume objects. These objects contain the information on the volumes of the geometry that are sensitive. The FocalHitArray contains FocalHit objects. These contain all information on a specific energy deposition. Now every Monte Carlo step the FocalHitGenerator checks if any energy was deposited and if so whether this occurred in a sensitive volume. If this is the case the energy deposition is saved in the FocalHitArray.
- DetectorConstruction: This object creates an instance of the ALIROOT GeoManager class in which the geometry is created and saved as defined in the geometryfile by the user. Upon initialization of the simulation the geometry is handed to GEANT by

the GeoManager object.

- PrimaryGenerator: This object generates a set of primary particles at the start of each event as defined by the user in the primaryfile and places them on the AliStack. The PrimaryGenerator contains an array of TParticle objects that is generated upon initialization of the simulation. The primaries are generated as defined in the primaryfile. This class also contains an HIJING and PYTHIA6 event generator. If these are switched on in the primaryfile at the start of every event all the particles from the HIJING or PYTHIA event will be pushed on the stack in addition to the user defined primaries from the array.
- TRandom3: This object generates random numbers and is handed to the GEANT3 program upon initialization of the simulation. Moreover a random seed is given to the random generator at this stage, which prevents all simulations from being identical.

Next the simulation is initialized by the following actions:

- The AliStack and random number generator are handed to GEANT3
- The DetectorConstruction object constructs the geometry in the geomanager and hands it to GEANT.
- The FocalHitGenerator object creates the array of sensitive volumes.
- The physics section of GEANT is initialized. This involves the calculation of cross section tables.

Subsequently the simulation is run, this involves the following actions:

- The primary generator generates the particle array
- The GEANT simulation is started. GEANT will now call the following functions of the FocalMCapplication instance. BeginEvent, GeneratePrimaries, BeginPrimary, PreTrack, , Stepping, PostTrack, FinishPrimary, FinishEvent. The only functions that are used in the current state of the simulation framework are the following:
- Generate primaries: When this function is called the PrimaryGenerator pushes the particles from the particle array onto the AliStack in addition to any optional particles generated by the HIJING or PYTHIA event generator.
- Pre track: This function creates a TTrack object that is stored in the TrackArray of the FocalMCapplication instance. The tracks are only stored of those events that will be drawn later as requested in the drawfile.
- Stepping: This function is important since it is called at every Monte Carlo step of the simulation. First it makes the HitGenerator check whether an energy deposition occurred in this step. If this is the case and the current track position is inside a sensitive volume the hit will be saved. Optionally also the track position is stored in the track object if these tracks need to be drawn later.

Finally the simulation is terminated with the following actions:

- The array containing the FocalHit objects are saved in a ROOT file.
- The HitGenerator saves the sensitive volume objects for they will be needed later on when reconstructing the hit pixels.
- The primary particles that were defined by the user (this does not include the particles generated by HIJING or PYTHIA) are saved to a ROOT file. This data is

possibly needed in the analysis process of the simulation.

- The drawfile is checked for any requested data visualization in this phase of the simulation. Options would be drawing the saved energy depositions in the sensitive volumes of the detector geometry or the particle tracks of certain events.

2.2.2 Frame reconstruction

After the GEANT simulation phase the frame reconstruction commences. In this phase the energy depositions saved as FocalHit objects are converted to objects that contain all the information on a certain chip including all the hit pixels for a certain event. The frame reconstruction is performed by an instance of the PixelManager class. This object first loads the ROOT file with the FocalHit objects and determines for all of the hit objects in the hitarray the exact pixel that they occurred in. This is done on the basis of the chip parameters as described in the analysisfile. Next it constructs the so called frames. A frame is an object that contains a layer number, chip name, start time, end time, event number and a framepixelarray that in turn contains framepixel objects. The framepixel objects consist of a x, y and z coordinate. These frames can be considered pictures of the hit pattern at a given time taken by a certain chip. Subsequently a number of noise energy depositions is added to the framepixelarray of each frame. The way in which this is done is described in detail in the analysis file manual in APPENDIX 6.4. And finally the discriminator function of the focalframe class is applied. If multiple hits occurred on a single pixel this function will add their energy depositions. In addition it checks for all the framepixel objects whether their energy deposition exceeds the discriminator setting of the relevant column. If this condition isn't met by a framepixel object it will be removed from the framepixel array. Finally the array containing the frame objects is saved and if requested by the draw interface some frames or compositions of frames will be shown.

Most versions of the program do not use the frames as constructed above. They use the so called FocalPhysicalFrame objects. These objects are basically the same as regular frames with the minor difference that they contain all hits of a given event on the chip under consideration. So the rolling shutter mechanism is ignored and only one frame is constructed per chip per event. Subsequently noise is added as for a regular frame. The physical frames are used for the following reason. The frames as described above allow the program to mimic the exact output of a detector in the data reconstruction phase. However for the actual analysis of the detector behavior the precise output format is not very relevant. For these purposes only the locations of the hits as reconstructed from the data are relevant, which can be done using the physical frames. This method prevents unnecessary bookkeeping involved with analyzing multiple frames per chip per event. In addition in reality the parts of frames that just contain noise can be excluded by using the trigger data. In the simulation framework this would just introduce unnecessary bookkeeping when using the regular frames.

2.2.3 Hit reconstruction

After the frame reconstruction phase the hit reconstruction phase commences. During this phase the frames as constructed in the frame reconstruction phase are used to construct so called ReconEvent objects. These ReconEvent objects contain the user defined primary particles. This does not include the particles generated by HIJING or PYTHIA generators. Furthermore they contain the event number and an array of ReconHit objects. These ReconHit objects contain the coordinates, the volume name and the layer number of the hit. At the end of the hit reconstruction phase the ReconEvents are written to a ROOT file. This ROOT file can subsequently be used for the analysis of the detector performance.

2.2.4 Data reconstruction

During the data reconstruction phase the FocalFrame objects are converted to a bin-file that has the exact same format as the real FoCal data. Using these bin-files the scripts designed to reconstruct the actual data can be tested. The data is constructed from the frames by several multiplexing procedures as described in the data acquisition section above and depicted in Figure 7. The frames are separated in the bin-file by a checkerboard pattern and a user defined test pattern of both 768 bits corresponding to 4 readout cycles of all chip channels by the Spartans and 3 readout cycles of each Spartan by the Virtex boards. Finally two bin-files are generated one for each Virtex board that transfers data to memory.

2.3 Versions and their output

2.3.1 Focal Physical

The purpose of the Focal Physical version is the generation of a ROOT file that contains all the ReconEvent objects of a simulation of a large number of events. These ReconEvents can then be used for further analysis by scripts of the user. When this version is run the first phase executed is the GEANT simulation phase. This phase is followed by the reconstruction of the physical frames as described in the frame reconstruction section above. Finally in the hit reconstruction phase the ReconEvent objects are created and saved.

2.3.2 Focal Data

The purpose of the Focal Data version is the exact replication of the data generated by the detector. This includes the multiplexing procedures that are performed during the data acquisition process. When this version is run the first phase executed is the GEANT

simulation phase. This phase is followed by the frame reconstruction phase in which the regular frames are constructed. The final phase executed is the data reconstruction phase in which the bin-files are produced that have the exact same format as the output of the Virtex boards. These output files become very large already for a relatively small number of events, since a single readout of all chips generates 96 frames which result in 5MB of data.

2.3.3 Focal Pedestal

The purpose of the Focal Pedestal version is merely the generation of the FocalHit file, so only the GEANT simulation phase is carried out. This is useful for investigations into the distribution of energy depositions throughout all the detector volumes for example. This version also has features that allow the determination of the flux of specific types of particles at predefined depths in the detector. These features do not have their own interface yet. This version was specifically designed to check the reliability of the GEANT simulation phase.

2.4 Demonstration

In this section several features of the various simulation phases are presented. These are all results that can be requested through the draw file of the visualization interface.

2.4.1 Detector geometry

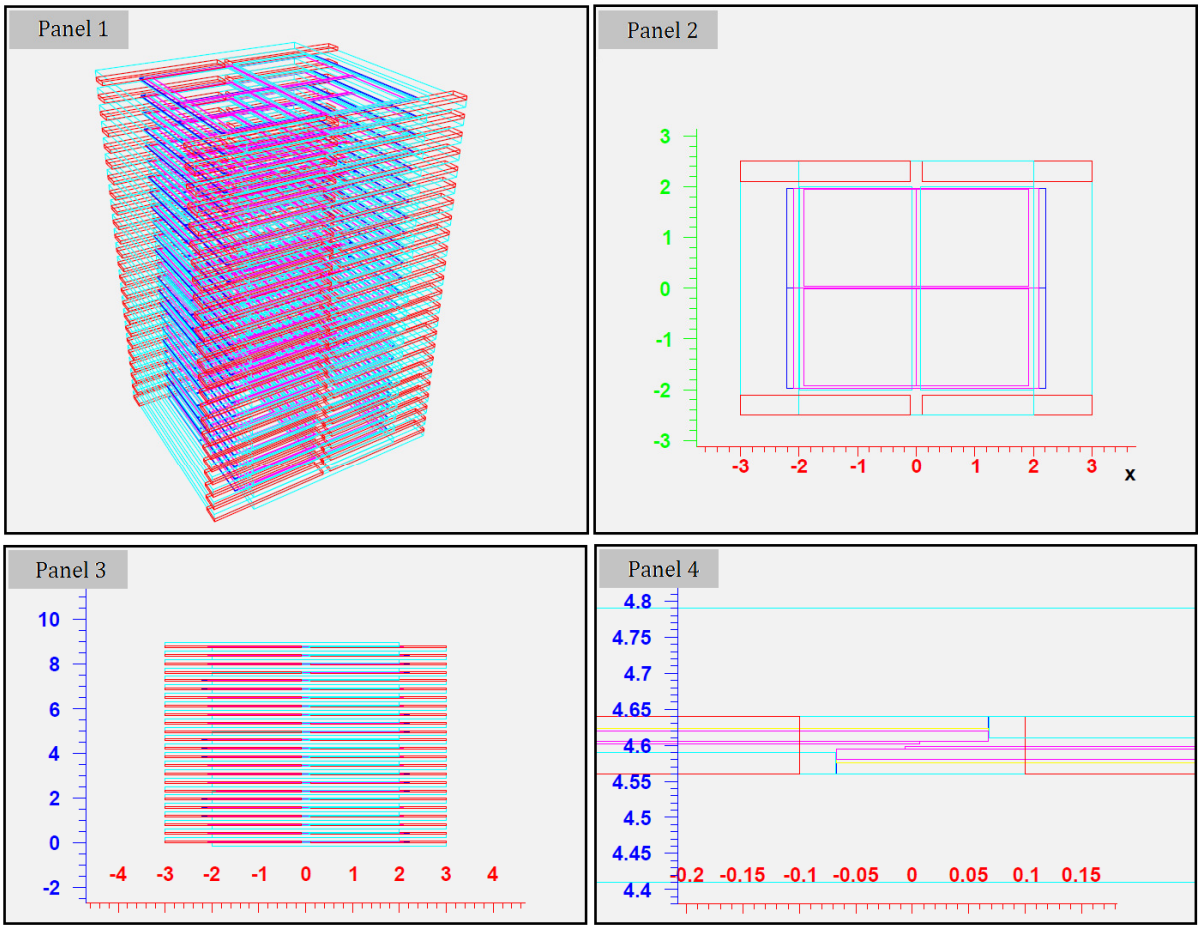

Figure 8: Panel 1, perspective of detector geometry. Panel 2, topview of geometry. Panel 3, front view of detector tower. Panel 4, zoom-in side view

Figure 8 shows the detector geometry that is defined in the geometry file. In panel 2 the four MIMOSA chips that make up each detection layer are clearly visible. In the side view of panel 3 the 24 detection layers can be clearly distinguished. Finally panel 4 shows a zoomed-in view of the side view of panel 3. This view closely resembles the schematic view of Figure 5.

2.4.2 Particle tracks

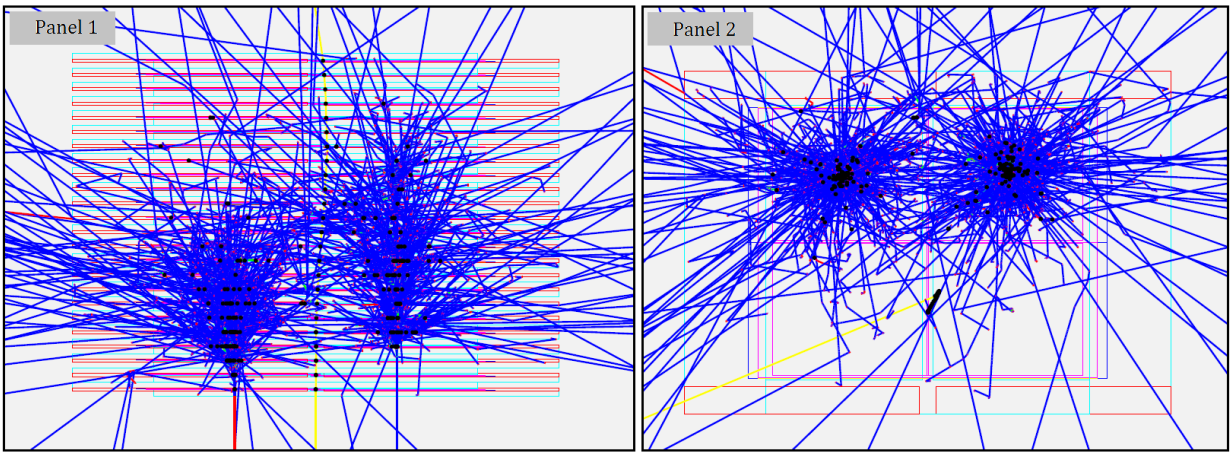

Figure 9: Panel 1, side view of particle tracks in detector geometry. Panel 2, top view of particle tracks in same event

Figure 9 shows the top and side view of a single event with three primary particles. An electron, a photon and a muon each with an energy of 2GeV. The primary particles enter the detector geometry at the bottom. The yellow, blue, green and red tracks represent respectively the muons, photons, positrons and electrons. The electromagnetic showers caused by the incident electron and photon are clearly visible. The muon does not cause a shower as expected since it characteristics approach those of a minimum ionizing particle. The black dots are the locations of energy depositions in the epitaxial layer of the MIMOSA chips. The showers of the photon and the electron are qualitatively similar as expected with the anticipated difference that the photon shower is shifted deeper into the detector. This is the result of the mean free path length of the photon while the electron will start losing energy immediately upon entering the tungsten.

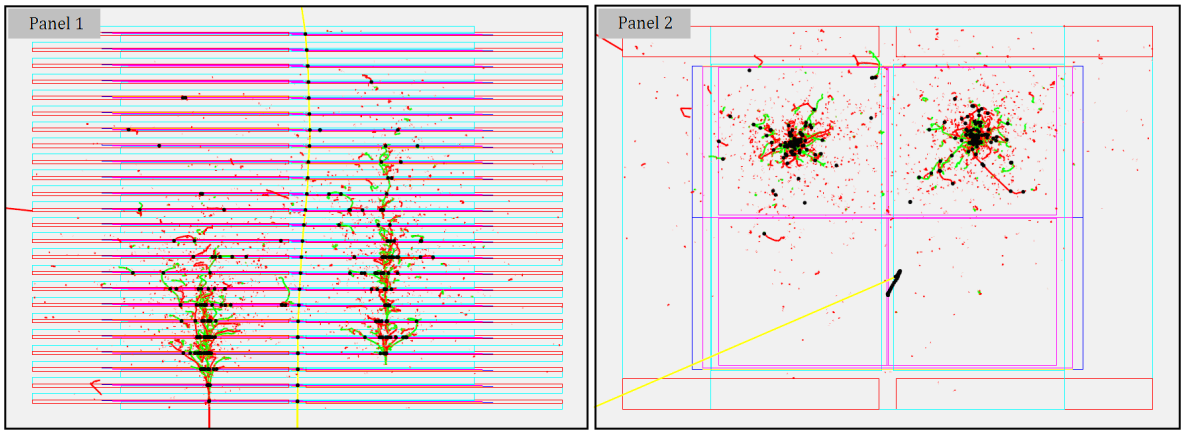

Figure 10: Panel 1, side view of the particle tracks excluding the photon tracks. Panel 2, top view of the same event.

Figure 10 shows the top and side view of the same event as depicted in Figure 9, however in these picture the photon tracks are not shown. Comparing Figure 9 to Figure 10

the large discrepancy between the photon and charged particle flux in the detector becomes evident. In this comparison it also becomes instantly clear that the overwhelming majority of the pixel hits are caused by traversing electrons and positrons rather then photons.

2.4.3 GEANT simulation phase results

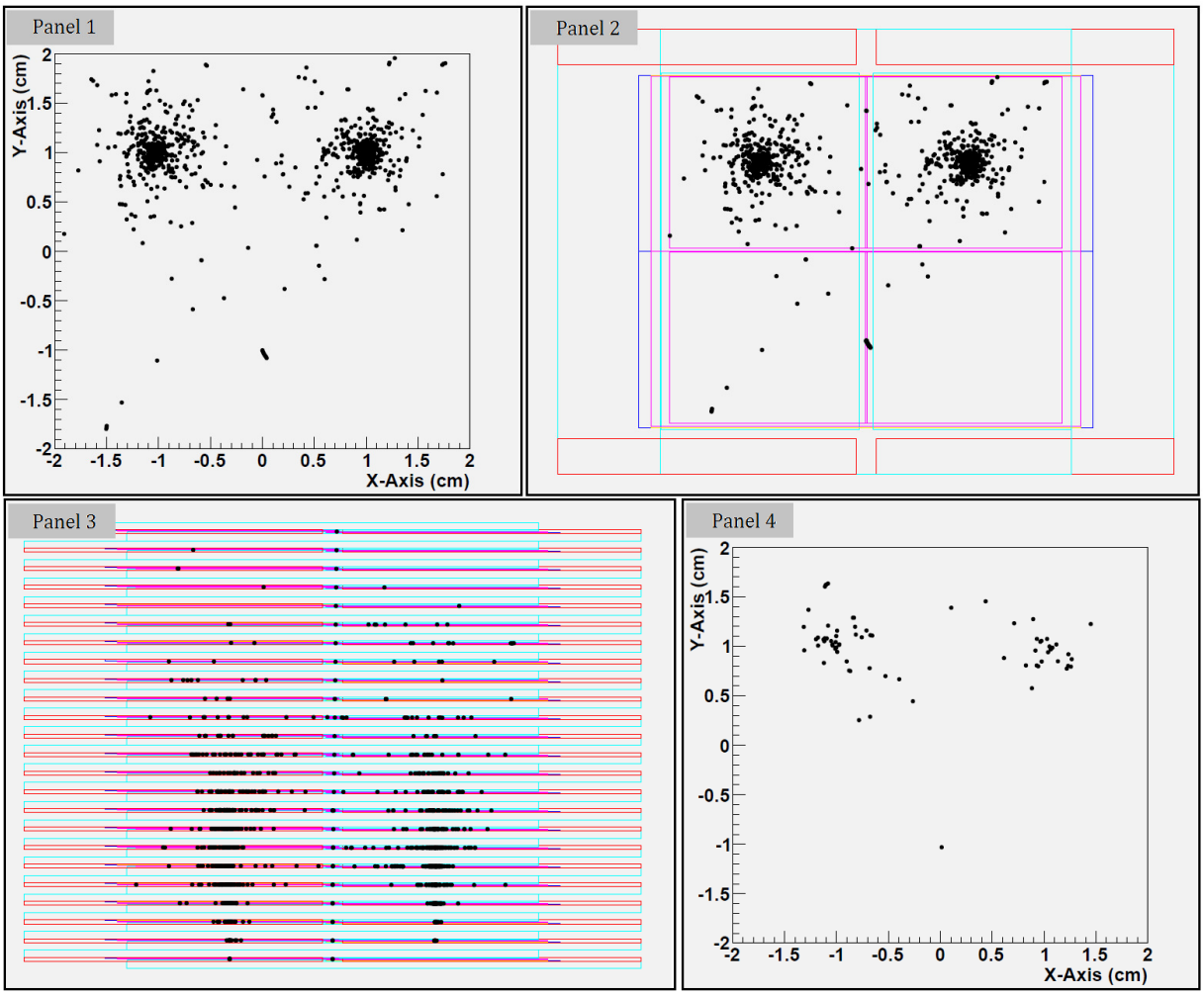

Figure 11: Panel 1, energy depositions in all layers. Panel 2, top view of energy depositions in the geometry. Panel 3, side view of energy depositions in geometry. Panel 4, energy depositions in the 9th layer

Figure 11 shows the data of a single event gathered in the GEANT simulation phase. The event simulated is similar to the one in Figure 9 with the only difference that all primary particles have 10GeV energy. During the GEANT simulation an array of FocalHit objects is created. A FocalHit object corresponds to an energy deposition in an active detector volume and it contains information like the layer number, volume name and position of said energy deposition. In panel 1 the energy depositions in all layers are shown in the mother reference frame. Panel 2 and 3 show the energy depositions in the active layers of the detector geometry. Finally panel 4 depicts the energy depositions of a single layer.

2.4.4 Frame reconstruction results

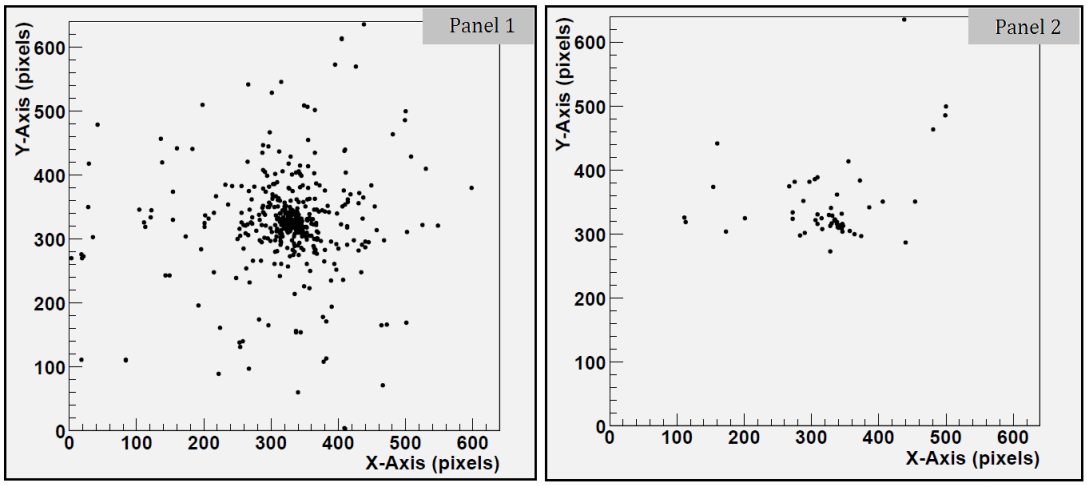

Figure 12: Panel 1, sum of frames of chip 0 in all layers for event of Figure 11. Panel 2, frame of chip 0 in layer 9 for same event.

In Figure 12 a selection of the frame reconstruction data of the event depicted in Figure 11 is represented. A normal frame contains the hit pixels of a single readout cycle of a single MIMOSA chip. Here however physical frames are considered that contain all the hit pixels of an entire event. Panel 1 shows all the hits on chip 0 in all layers, as can be checked this picture does resemble the photon shower in the top right corner of Figure 11 panel 2. Note here that Figure 12 is the top view of the MIMOSA chip while Figure 11 panel 2 shows the bottom side of the chips that contain the photon shower. In panel 2 a single frame is depicted. This frame corresponds to the MIMOSA chip 0 in layer 9 for this event.

2.4.5 Hit reconstruction results

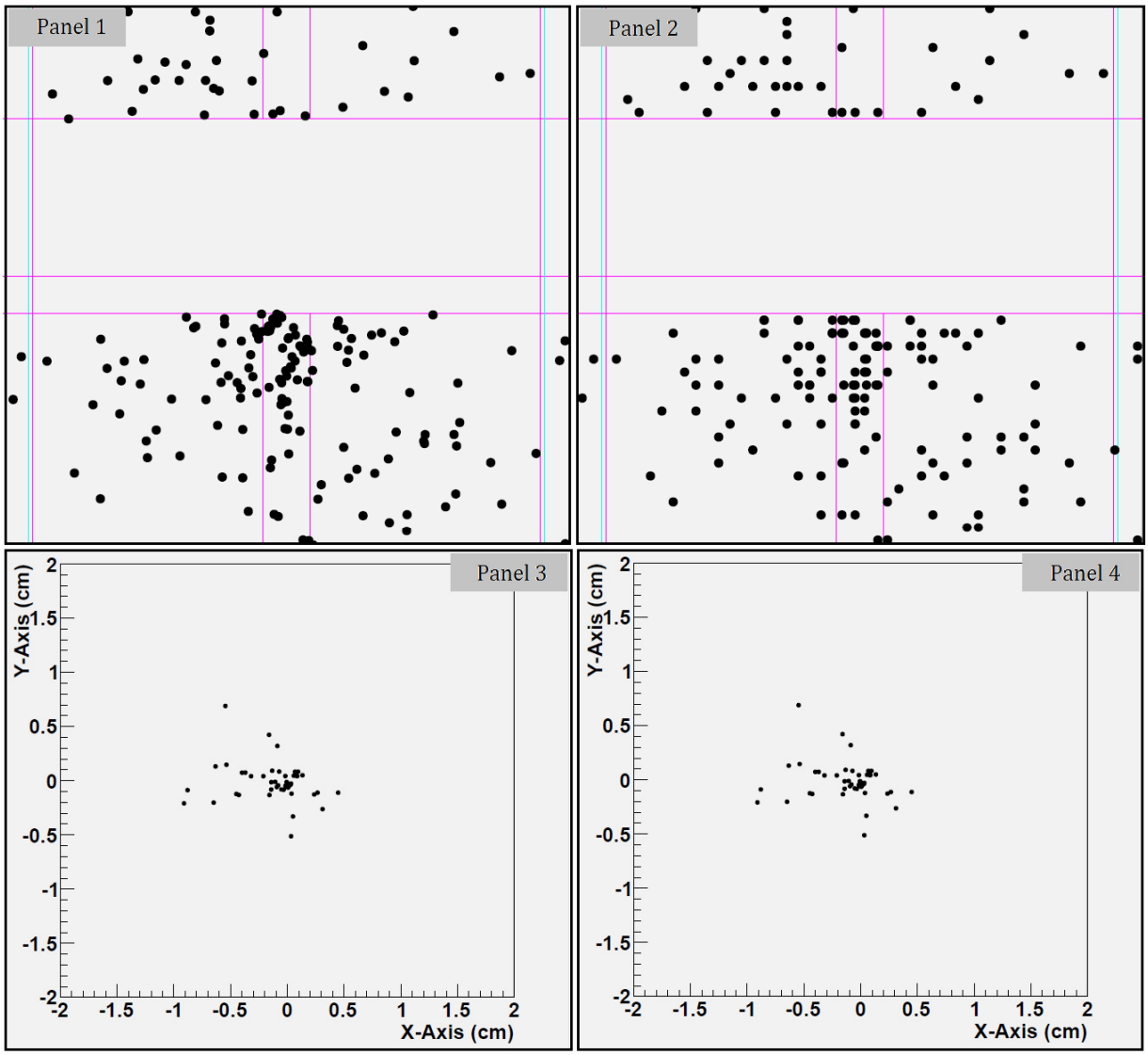

Figure 13: Panel 1, energy depositions in zoomed-in top view of centre of detector for a 20GeV electron incident on centre of detector. Panel 2, reconstructed hits of same event in same view. Panel 3, energy depositions in layer 9. Panel 4, reconstructed hits in layer 9.

Panel 1 and 3 of Figure 13 show the raw energy deposition data from the GEANT simulation. Panel 2 and 4 show the locations of the energy depositions that were reconstructed from the physical frames. The effect of the pixel structure of the MIMOSA chip on the reconstruction of the hits becomes evident in panel 2 where the hits appear orderly on a grid. However on a larger scale the ordering of the hits on the grid is not visible due to the small pixel size. This becomes clear upon comparison of panel 3 and 4. In the results presented in this section the noise and discriminator features of the program were ignored.

3. Focal simulations

The main purpose of the simulation results presented here is determining whether the simulation framework offers realistic insight into the response and general functioning of the FoCal detector and consolidating its position as a reliable tool in the R&D process of FoCal. Note that these results only apply to electromagnetic showers and do not allow for any conclusions on hadronic showers. The following aspects of the simulation of electromagnetic showers in FoCal are treated.

First of all a check of general energy conservation is performed. This involves the total energy deposition in all detector volumes combined with all energy leaking out of the detector. The sum of these two contributions should equal the energy of the primary particle. Secondly the exact distribution of energy over the different detector volumes is considered in order to make sure the amount of energy deposited in the sensitive detection volumes is correct. Next the precise characteristics of the energy deposition processes are investigated. This is done by determining the dE/dx curve for the electrons traversing the active volumes.

Finally the precise spatial distribution of the showers is investigated. If the total energy is accounted for and the energy is distributed correctly over the different volumes the conclusion can be drawn that the correct amount of energy ends up in the active volumes. If in addition the energy deposition process of particles is realistically reproduced then the total number of hits should be reasonable as well. And if finally the shower shape is also similar to known shower profiles the final conclusion can be drawn that the simulation frame work should realistically reproduce the response of the FoCal to electrons, positrons and photons.

3.1 Total energy deposition and distribution analysis

3.1.1 Theoretical background

The purpose of the section is the execution of the consistency check on the amount of energy that is absorbed by the active volumes in the FoCal detector. These are the $30\mu m$ thick epitaxial layers of the MIMOSA chips. This is important since it is not a priori clear that GEANT correctly treats such thin layers correctly for this is a quite unusual running scenario for GEANT. First some concepts will be introduced that play a key role in the discussion on the energy distribution of a sampling calorimeter like FoCal.

The calorimetric response is defined as the average calorimeter signal divided by the energy of the particle that caused it. This quantity is a constant in a large range of primary energies. However as shall be considered in the final results section on the total detector response there are effects at high energy that render this quantity non-linear. The detector

response does not merely depend on the energy of the primary particle. It also depends on the type of particle. In order to compare the response of different particles the so called X/mip ratio was introduced, where X is the detector response to a certain particle X and mip the detector response to a minimum ionizing particle. Note here that a mip is a hypothetical particle since any mip that traverses a medium immediately loses energy and therefore seizes to be a mip. The mip signal is used as a reference frame for other particle signals since the way in which it loses its energy in a medium and thus generates a signal is identical to that of an electromagnetic shower though much less complicated to describe. Therefore in a homogenous detector were all deposited energy contributes to the signal e/mip = 1, given that the energy deposited by the mip's is equal to the energy deposited by the shower. As it will turn out this is not the case for sampling calorimeters in general as will be discussed later on.

Another important concept needed in the consideration of the energy distribution is the sampling fraction. The sampling fraction is defined according to [1] as the ratio of the energy a mip deposits in the active layers and the total energy it deposits during its traversal.

$$f_{sam} = \frac{d_{act} \cdot \left.\frac{dE}{dx}\right|_{act}^{mip}}{d_{act} \cdot \left.\frac{dE}{dx}\right|_{act}^{mip} + d_{pas} \cdot \left.\frac{dE}{dx}\right|_{pas}^{mip}} \tag{3.1}$$

with d_{act} and d_{pas} the total thickness of the active and passive layers respectively. And dE^{mip}/dx_{act} and dE^{mip}/dx_{pas} the energy loss per unit distance of a *mip* in the active or passive material respectively. It turns out that for sampling calorimeters of which the Z-value of the active material is smaller then the Z-value of the absorber material the *e/mip* < 1. A reasonable approximation according to [2] is

$$\frac{e}{mip} = \frac{1}{1 + 0.007(Z_{pas} - Z_{act})} \tag{3.2}$$

with Z_{pas} and Z_{act} the effective Z-value of the passive and active material respectively. This peculiar behaviour of the *e/mip* ratio for sampling calorimeters is known as the transition effect and it renders the description of a shower by a mere set of *mip*'s inadequate. First of all this effect is not caused by a discrepancy between the shower development in the absorber versus the development in the active layers, because the active layers are much thinner then a single radiation length (especially in FoCal) and the shower requires a good fraction of a radiation length to significantly alter its behaviour.

Rather the effect is explained by the behaviour of low energy photons. A large fraction of the energy in the shower is carried by low energy (<1MeV) photons that originate from the bremsstrahlung process. These low energy photons create low energy electrons in turn through the photo-electric effect and Compton scattering. Now the cross section of the photo-electric effect is proportional to Z^5 of the considered material. This causes the overwhelming majority of the low energy photons to interact in the absorber in stead of the active layer. In addition the soft electrons from the photo-electric effect have a very limited range in the absorber material. Moreover only the soft electrons created directly at the edge

of the absorber will be detected. These two effects cause the sampling of the low energy electrons to be incomplete and it effectively lowers the response of the sampling calorimeter to showers. It is in this argument that also the importance of setting the energy cut off values low enough in the simulation becomes apparent.

Concluding the *e/mip* ratio and the sampling fraction are important parameters that characterize the energy distribution in a sampling calorimeter. Furthermore they are ideally suited for the consistency check pursued here. Therefore the next step will be the determination of the *e/mip* ratio and sampling fraction for FoCal and their comparison with theoretical estimates.

First of all the determination of the sampling fraction for FoCal is conducted in the following manner. Equation (3.1) is applied with

$$d_{pas}\cdot\left.\frac{dE}{dx}\right|_{pas}^{mip} = d_W\cdot\left.\frac{dE}{dx}\right|_W^{mip} + d_{cu}\cdot\left.\frac{dE}{dx}\right|_{cu}^{mip} + d_{FR4}\cdot\left.\frac{dE}{dx}\right|_{FR4}^{mip} + d_{si,pas}\cdot\left.\frac{dE}{dx}\right|_{si}^{mip}$$

$$d_W\cdot\left.\frac{dE}{dx}\right|_W^{mip} = 77.7\text{mm}\cdot 2.21\text{MeV mm}^{-1}$$

$$d_{cu}\cdot\left.\frac{dE}{dx}\right|_{cu}^{mip} = 1.2\text{mm}\cdot 1.26\text{MeV mm}^{-1}$$

$$d_{FR4}\cdot\left.\frac{dE}{dx}\right|_{FR4}^{mip} = 7.2\text{mm}\cdot 0.40\text{MeV mm}^{-1}$$

$$d_{si,pas}\cdot\left.\frac{dE}{dx}\right|_{si}^{mip} = 3.6\text{mm}\cdot 0.39\text{MeV mm}^{-1}$$

$$d_{pas}\cdot\left.\frac{dE}{dx}\right|_{pas}^{mip} = 177.7\text{MeV}$$

$$d_{act}\cdot\left.\frac{dE}{dx}\right|_{act}^{mip} = d_{si,act}\cdot\left.\frac{dE}{dx}\right|_{si}^{mip} = 0.72\text{mm}\cdot 0.39\text{MeV mm}^{-1} = 0.28\text{MeV}$$

With d_w, d_{cu} and $d_{si,pas}$ the total thickness of respectively the tungsten, copper and passive silicon layers in FoCal. The passive silicon layers represent the substrate layers of the MIMOSA chips. The copper layers are found in the printed circuit board on which the chips are mounted. The d_{FR4} is the total thickness of the fibreglass material that together with the copper constitutes the pcb's. Thus for the sampling fraction f_{sam} the following value is found

$$f_{sam} = \frac{0.28}{177.7} = 0.0016 \qquad (3.3)$$

3.1.2 Simulation results

Next the sampling fraction for Focal was determined in a simulation applying the FoCal pedestal version of the program as described in chapter 2 above. The results of the FoCal pedestal runs are shown in Figure 14. In these simulations the energy depositions in all of the individual volumes were saved. Subsequently for every event the total energy

deposition in the active layer of the chips, the absorbers and the remainder of the volumes was determined. Also the total energy of particles exiting the detector geometry was determined for each event. The simulation consisted of only 600 events because of the large amount of data produced due to saving all energy depositions. All particles were tracked down to the 10keV level, which is important keeping in mind the transition effect. The primary particles were 5GeV electrons impinging uniformly distributed on a 1x1cm square centred on the first absorber layer and perpendicular to said layer.

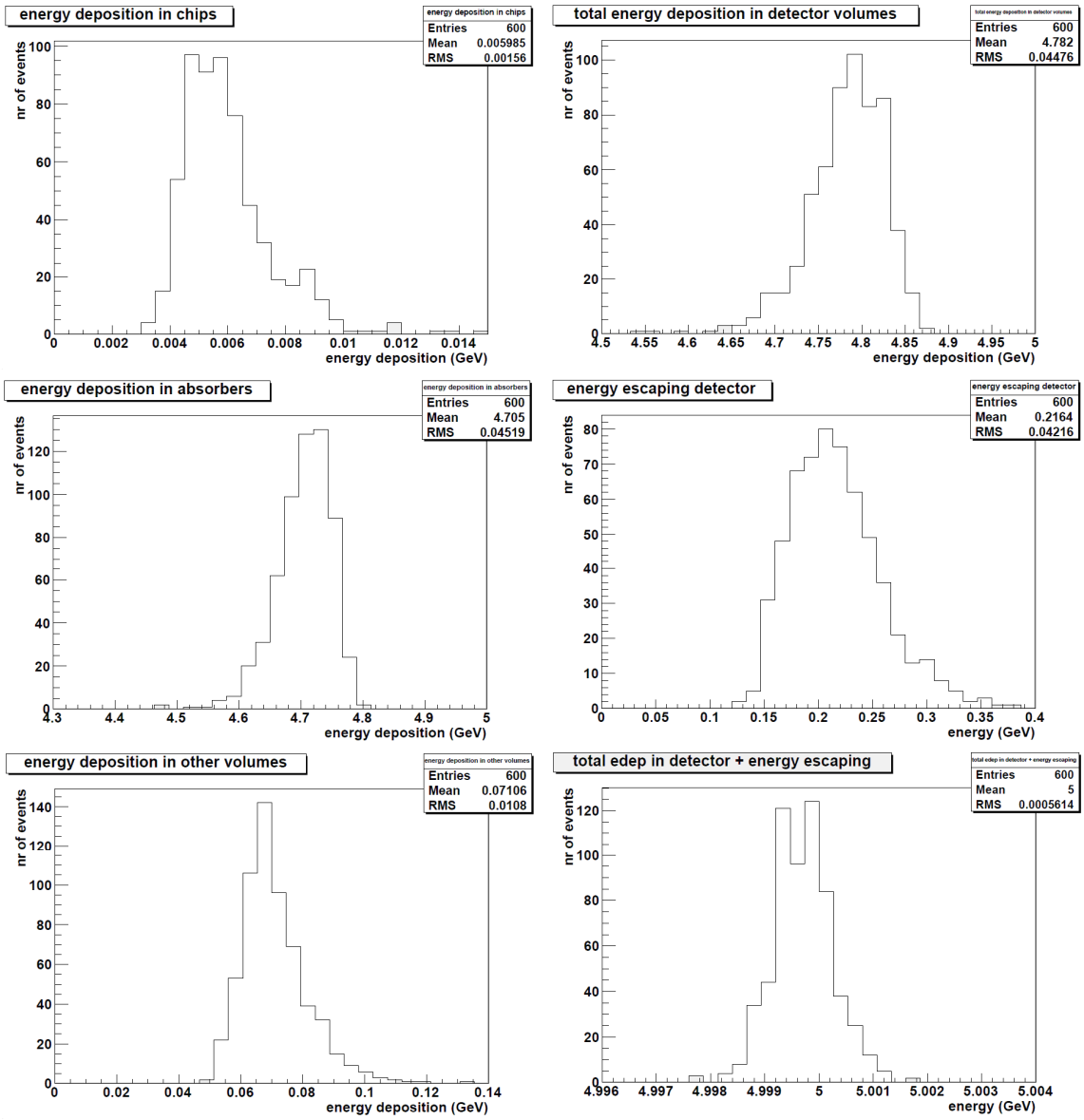

Figure 14: Panel 1, total energy deposition in active layer of MIMOSA chips. Panel 2, energy deposition in detector volumes. Panel 3, energy deposition in absorbers. Panel 4, energy that is not deposited in detector. Panel 5, energy deposition in volumes other then chips or absorbers. Panel 6, sum of energy deposition in all volumes and leakage energy.

These primary conditions were chosen to minimize lateral shower leakage while preventing systematical errors due to dead areas on the MIMOSA chips. Moreover the 5GeV was chosen for it roughly matches the energy at which recently the data at DESY was gathered with the actual FoCal prototype. Also for any higher primary energy the amount of data produced per event becomes too large to obtain adequate statistical precision.

First of all panel 4 shows that approximately 4% of the total energy escapes the detector geometry. Since this also involves a lateral shower leakage component this number is not relevant to the eventual FoCal setup that is much wider, however it evidently is for the functioning of the FoCal prototype. Secondly panel 6 of *Figure 14* shows the sum of the energy deposited in all detector volumes and the energy that escapes from the detector. It clearly shows that all of the primary electron energy (5GeV) is indeed accounted for in the simulation down to the 0.25‰ level.

Next using the total average energy deposition in the chips epitaxial layer and the total average deposition in the entire detector the sampling fraction can be determined.

$$f_{sam} = \frac{0.00598\text{GeV}}{4.78\text{GeV}} = 0.00125 \tag{3.4}$$

Comparing this value with the prediction of equation (3.3) the sampling fraction seems to be of by roughly 20% at first sight, however as established earlier the sampling of an electromagnetic shower shows quite substantial differences with the sampling of *mip*'s, especially in case of a large discrepancy in the Z-value of the passive and active medium. Using the *e/mip* ratio a more accurate estimate of f_{sam} can be made.

$$\frac{e}{mip} = \frac{\text{signal e}}{\text{signal mip}} = \frac{\text{electron edep in active layer}}{\text{mip edep in active layer}} = \frac{f_{sam}^{e} \cdot \text{total edep}}{f_{sam}^{mip} \cdot \text{total edep}} = \frac{f_{sam}^{e}}{f_{sam}^{mip}} = \frac{0.00125}{0.0016} = 0.78 \tag{3.5}$$

in which e stands for electron signal and edep for energy deposition. Finally according to expression (3.2) *e/mip=0.7* for FoCal using Z_{pas} = 74 and Z_{act} = 14. This value is remarkably close to the *e/mip* value calculated in (3.5). Concluding the sampling fraction is approximately 10% too high. This can be caused by an unrealistically high particle flux on the chips, an unrealistically high energy loss of the particles traversing the active layers or a combination of these two effects.

3.2 Thin layer energy deposition

The accurate modelling of energy deposition processes in extremely thin silicon layers like the MIMOSA epitaxial layer (30μm) is far from a trivial matter. This is the main motivation for the next consistency check of the simulation that consists of a thorough examination of these energy depositions. As will become clear the GEANT package contains quite sophisticated and accurate models for the simulation of these processes. In this section first the general theory on energy loss of electrons and positrons traversing a thin layer will be discussed followed by a brief description of the different models implemented

by GEANT to simulate these processes. Finally these theoretical results will be compared with the results from simulations. Since the gathered data from shower simulations are inherently not ideal for the investigation of aforementioned energy deposition processes, an extra simulation on thin silicon layers was set up in order to be able to draw any quantitative conclusions.

3.2.1 Theoretical background

As described in the introduction the electromagnetic shower consists of photons, electrons and positrons. The photons lose their energy through Compton scattering, the photo-electric effect and pair production. Photons will only deposit energy in the chips if one of these processes occurs in the chip volume in which case the recoiling nucleus absorbs a small fraction of the energy. It is possible that subsequently the created electron or positron deposits energy, however such an energy deposit is not counted as a photon energy deposition. In addition if the photon energy in the simulation decreases beneath the cut off value through one of the aforementioned processes the photon will seize to exist in the simulation and deposit all of its energy on the spot. Given the thickness of the active chip volume is only 30μm the probability for the occurrence of these scenarios is very small. Therefore the contribution of photons to the detector signal is negligible, which is also mentioned in the results presented below. Consequently the photon energy depositions will not be considered in much detail.

The electrons and positrons on the other hand mainly lose their energy through radiation and ionisation. The radiation process will only cause an energy deposition through recoiling nuclei or if the emitted radiation causes the electron energy to decrease below the cut off value in which case the electron transport seizes and all its energy is deposited on the spot. Again given the thickness of the active layer and the radiation length in silicon the occurrence probability of these processes is extremely small and these effects are thus negligible as well.

Finally the electrons and positrons lose energy through ionizations of the silicon atoms. As a charged particle traverses a layer of silicon it will inevitably lose energy through collisions with the present atoms. In these collisions a certain fraction of the energy will be transferred from the particle to the electrons and nucleus of the atom. It can be shown that the recoil of the nucleus can be neglected compared to the energy transfer to the atomic electrons. Depending on the magnitude of the energy transfer the electron that receives the energy will move to a higher energy level or is completely freed from the atom respectively exciting or ionizing the atom. In case of excitation the atom will emit a soft photon that will quickly be absorbed in the vicinity resulting in a low energy free electron that constitutes part of the charge collected in the detector. In case of ionization the free electron is referred to as a δ-ray. These δ-rays will then in turn lose their energy through excitation and ionization of the medium. The overwhelming majority of the collisions are however very soft and result in extremely low energy δ-rays that directly constitute the charge that is collected in the chip.

Since the collisions occur in a continuous fashion during the traversal of the medium this process is also significant in thin layers. Moreover ionization is the process through

which the vast majority of energy is deposited in the chips.

3.2.1.1 Average ionization energy loss

First of all treating the collisional energy loss as a continuous process is done in the following manner. If the energy of the incident positron or electron is large compared to the atomic electron binding energy the medium can be considered a cloud of quasi free electrons. The average energy loss per collision of a light lepton with energy (E) through collisions with an energy transfer (T) between 0 and the maximal transferable energy T_{max} is given by

$$E_{loss}(E) = \int_0^{T_{\max}} \frac{d\sigma(E,T)}{dT} T dT \tag{3.6}$$

For electrons the Møller scattering cross section is used while for positrons the Bhabha cross section is implemented. The maximal transferable energy is $0.5E$ for an electron due to the identity of the interacting particles and E for a positron. However since in the simulation the δ-rays with energy above 10keV are explicitly generated and transported through the geometry quantity (3.6) is not of much interest. Rather the average collisional energy loss through soft collisions with an energy transfer T below the δ-ray energy cut off value $E_{CUT,\delta}$ (10keV in most of the FoCal simulations presented in this thesis) is of interest. This quantity is given by

$$E_{loss}^{soft}(E) = \int_0^{E_{CUT,\delta}} \frac{d\sigma(E,T)}{dT} T dT \tag{3.7}$$

From expression (3.7) the so called Berger-Seltzer formula can be derived [3], which is the equivalent of the Bethe-Bloch formula for electrons and positrons.

$$\frac{dE_{tot}}{dx} = \frac{2\pi r_e^2 m_e \rho N_A Z}{\beta^2 A}\left[\ln\frac{m^2(2\tau+4)}{I^2} + F^{+}(\tau,\Delta) - \delta\right] \tag{3.8}$$

with

$m_e =$ electron mass [MeV]

$r_e =$ $2.8\cdot10^{-13}$ [cm], classical electron radius

$\tau =$ $\frac{E_K}{m_e}$ kinetic energy of incident particle in electron mass units

$\varepsilon =$ $\tau + 1$ total energy in electron mass units

$\tau_c =$ $\frac{E_{CUT,\delta}}{m_e}$

$\tau_{\max} =$ maximum possible energy transfer in e^-mass: τ for e^+, $\tau/2$ for e^- [MeV]

$\Delta =$ $\min(\tau_c, \tau_{\max})$

$\beta^2 =$ $1 - \frac{1}{\varepsilon^2}$

$E_{CUT,\delta}$= energy cut for $e^{\pm}$ [MeV]

ρ = density of the medium [gr/cm^3]

N_A = Avogadro number

Z = atomic number medium

A = atomic mass medium

I = $16\cdot10^{-9}Z^{0.9}$ [MeV], average mean ionisation energy medium

δ = density effect correction, see bellow

in which the functions $F^{\pm}$ are given by the following expression for the positron and electron respectively [4].

$$F^{+}(\tau,\Delta)=\ln(\Delta\tau)-\frac{\Delta^2}{\tau}\left[\tau+2\Delta-\frac{3\Delta^2 y}{2}-(\Delta-\frac{\Delta^3}{3})y^2-(\frac{\Delta^2}{2}-\tau\frac{\Delta^3}{3}+\frac{\Delta^4}{4})y^3\right]$$
$$F^{-}(\tau,\Delta)=-1-\beta^2+\ln\left[(\tau-\Delta)\Delta\right]+\frac{\tau}{\tau-\Delta}+\frac{1}{\varepsilon^2}\left[\frac{\Delta^2}{2}+(2\tau+1)\ln(1-\frac{\Delta}{\tau})\right] \quad (3.9)$$

with $y = 1/(\varepsilon+1)$. The δ term represents a correction for the density effect and does not derive directly from the scattering cross section. The density effect is effectively a reduction in the average energy loss due to a polarization of the medium. As the electron or positron traverses the medium the constituents of the medium will polarize decreasing the effective range of the electric field of the lepton. This decrease prevents any long distance energy transfers and therefore lowers the average energy loss. The density effect term is determined as follows [5]. First the parameter x is introduced

$$x=^{10}\log(\beta\varepsilon)=\frac{1}{2}\,^{10}\log[\tau(\tau+2)] \quad (3.10)$$

Now the density effect correction term is given by

$$\begin{aligned}
&\delta(x)=0 && x<x_0\\
&\delta(x)=4.6052x+a(x_1-x)^m+C && x_0\le x\le x_1 \quad (3.11)\\
&\delta(x)=4.6052x+a(x_1-x)^m && x_1<x
\end{aligned}$$

where the parameters C, a and m can be found in article [4] for different materials.

The formula can also be applied to low energy incident electrons and positrons. This scenario unfolds when the particle has approximately the same velocity as the bound atomic electrons in which case the so called shell correction term needs to be implemented. This shell correction term takes into account the fact that the atomic electrons in the innermost shells do not interact with the incident particle at these energies. In this regime the density effect can be neglected. Note that this shell correction term is merely an approximate parameterization since the fundamental assumption of scattering on a cloud of quasi free electrons does no longer hold in this scenario. A more thorough approach of such a scenario would explicitly take into account the atomic structure of the medium.

3.2.1.2 Energy straggling

The previous discussion on the collisional energy loss of electrons and positrons exclusively deals with the average energy loss of the particles as they traverse a medium. However this quantity is subject to fluctuations. This effect is also known as energy straggling. The fluctuations in the amount of energy lost in a certain thickness of material are caused by fluctuations in both the number of collisions and the energy transfer per collision. There exist several models that describe these fluctuations, each one with its own validity range as specified in the following section. Roughly speaking for a relatively large number of collisions the statistical theories can be applied like the one proposed by Landau and Vavilov. However as the thickness of the material traversed becomes smaller effectively reducing the number of collisions, the detailed nature of the atomic structure becomes important in determining the fluctuations of the energy loss. In this scenario the passage of a particle is no longer a statistical event but rather the sum of a fairly small number of interactions calling for a detailed description of the individual interactions. The energy loss distributions that are derived from the statistical models all resemble the shape depicted in Figure 15. The peak value of the distribution is called the most probable energy loss, which is significantly lower then the average energy loss as calculated earlier due to the tail of the distribution. This tail is caused by the high energy δ-rays that are formed in high energy transfer collisions that occur with a small probability.

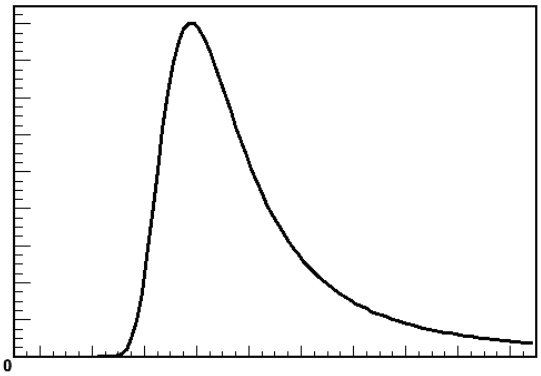

Figure 15: General shape of the collisional energy loss distribution

3.2.1.3 Energy straggling models

Next several models that are used in GEANT to simulate the energy loss fluctuations are presented. First of all the Landau model can be applied if two conditions are satisfied. The first being that the typical total energy loss upon traversal is small compared to the maximal possible energy loss in a single collision. So for an electron the energy loss upon traversal should be much smaller then half of its energy. This implies that no energetic δ-rays are created. Secondly said energy loss should be large compared to the binding energy of the innermost electron shells. This establishes the validity of the assumption of scattering

on a cloud of quasi free electrons. If this is not the case more detailed models taking into account the atomic structure are needed to accurately estimate the energy loss. The Landau distribution for electrons and positrons in this context is given by [6]

$$f(\varepsilon,t) = \exp(-\alpha^{\pm}(\lambda + \ln\alpha^{\pm}))\frac{\phi(\lambda)}{\zeta} \tag{3.12}$$

where

$\phi(\lambda) = \frac{1}{2\pi i}\int_{c-i\infty}^{c+i\infty} \exp(u\ln u + \lambda u)du$ $\quad c \geq 0$ universal Landau distribution

$\lambda = \frac{\varepsilon}{\zeta} - 1 - \nu - \beta^2 - \ln\frac{\zeta}{E_{\max}}$

$\zeta = 0.1535\frac{Z\rho}{A\beta^2}t$

t = thickness layer

$\nu = 0.422784$ (1-Euler's constant)

$\varepsilon =$ actual energy loss

$E_{\max} =$ maximal energy loss in single collision

$\alpha^{\pm} = c^{\pm}(\zeta / E)$

$c^{+} = \beta^2\left[2 - \frac{1}{(\gamma+1)^2}\right]$

$c^{-} = \frac{2\gamma - 1}{\gamma^2}$

The most probable energy loss which significantly differs from the average energy loss due to the Landau tail is given by [6]

$$\lambda_{mp}^{\pm} = \zeta\left[\ln\frac{2m_e\beta^2\gamma^2}{I^2} + \ln\frac{\zeta}{I} + 0.2 - \beta^2 - \delta\right] - 2.8\alpha^{\pm} \tag{3.13}$$

A problem with the Landau distribution is that its average value is infinite. For particle transversel with a high number of high energy transfer collisions this would lead to asymmetric fluctuations. However since the model is only valid for traversals with a relatively low number of energetic collisions this effect is negligible.

Next the more complicated Vavilov distribution is more accurate for it does not rely on the assumption of a negligible amount of high energy transfer collisions as will become clear in the following section where the validity regions of the models are discussed. Furthermore it has been shown that the Vavilov distribution tends to the Landau distribution in the regime were the previously discussed assumption does hold.

When the number of high energy collisions increases even further and the particle loses almost all of its energy upon traversal the Vavilov distribution tends to a Gaussian distribution. Since this is of no relevance for the description of thin layers. This scenario will not be discussed in more detail here.

For very thin layers the energy loss of an electron or positron upon traversal is no longer the sum a large number of small energy losses. Therefore statistical theories like the Landau or Vavilov model do no longer apply and GEANT resorts to the default Monte Carlo

model called the Urbán model [7]. This model assumes the atoms have two energy levels. Each interaction of the particle with the atom causes an excitation or an ionisation with probabilities distributed according to a set of parametrized formulas. For larger layer thicknesses the distribution generated by this model approaches the Landau theory.

Finally for very thin layers the more advanced photo absorption ionization (PAI) model can also be applied in GEANT simulations. This model uses the photoelectric cross-sections to describe the energy loss distribution. As for the Urbán model the width and the most probable value of the energy loss closely match the Landau and Vavilov models for relatively thick layers. In the PAI model the energy loss is derived by considering the total energy transfer as the sum of the energy transfers in the electromagnetic interactions between the particle and the atomic electrons. In the derivation, the atomic transition current is considered as the sum of the transition currents of its electrons. The PAI model though more accurate then the Urbán model is slower and therefore not the default model in GEANT. A comparison of the PAI model with experimental data can be found in [8].

3.2.1.4 Validity regions models

Which model describes the collisional energy loss most accurately depends strongly on the relative importance of high and low energy transfer collisions and the absolute number of collisions upon traversal. These quantities can be established using the following estimates

$\left\langle E_{loss,t} \right\rangle = \frac{dE_{tot}}{dx} t$ average energy loss by the particle in a layer of thickness t according to the Berger-Seltzer formula

$E_{\max} =$ maximal transferable energy in a single collision, which equals E for a positron and 0.5E for an electron

$I =$ typical electron binding energy as defined and parametrized previously as the average ionization potential

$\kappa = \frac{\left\langle E_{loss,t} \right\rangle}{E_{\max}}$ relative importance of high energy transfer collisions in the ionisation process

$\Phi = \frac{\left\langle E_{loss,t} \right\rangle}{I}$ estimation of the number of collisions with energy close to the ionisation energy

The boundaries of different validity regimes are slightly arbitrary and the boundaries presented here are based on the choices made in the GEANT simulation software [4].

1. large number of low-energy collisions: $\Phi \geq 50$

if δ-rays generation is requested the Urbán model is used. If δ-rays are not produced

three regions are distinguished:

- very few energy transfers close to the maximum: $\kappa \leq 10^{-2}$
  the Landau distribution is used;
- few energy transfers close to the maximum: $10^{-2} < \kappa \leq 10$
  the Vavilov distribution is used;
- many energy transfers close to the maximum: $\kappa > 10$
  the Gauss distribution is used;

2. small number of low-energy collisions: $\Phi < 50$

The model used is chosen directly by the user. As default the Urbán model is used, while on request the PAI model is implemented as was done in all the simulations presented in this thesis.

3.2.1.5 Implementation in GEANT

In the FoCal simulations presented here the electrons and positrons are transported through many different layers. The particles are transported through the tungsten absorbers in multiple steps due to the thickness and high density of these layers. Between the absorbers the particles are also transported through many thin layers of which the epitaxial layer of the chips is of paramount importance to the detection purposes. This layer is so thin (30μm) that particles are transported through them in a single step, which will be discussed in more detail in the next section.

Now for each step the collisional energy loss needs to be determined. As described this energy loss is due to the creation of δ-rays. However the cross section for the generation of δ-rays increases strongly as the δ-ray energy decreases. Concluding in reality a large number of electrons will just receive enough energy to escape from the atom. As with other numerous low energy particles in the simulation of em-showers the δ-rays cannot be explicitly generated down to arbitrary low energies since this would take too much computation time. As for all particles in the simulation there is an energy cut off for the δ-ray generation. The δ-rays with energy above this cut off are generated explicitly using the cross section for Møller or Bhabha scattering. The low energy δ-rays underneath the energy cut off contribute to the continuous energy loss of the traversing particle. The total energy loss of the particle due to these numerous low energy transfer collisions is simulated using a combination of the Berger-Seltzer formula and one of the energy straggling models described above.

An important topic in this context for the user to decide on is how to set the δ-ray cut off value. This energy should be set as low as possible for most realistic results however if this takes too much computing time one has to make sure the range of the δ-rays at the cut off value energy is not too large for reasons explained below. Considering the energy straggling the Landau, Vavilov and Gauss models are only used when the number of energetic δ-rays is very small. So the cut off value is of no importance to these models. The Urbán and PAI model explicitly take into account the δ-ray cut off value in order to prevent double counting the energy lost to the explicitly generated particles.

Finally the user can choose not to simulate the δ-rays at all and just rely on the high energy tail of the energy straggling models to take into account the production of these δ-rays. Note that in this scenario the energy loss of the particles can still be accurately approached. However, the total energy deposition in a certain layer might be influenced by this choice, for δ-rays with a high energy might escape the layer or volume depositing their energy in adjacent volumes. If these δ-rays are not simulated explicitly this energy loss will be considered part of the energy deposition of the incident particle. For large volumes and thick layers this problem is not so urgent for only a very small fraction of the total deposited energy would possibly escape. Here the important difference between the energy loss and the energy deposition of a particle in a single step becomes evident. The energy deposition does not equal the energy loss under all circumstances. The energy deposition is the energy loss of the particle in a step minus all the energy lost to particles that are explicitly generated and transported. This can be δ-rays but also radiation photons for electrons and positrons. Thus when just the energy loss of the incident particle is important ignoring the high energy δ-rays is fine and effective for saving computing time. However when the exact energy deposition is of importance as in the simulations described in this thesis the explicit generation of such particles is important.

Note that the precise energy deposition is important, since it determines the amount of charge generated in a pixel. This amount of charge is then compared to the discriminator value of said pixel to determine whether a signal occurs.

3.2.2 Simulation results

The results from actual shower simulations are not very useful for comparison with the theory of the thin layer energy deposition as presented previously for the following reason. The amount of energy deposited depends strongly on the path length of the traversing particle. As this path length increases significantly for the shower particles traversing the chips at large angles the energy deposition characteristics are convolved with an angular distribution that is not known. Therefore these results are useful for qualitative considerations of rough characteristics; however for a quantitative analysis of the energy deposition mechanisms an alternative simulation was run. This simulation will be discussed first.

The thin layer simulation executed using the FocalPedestal version consisted of 1000 events each with 500 electrons incident perpendicularly on a 45μm thick silicon layer. This thickness was chosen because it approximates the average path length of the shower particles through the active chip layers. The energy of the primary electrons was distributed uniformly from 0 to 5MeV since this is the energy range of the particles that deposit the overwhelming majority of the energy in the actual shower simulation as will be shown in Panel 3 and 4 of Figure 17. Apart from the primary particles and the geometry the simulation settings were chosen identical to those of the shower simulations. In the following only the electron behaviour in thin layers is discussed since this is nearly identical to the positron behaviour in thin layers.

First it is important to establish what the recorded energy depositions represent. An energy deposition is saved if the electron lost a certain amount of energy which was not transferred to particles that were explicitly generated. This energy deposition is saved at the end location of the step. GEANT determines the step size for a particle in a material based on the known free path length at the given energy except for when the boundary of a volume is reached before the end of the step. In this scenario the step is ended at the boundary. Upon examining the tracks of multiple events it turns out that the energy depositions in the chips epitaxial layer as measured in the simulation appear exclusively on the edge of said volumes. In addition the total number of depositions is only about 1% larger then total number of primaries, so only a negligible amount of δ-rays is explicitly produced. This leads to the conclusion that the depositions are the total energy loss of the particles caused by the traversal of the entire 45μm of silicon.

Any energy losses due to radiation are negligible since the energy of the particles under investigation is beneath 5MeV a regime where ionization cross section is much larger then the radiation cross section. This can also be verified using the tables of article [3] were it becomes evident that the radiation losses are of the order 10^{-2} compared to the collisional energy losses. Concluding the overwhelming majority of the traversing electrons leave a single energy deposition and that deposition represents the total energy deposition due to ionizing collisions and can therefore directly be compared to the previously discussed energy loss and straggling theories.

First of all the electron formula (3.8) can be used to determine the average total collisional energy loss in the layer. In this formula the 10keV δ-ray energy cut off value is applied to match the simulation settings. Any δ-rays with higher energy are explicitly generated. This happens for 1% of the incident electrons, since the number of energy depositions is found 1% higher then the number of primaries. The following values for a 45μm thick silicon layer were implemented

$m_e =$	0.511MeV	$\rho =$	$2.323\ \text{gr/cm}^3$
$r_e =$	$2.8\cdot10^{-13}\ \text{cm}$	$N_A =$	$6.022\cdot10^{23}$
$\tau =$	$\frac{E_K[MeV]}{0.511\text{MeV}}$ kinetic energy	$Z =$	14
$\varepsilon =$	$\tau+1$	$A =$	28
$\beta^2 =$	$1-\frac{1}{\varepsilon^2}$	$\delta =$	density effect correction, see bellow
$I =$	$173\cdot10^{-6}\ \text{MeV}$	$\Delta =$	$\tau_c = 0.020$
$\tau_c =$	$\frac{0.01}{0.511} = 0.020\text{MeV}$		

to arrive at the following expression for the collisional energy loss. Note that as a convention *E* is the kinetic energy of the incident electron in all of the following

$$\frac{dE_{tot}}{dx} = \frac{0.21}{(1-(\frac{0.511}{E_K+0.511})^2)}\left[\ln\frac{1.02E_K+1.04}{173\cdot10^{-6}} + F^-(E_K,0.020) - \delta(E_K)\right] \tag{3.14}$$

with

$$F^-(E_K,0.020) = -1-\left(1-\left(\frac{0.511}{E_K+0.511}\right)^2\right)+\ln\left[0.039E_K-4\cdot10^{-4}\right]+\frac{1.96E_K}{1.96E_K-0.020}+ \left(\frac{0.511}{E_K+0.511}\right)^2\left[2.0\cdot10^{-4}+(3.92E_K+1)\ln\left(1-\frac{0.020}{1.96E_K}\right)\right] \tag{3.15}$$

For the density effect in silicon the constants C = -4.4351, x_0 = 0.2014, x_1 = 2.8715, a = 0.14921 and m = 3.2546 are retrieved from [5]. Prior to the determination of the δ correction term the validity regimes of this term is determined using (3.10) and (3.11).

$$\begin{aligned} \frac{1}{2}\log\left(\frac{E_K}{0.511}\left(\frac{E_K}{0.511}+2\right)\right) < 0.2014 \quad &\Rightarrow \quad E_K < 0.45\text{MeV} \\ 0.2014 \le \frac{1}{2}\log\left(\frac{E_K}{0.511}\left(\frac{E_K}{0.511}+2\right)\right) < 2.8715 \quad &\Rightarrow \quad 0.45\text{MeV} \le E_K \le 380\text{MeV} \end{aligned} \tag{3.16}$$

Now from (3.11) follows directly for the density effect correction term

$$\begin{aligned} \delta(x) &= 0 && E_K < 0.45\text{MeV} \\ \delta(x) &= 4.6052x + (2.8715-x)^{3.2546} - 4.4351 && 0.45 \le E_K \le 380\text{MeV} \end{aligned} \tag{3.17}$$

with *x* defined by (3.10). Next by combining (3.14), (3.15) and (3.17) the average energy loss formula can be determined. This formula is shown in Panel 4 of Figure 16 together with the average energy deposition that was determined from the total energy deposition spectrum shown in Panel 1 of said Figure. The discontinuity in the graph is caused by the validity region boundary of the density correction term as determined in (3.17). The horizontal errors correspond to the width of the track energy bins and the vertical errors to the error of the mean of the energy deposition distribution for each track energy bin. As can be seen the average energy deposition matches the predictions by (3.14), (3.15) and (3.17) very well for the 800keV to 5MeV electron range. For the less energetic electrons the simulated average energy deposition are roughly 30% too high.

Next it is important to determine what model GEANT implements for the simulation of the energy loss in the chips. In order to do so the quantities κ and Φ are determined that represent the number of high and low energy transfer collisions respectively. Doing so for the 200keV electrons an average energy loss of approximately 40keV can be determined from the function in Figure 16 panel 2 thus giving the following values for κ and Φ

$$\kappa = 40\text{keV} / 100\text{keV} = 0.4$$
$$\Phi = 40\text{keV} / 173\text{eV} = 231$$

Therefore according to the section on the validity regions of the energy straggling models the Vavilov model will be applied for these particles. For the 5MeV electrons on the other end of the spectrum an average energy loss of 15keV is found from Figure 16 panel 2.

$$\kappa = 15\text{keV} / 2.5\text{MeV} = 0.006$$
$$\Phi = 15\text{keV} / 173\text{eV} = 87$$

Thus for the higher energy electrons the Landau model is implemented by GEANT. This allows for a comparison of the most probable energy loss according to the Landau distribution as given by (3.13). For electrons this expression transforms to

$$\lambda_{mp}^{-} = \zeta\left[\ln\beta^2\gamma^2 + \ln\zeta + 26.2 - \beta^2 - \delta\right] - 2.8\left(\frac{2\gamma-1}{\gamma^2}\right)\frac{\zeta}{E} \tag{3.18}$$

This expression is shown in Panel 2 of Figure 16 together with the most probable energy deposition as determined from the total energy deposition spectrum visible in Panel 1 of said Figure. The horizontal errors correspond here to the track energy bin size and the vertical errors to the width of the energy deposition bins. As can be seen the most probable energy deposition is fairly accurate for the electrons below 600keV, however for the higher electron energies up to 5MeV the simulated most probable energy loss is about 10 to 20% too high.

Finally in Panel 3 of Figure 16 a cross section of the energy deposition spectrum at 2MeV track energy is shown. Comparing the Landau fit to the distribution it is evident that at 2MeV the energy depositions are indeed distributed following a Landau distribution. Considering Panel 1 of said Figure it becomes clear that this distribution is almost constant for all electron energies ranging from 1.5 to 5MeV. This is also apparent given the average energy deposition and the most probable energy loss are almost constant in this energy range.

In Figure 17 the energy deposition spectra are shown of an actual shower simulation. This simulation consisted of 1000 events of a single shower caused by a 5GeV incident electron. The difference between this simulation and the thin layer simulation discussed previously is merely the geometry and the primary particle settings. Each energy deposition that is present in the data set occurred in the epitaxial layer of one of the 96 MIMOSA chips. This epitaxial layer is 30μm thick in this scenario. As mentioned before the data presented in Figure 17 is constituted by 150000 electron energy depositions while the positron data consisted of approximately 100000 energy depositions in total. This gives roughly 250 energy depositions in the chips per event. No energy depositions by photons were considered for reasons discussed in the previous section and which is validated by the fact that in a 1000 simulated events only 400 photon energy depositions occurred.

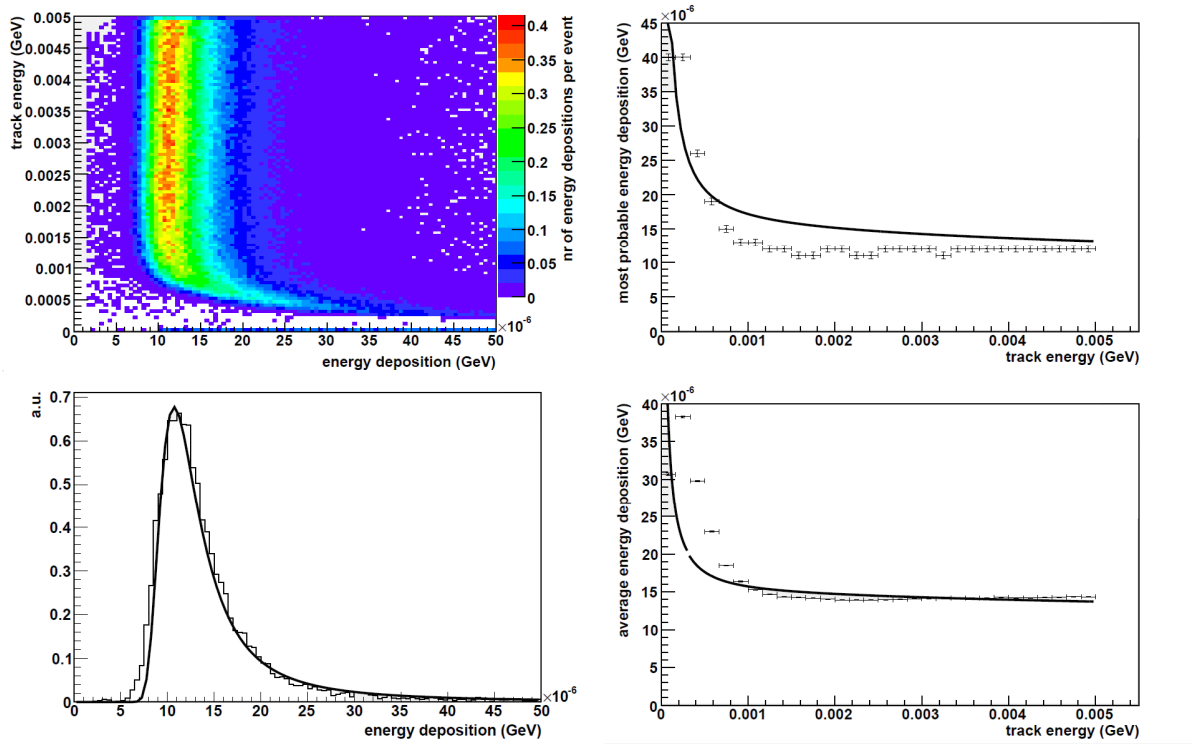

Figure 16: Panel 1 (up left), energy deposition spectrum of thin layer simulation consisting of 1000 events each with 500 primary electrons incident on a 45micron thick Si layer. Panel 2 (up right), Most probable energy loss for the traversing electrons as a function of track energy fitted with formula (3.18). Panel 3 (down left), Distribution of energy depositions for approximately 2MeV electrons fitted with landau distribution. Panel 4 (down right), Average energy loss of the electrons as a function of track energy fitted with formula (3.14)

In Panel 1 and 2 the energy deposition spectra for the electrons and positrons are shown for a wide energy deposition and track energy range. It is obvious here that the overwhelming majority of the energy depositions is smaller then 50keV and that by far the largest portion of the energy is deposited by particles with an energy below 10MeV. This is expected for two reasons. First the low energy electrons and positrons are much more numerous then the higher energy particles for obvious reasons. Secondly the cross section for the ionization process increases dramatically at low energy causing the low energy particles to lose relatively more energy upon traversal.

Panel 3 and 4 show the energy deposition spectra for the low energy (<10MeV) electrons and positrons respectively. First it is important to note the different colour scales for both figures. This shows that the electrons are more numerous then the positrons at low energies. Also the electron flux greatly increases as the track energy decreases as is apparent from panel 3. This is logical since low energy electrons are produced through several different processes. This is not the case for the positrons that are only created in the pair production process that occurs at higher energies, which explains the more uniform distribution of the positron flux. The positrons are namely created at higher energies relatively early in the shower. As the shower develops the high energy positrons gradually

lose their energy while their number remains nearly constant for annihilation processes only take over at very low energies. In addition the rise of the most probable energy and the average energy deposition are not observed for the positrons since the positron flux drops rather abruptly below 1MeV.

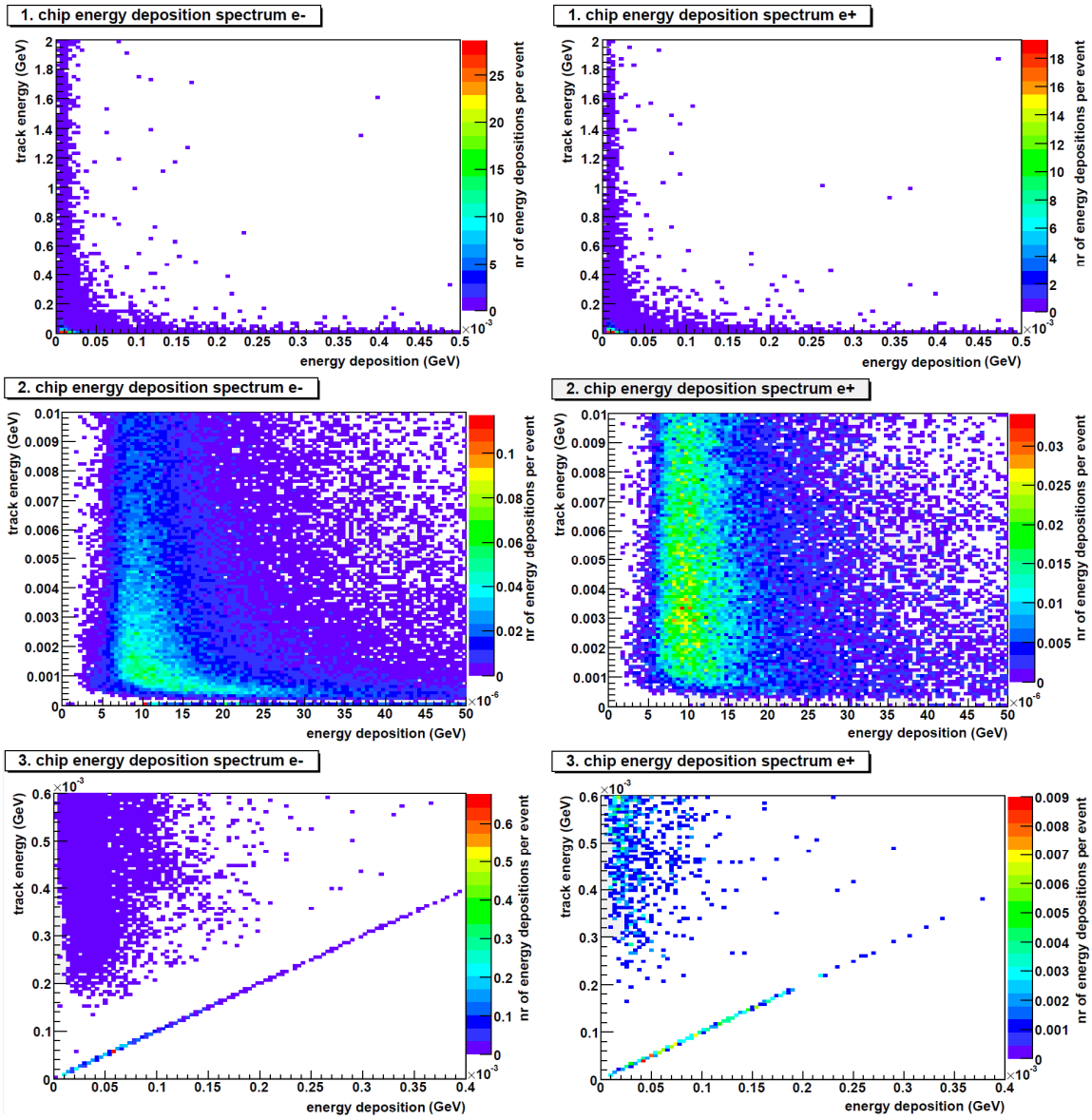

Figure 17: Panel 1,3,5 (left from top to bottom) different regimes of the energy deposition spectrum of the electrons. Panel 2,4,6 (right from top to bottom) different regimes of the energy deposition spectrum of the positrons.

The average energy deposition of the electrons in the 2 to 5MeV range equals roughly 12keV as can be seen in panel 3. This is about 3keV lower then the average energy deposition found in the thin layer simulation presented in Figure 16. From this can be

deduced that the average path length of the electrons is smaller then 45microns, which was the path length in the thin layer simulations. This is also apparent from the relative position of the most probable energy deposition which is about 3keV lower for the shower simulations as well.

Finally in panel 5 and 6 a peculiarity directly caused by the simulation algorithm is shown. A clear line is visible constituted by energy depositions of which the size matches the track energy. As a particle loses so much energy in a single step that the remaining kinetic energy of the particle lays below the energy cut off value of 10keV the particle transport is terminated and all of its energy is deposited at the end point of said step. This effect causes the particles that in reality would lose almost all their energy to lose also their remaining energy if this happens to be less then 10keV, causing the average energy loss for these particles to be slightly higher then in reality.

3.3 Shower shape analysis

The high spatial resolution of the MIMOSA chips offers a unique insight into the development of electromagnetic showers in the detector. The distribution of the energy depositions throughout the detector also referred to as the shape of the shower can be used to identify particles and their energies. Moreover the shower shape offers detailed comparison opportunities of the simulations with the actual detector.

3.3.1 Theoretical background

The longitudinal shower shape is mostly considered using the longitudinal distribution of the energy deposition in the detector. The shower shape can also be described using the particle flux as a function of the shower depth, however this would introduce parameters like the particle energy and type which would complicate matters. Furthermore in an actual detector the energy depositions can be measured easily as opposed to the particle fluxes that only manifest themselves through energy depositions. The fractional energy deposition as a function of the shower depth roughly resembles the shape depicted in Figure 18.

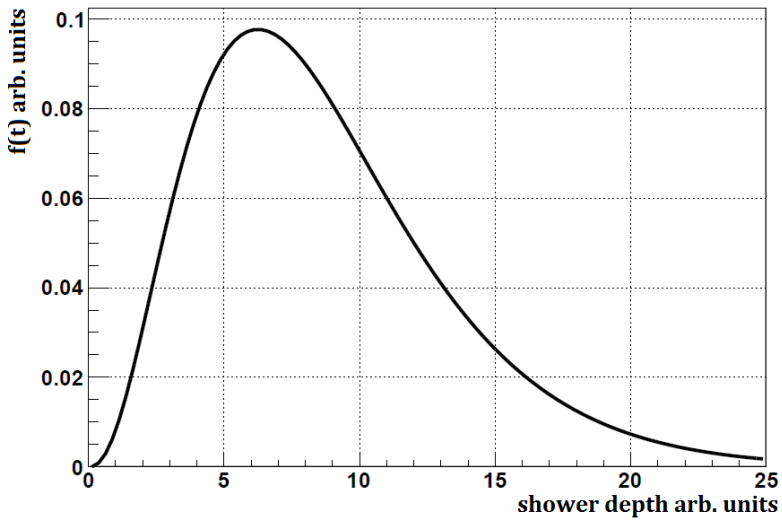

Figure 18: longitudinal shower profile with shower depth and $f(t)$ in arbitrary units

The energy is deposited primarily by low energy particles. The flux of these particles grows exponentially in the early development of the electromagnetic cascade due to the particle multiplication processes discussed above. Subsequently as the average energy of particles in the shower reaches the critical energy the particle multiplication stops and the particle flux reaches its maximum causing the energy deposition profile to also reach its maximum. Finally after the shower maximum the particle flux and with it the energy deposition per depth increment decreases since the soft particles in the shower are absorbed and there is no more particle multiplication.

In order to describe the longitudinal shower profile in an approximately material independent way the scaling variable referred to as the radiation length is introduced. Since high energy particles lose the same fraction of energy every consecutive radiation length, the average energy of the shower particles is roughly proportional to their depth in the detector. So the general longitudinal shower characteristics should scale with the radiation length and allow a material independent description of the longitudinal shower profile. However the scaling with the radiation length is not perfect. It turns out that as the Z of the absorber material increases the decay rate after the shower maximum decreases and the shower maximum shifts to greater depths in the detector. The shift of the maximum is caused by the lower critical energy of high-Z materials. The lower critical energy causes the particle multiplication to continue till lower average energy, which corresponds with a larger number of radiation lengths.

The transversel development of the electromagnetic showers is also considered through the energy deposition profile for the same reasons as the longitudinal profile. The energy deposition as a function of depth roughly resembles the shape in Figure 19.

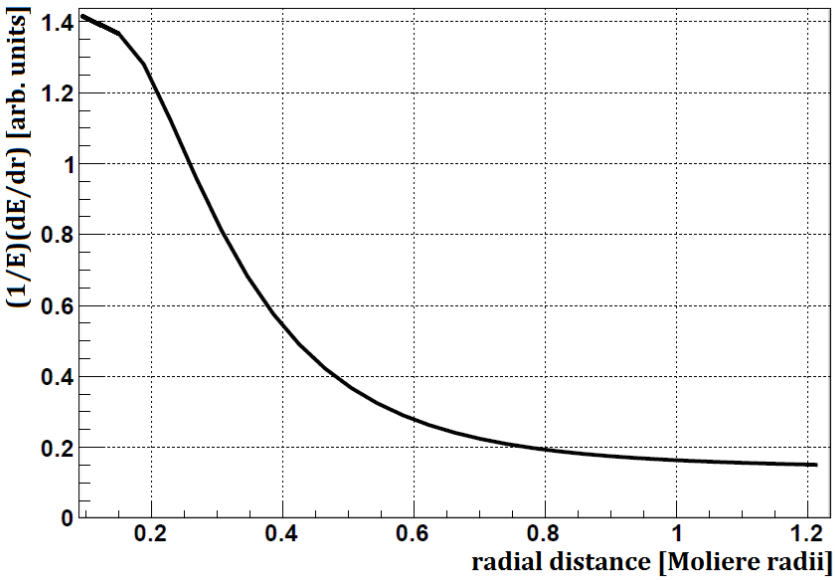

Figure 19: radial shower profile

As expected the bulk of the total energy is deposited on or close to the shower axis and the deposition diminishes quickly with the radial distance. The transversel spread is caused by two effects:

- High energy electrons and positrons obtain a transversel momentum component through multiple coulomb scattering. This component will be relatively small compared to the total momentum.
- Relatively low energy photons and electrons produced in processes like the photo-electric effect, bremsstrahlung and Compton scattering will also obtain a lateral momentum component.

The first process is dominant in the early development of the shower while the second process is dominant after the maximum. These two effects manifest themselves in an obvious way in the radial profile in Figure 19. In this figure two components can be distinguished. The central core component that drops of steeply at low radii and a halo component that decreases more slowly at larger radii. In this figure the lateral shower profile is integrated over the entire detector depth. However the core component should be most pronounced at small depths in the detector while the halo component should take over after the shower maximum with a mixture of both components around the shower maximum. These expectations will be reflected in the results presented below.

Finally since 90% of the shower energy is deposited within a single Molière radius from the shower axis this quantity couples the radial energy deposition to the radial distance. This allows an approximate material independent description of the radial profile. However, as Z increases the decrease of the energy deposition as a function of the radial distance becomes steeper. The high radius tail of the energy deposition profile is mainly caused by soft electrons from Compton scattering and the photo-electric effect. The photons that produce these electrons have a smaller mean free path in high-Z materials. Therefore in high-Z materials the showers will be slightly narrower. In addition the photo-electric

effect becomes the dominant process at much higher energies in high-Z materials. This causes absorption of the photons at higher energies preventing them from participating in Compton scattering processes that widen the shower.

3.3.2 Shower parametrization

In order to draw any quantitative conclusions on the shower shape the parametrization introduced in [2] is used to fit the longitudinal and radial shower profiles. Furthermore the parametrization offers a theoretical prediction on the shower profiles that is used as a consistency check of the simulation framework. The parametrizations presented in the article were developed based on GEANT simulations that approximately matched actual calorimetric data with a 1.5% accuracy.
The following parametrization as developed in [2] is applied. The spatial energy distribution is given by two probability density functions (pdf's) that describe the longitudinal and radial dependencies.

$$d^3E(\vec{r}) = E\, f(t)dt\; g(r,t)dr \tag{3.19}$$

Note here that t represents the depth in the detector and is expressed in radiation lengths (X_0) and r represents the radial distance from the shower axis and is expressed in Molière radii (ρ_M) for previously mentioned reasons. The energy distribution is assumed independent of the azimuthal angle. The longitudinal pdf is described by a gamma distribution and the radial pdf is described by a two-component Ansatz. Finally the radial distribution $g(r,t)$ obviously depends on the depth t since the shower starts out narrow and grows wider deeper into the detector.

3.3.2.1 Longitudinal parametrization

When considering the longitudinal pdf the energy is integrated over all radii at a certain depth. Thus the factor $g(r,t)dr$ =1 in (3.19). Moreover for $f(t)$ the gamma distribution is used as parametrization giving the following equation [2].

$$f(t) = \frac{(\beta t)^{\alpha-1}\beta e^{-\beta t}}{\Gamma(\alpha)} \tag{3.20}$$

with α the shape parameter and beta the scaling parameter. The maximum of $f(t)$ can be calculated setting $df(t)/dt$ equal to 0. This yields

$$T \equiv \frac{\alpha-1}{\beta} \tag{3.21}$$

with T the t-value of the maximum. From this point on the shape parameter α and the shower maximum T are used to define the longitudinal pdf. For a sampling calorimeter like FoCal the α and T can be parametrized in the following way [2].

$$T_{sam} = \ln y - 0.858 + 0.59F_S^{-1} - 0.53(1-\hat{e}) \tag{3.22}$$

$$\alpha_{sam} = 0.21 + (0.492 + \frac{2.38}{Z})\ln y - 0.444F_S^{-1} \tag{3.23}$$

The subscript *sam* indicates this expression is valid for sampling calorimeters. F_s is the sampling frequency

$$F_s = \frac{X_{0,eff}}{d_a + d_p} \tag{3.24}$$

with d_a and d_p the thicknesses of the active and passive layers respectively, which becomes for FoCal

$$F_{s,focal} = \frac{4mm}{3.8mm} = 1.053 \tag{3.25}$$

and $\hat{e}$ the *e/mip* ratio that can be approximated by

$$\hat{e} = \frac{1}{1 + 0.007(Z_p - Z_a)} \tag{3.26}$$

which becomes for FoCal

$$\hat{e}_{focal} = \frac{1}{1 + 0.007(74 - 14)} = 0.70 \tag{3.27}$$

Finally y in (3.22) and (3.23) is defined as

$$y = \frac{E}{E_c} \tag{3.28}$$

with E_c the critical energy as defined before. Using the *e/mip* ratio and the sampling fraction of FoCal (3.22) and (3.23) become

$$T_{sam} = \ln y - 1.577 \tag{3.29}$$

$$\alpha_{sam} = -0.212 + 0.524\ln y \tag{3.30}$$

The parametrizations (3.29) and (3.30) suggest a fit of the α and T simulation data to the following functions

$$\ln T_{sam} = \ln(\ln(y) - t_1) \tag{3.31}$$

$$\ln \alpha_{sam} = \ln(a_1 + a_2 \ln y) \tag{3.32}$$

Note here that the fit is conducted on the natural logarithm of α and T. This is done because it turns out that these quantities are distributed normally [2]. The fits can subsequently be compared to the logarithm of the predictions (3.29) and (3.30).

The approximate logarithmic dependency of the shower maximum T on the energy can be explained by the following reasoning. A high energy photon takes approximately 9/7 radiation length to convert to an electron and positron that both carry approximately half of the photons energy. Therefore, as the energy of a primary particle doubles the shower only shifts about $9/7X_0$ deeper into the detector. This implies a logarithmic relation of the shower depth with the incident energy.

The parametrization of the longitudinal profile deals with energy deposition per unit depth. However it is not a priori obvious how to apply this parametrization to the FoCal simulation data, since the Focal data merely consists of a number of hits per detector layer. This problem is tackled in the following way. The fraction of hits in a single layer is assumed to be proportional to the total energy deposition in that layer, which gives rise to the following expression

$$E\left\langle \frac{N_L(l)}{N_T} \right\rangle = E\, f(t)dt \tag{3.33}$$

were the average is taken over a large number of events. E is the total energy deposition in the detector, $N_L(l)$ the number of hits in layer l corresponding to depth t in the following way

$$t = \frac{3.8(l+0.5)}{X_0} \tag{3.34}$$

and N_T the total number of hits in the entire detector. The thickness of the layer is 3.8mm in the current FoCal design, so $dt = 3.8/X_0$, since t is the shower depth in radiation lengths. Using the effective radiation length as calculated previously $f(t)$ becomes

$$f(t) = \left\langle \frac{X_0 N_L(l)}{3.8 N_T} \right\rangle \tag{3.35}$$

In this fashion the discrete FoCal output is related to the continuous energy deposition distribution as described by the parametrizations. The fundamental assumption that is made here is that each pixel hit in the detector corresponds to an equal energy deposition that is approximately homogeneously distributed in a volume with a cross section of said pixel and a depth of a single layer (3.8mm). This assumption is obviously not infallible, which will also be reflected in the results.

3.3.2.2 Radial parametrization

The radial pdf is more complicated then the longitudinal one, since it also depends on the shower depth. For this reason the entire formula (3.19) needs to be applied. For the parametrization of *g(r,t)* the following two-component Ansatz is used following [2]

$$g(r,t) = pg_c(r,t) + (1-p)g_t(r,t) = p\frac{2rR_c^2}{(r^2+R_c^2)^2} + (1-p)\frac{2rR_t^2}{(r^2+R_t^2)^2} \tag{3.36}$$

with $0 \leq p \leq 1$. R_c is the median of the core component, R_t is the median of the tail component and p represents the relative weight of the core component. As previously mentioned these constants depend on the shower depth and can be parametrized as follows. For homogeneous calorimeters the expression for R_c is linear, however in the sampling scenario of FoCal there are some correction terms

$$\begin{aligned} R_{c,sam} &= z_1 + z_2\tau - 0.0203(1-\hat{e}) + 0.0397F_S^{-1}\exp(-\tau) \\ z_1 &= 0.0251 + 0.00319\ln E \\ z_2 &= 0.1162 - 0.000381Z \end{aligned} \tag{3.37}$$

The expression for the R_t and p parameter are quite complicated compared to the evolution of the R_c parameter. This can mainly be explained by the propagation of low energetic photons [9].

$$\begin{aligned} R_{t,sam} &= k_1(\exp(-2.59(\tau-0.645)) + \exp(k_2(\tau-0.645))) - 0.14(1-\hat{e}) - 0.495F_S^{-1}\exp(-\tau) \\ k_1 &= 0.659 - 0.00309Z \\ k_2 &= 0.3585 + 0.0421\ln E \end{aligned} \tag{3.38}$$

Finally the parametrization of the parameter p for a sampling calorimeter is given by

$$\begin{aligned} p_{sam} &= p_1\exp\left(\frac{p_2-\tau}{p_3} - \exp\left(\frac{p_2-\tau}{p_3}\right)\right) + (1-\hat{e})(0.348 - 0.642F_S^{-1}\exp(-(\tau-1)^2)) \\ p_1 &= 2.632 - 0.00094Z \\ p_2 &= 0.401 + 0.00187Z \\ p_3 &= 1.313 - 0.0686\ln E \end{aligned} \tag{3.39}$$

with

$$\tau = t / T$$

This scaling parameter is convenient for it separates the energy and material dependence of various parameters. F_s and $\hat{e}$ correspond again to respectively the *e/mip* ratio and the sampling fraction. Using the FoCal parameters these formulas take the following shape for 5 and 50GeV, which are the energies at which the radial profiles are presented in the results.

$$\begin{aligned} R_{c,sam}^{5GeV} &= 0.025 + 0.088\tau + 0.038\exp(-\tau) \\ R_{c,sam}^{50GeV} &= 0.034 + 0.088\tau + 0.038\exp(-\tau) \end{aligned} \tag{3.40}$$

$$\begin{aligned} R_{t,sam}^{5GeV} &= 0.430(\exp(-2.59(\tau-0.645)) + \exp(0.426(\tau-0.645))) - 0.042 - 0.470\exp(-\tau) \\ R_{t,sam}^{50GeV} &= 0.430(\exp(-2.59(\tau-0.645)) + \exp(0.523(\tau-0.645))) - 0.042 - 0.470\exp(-\tau) \end{aligned} \tag{3.41}$$

$$p_{sam}^{5GeV} = 2.56\exp(\frac{0.54-\tau}{1.20} - \exp(\frac{0.54-\tau}{1.20})) + 0.10 - 0.18\exp(-(\tau-1)^2)$$
$$p_{sam}^{50GeV} = 2.56\exp(\frac{0.54-\tau}{1.04} - \exp(\frac{0.54-\tau}{1.04})) + 0.10 - 0.18\exp(-(\tau-1)^2) \quad (3.42)$$

The expressions (3.40), (3.41) and (3.42) suggest a fit of the R_c, R_t and p data to the functions

$$R_{c,sam} = c_1 + c_2\tau + c_3\exp(-\tau) \quad (3.43)$$

$$R_{t,sam} = t_1(\exp(t_3(\tau - t_2)) + \exp(t_4(\tau - t_2))) + t_5 + t_6\exp(-\tau) \quad (3.44)$$

$$p_{sam} = p_1\exp(\frac{p_2-\tau}{p_3} - \exp(\frac{p_2-\tau}{p_3})) + p_4 + p_5\exp(-(\tau-1)^2) \quad (3.45)$$

These fits can then be compared to the parametrization predictions from (3.40), (3.41) and (3.42). As with the longitudinal profiles the parametrization of the radial profile as described above deals with energy deposition. Again it is not a priori obvious how to apply this parametrization to the FoCal simulation data, since the Focal data merely consists of a number of hits per cylindrical volume around the shower axis. This problem is approached in the following way. The fraction of hits in a cylindrical volume with non-zero inner radius and a fixed width is assumed to be proportional to the total energy deposition in that volume, which gives rise to the following expression.

$$E\left\langle \frac{N_c(c)}{N_T} \right\rangle = E\, f(t)dt\ \mathrm{g}(r,t)dr \quad (3.46)$$

Were the average is taken over a large number of events. E is the total energy deposition in the detector, $N_c(c)$ the number of hits in cylinder number c from the shower axis in the layer under consideration with width dr and N_T the total number of hits in the entire detector. As for the longitudinal profiles dt = 3.8mm/X_0 and dr can be chosen arbitrarily. In the results presented in the following section a cylinder with radius 1.2ρ_M is divided into 15 concentric cylinders. dr needs to be expressed in units of the Moliere radius and therefore

$$dr = \frac{w}{\rho_M} = \frac{1.2}{15} \quad (3.47)$$

with w the cylinder width. Formula (3.46) can now be rewritten as

$$g(r,t) = \left\langle \frac{N_c(c)}{N_T f(t)dtdr} \right\rangle = \left\langle \frac{3.29X_0N_c(c)}{N_T f(t)} \right\rangle \quad (3.48)$$

This way the discrete FoCal output is related to the continuous energy deposition distribution as described by the parametrizations in a similar manner as was done for the longitudinal distribution.

3.3.3 Simulation results

The results displayed in this section were obtained from simulations with primary electrons of various energies without any implemented background or noise. Also no discriminator threshold settings were applied. In all simulations 1000 events were generated and all particles were tracked down to the 10keV level, which is the minimal setting for GEANT3. The primary electrons all impinge perpendicular on the absorber of the first detector layer and they are uniformly distributed on a 1x1cm square centred on the first layer. This is important since there is a dead area between adjacent chips that will cause a systematic error if the primary particles all impinge on the same point. The square was not chosen any larger since at higher energies this would result in increased lateral shower leakage. The step size parameters or tracking parameters as they are referred to in the GEANT manual [4] were all calculated automatically by GEANT for consistency.

3.3.3.1 Longitudinal shower profiles

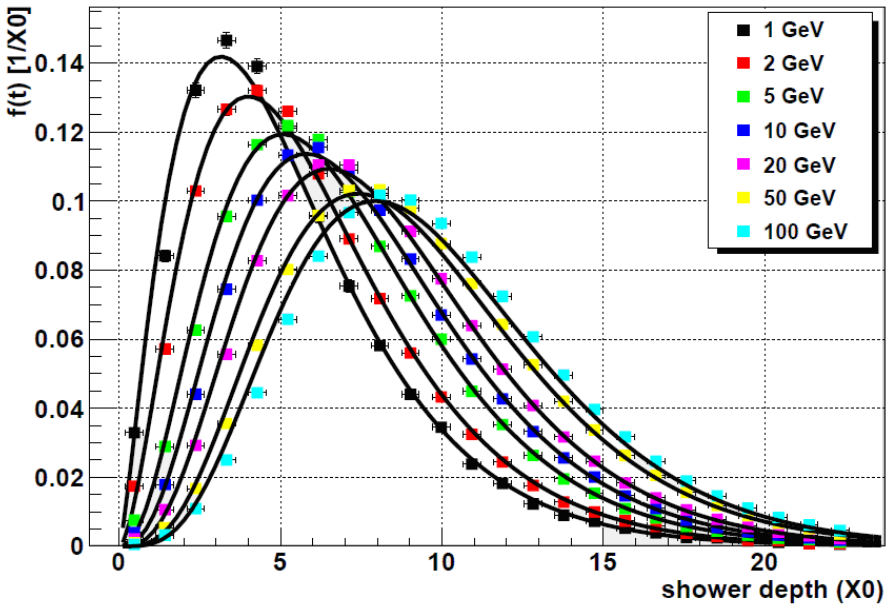

Figure 20: Longitudinal shower profile pdf $f(t)$ as a function of radiation length and its parametrization according to expression (3.20) for various electron energies.

For every detection layer the quantity $f(t)$ as defined in (3.35) was calculated with the average taken over all events. The resulting profiles were subsequently fit by expression (3.20). In Figure 20 the probability density profiles ($f(t)$) as a function of the shower depth in radiation lengths is displayed. The unit of the pdf is $[1/X_0]$ for in (3.35) the fraction of hits is divided by the thickness of a single layer in radiation lengths. This is done in order to allow comparison with the parametrization results as previously derived from [2]. The horizontal bars indicate 2/3 of the thickness of each layer and serve as a visual reference.

As expected for higher energies the shower maximum clearly shifts deeper into the

detector as becomes evident in Figure 20. Also the distribution widens considerably with increasing energy. This can be explained in the following manner. As the primary energy increases the number of radiation lengths needed before the average energy reaches the critical energy and thus the shower its maximum increases as well. In addition a higher total particle flux is reached causing a slower decay after the shower maximum. With increasing energy the quality of the fits decreases significantly. For the 1GeV fit a reduced χ^2 of 1.56 is found, while this value increases monotonous up to 5.74 for the 100GeV fit. For this reason the parametrization (3.20) of the longitudinal can be considered good for low energy showers E<20GeV and reasonable for higher energy showers.

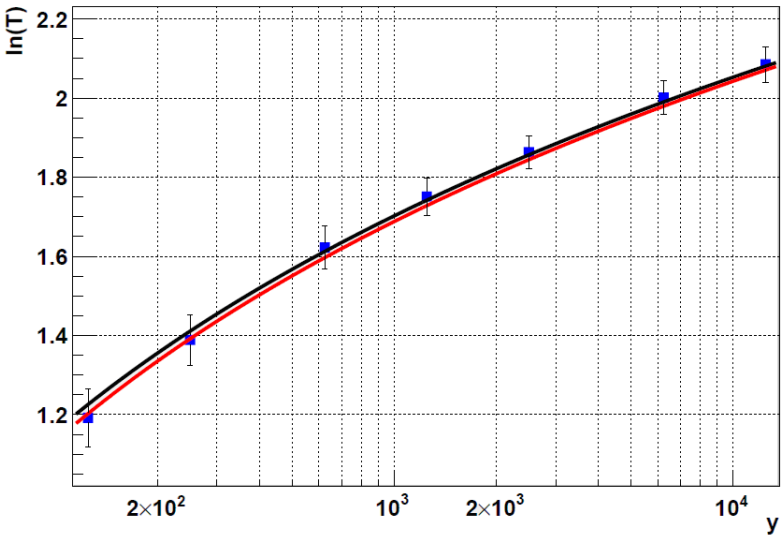

Figure 21: Shower maximum ln(T) vs. electron energy scaling variable $y = E/E_c$ as obtained from the longitudinal profiles depicted in Figure 20 including fit by expression (3.31) (black line) and parametrization prediction deduced from (3.29) (red line).

From each longitudinal fit in Figure 20 the α and β parameter were extracted. With these parameters the location of each shower maximum was determined using expression (3.21). The logarithm of the shower maximum is utilized here since this allows for a straight forward comparison with results from [2]. Subsequently a fit with formula (3.31) was applied (black line). The vertical errors were determined using the uncertainties of α and β from the fitting algorithm in combination with simple error propagation rules. There are no horizontal errors present since the primary electron energy in the simulations has a fixed value. Though slightly low the parametrization (3.29) (red line) as calculated in [2] matches the data very well. In addition the data matches the data presented in Figure 5 of [2] very closely.

From each longitudinal fit in Figure 20 the α parameter was extracted. The logarithm of the α parameter is utilized here since this allows straight forward comparison with results from [2]. Subsequently a fit with formula (3.32) was applied (black line) to allow comparison with the predictions from [2]. The vertical errors were determined using the uncertainty in α from the fitting algorithm in. There are no horizontal errors present since the primary electron energy in the simulations has a fixed value. The parametrization (3.30)

(red line) as proposed in [2] again matches the data closely. Concluding the parametrizations proposed for the longitudinal shower profiles are very well applicable to the FoCal data.

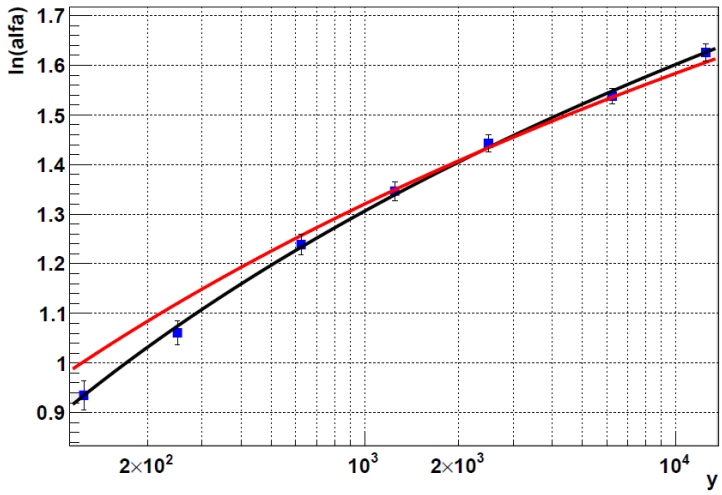

Figure 22: Shape parameter ln(α) vs. electron energy scaling variable $y = E/E_c$ as obtained from the longitudinal profiles depicted in *Figure 20* with fit by expression (3.32) (black line) and parametrization prediction deduced from (3.30) (red line).

3.3.3.2 Radial shower profiles

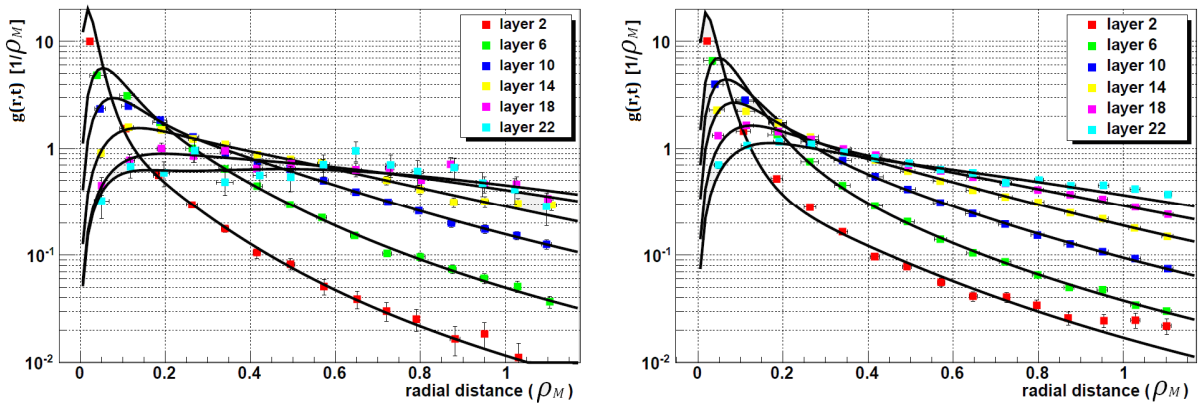

Figure 23: Panel 1 (left) Radial shower profile pdf as function of Molière radius for 5GeV electron. Panel 2 (right), Radial shower profile pdf as function of Molière radius for 50GeV electrons.

For every detection layer the radial shower profile $g(r,t)$ was determined. This was done by calculating the quantity $g(r,t)$ as defined in (3.48) for 15 concentric cylinders around the shower axis with the average taken over all events. The resulting profiles were subsequently fit by expression (3.36). In Figure 23 a selection of the probability density profiles as a function of the radial distance from the shower axis in Molière radii is

displayed. The unit of the pdf is [$1/\rho_M$] for in (3.48) the fraction of hits is divided by the longitudinal energy deposition fraction ($f(t)dt$) and by the cylinder width in Molière radii. This is done in order to allow comparison with the parametrization results in [2]. The precise horizontal position of the data points is given by the average of the distribution of radii at which the hits in the considered cylinder occurred. The horizontal errors correspond to the standard deviation of said distribution. The uncertainty of the calculated $g(r,t)$ is given by the standard error of the mean

$$\sigma_{\bar{r}} = \frac{\sigma_r}{\sqrt{N_{evt}}} \tag{3.49}$$

with σ_r the standard deviation of the measured f-values and N_{evt} the number of events.

In Figure 23 the core component of the shower is clearly visible for the profile of layer 2 at both energies. For deeper layers the tail component becomes increasingly well pronounced and the contribution of the core component disappears. Layer 6 is positioned before the shower maximum of the 50GeV showers and after the 5GeV shower maximum. This explains the discrepancy in the core component strength between these two profiles.

Note that since the effective radiation length is very close to the thickness of a single layer, the layer numbers roughly equal the depth in radiation lengths. This allows for a comparison with the 10GeV radial shower profiles in Figure 9 and the 40GeV radial shower profile on the left in Figure 12 of article [2]. This comparison shows a good agreement that functions as a consistency check for the conducted simulations.

The radial profiles for 5GeV electrons in panel 1 of Figure 23 with the profiles for 50GeV electrons in panel 2 turn out to be remarkably similar. Considering the weak energy dependence of the constants in equation (3.37), (3.38) and (3.39) this agrees with expectations.

Figure 24 shows the evolution of the fitting parameters of the radial profiles with the shower depth. The 24 data points in each graph correspond to the 24 layers of which the radial profile was fit by (3.36). The shower depth is expressed in units of the shower maximum for convenience as explained previously. Note that since the shower maximum for the 50GeV showers extends deeper into the detector the detector is only about $3T$ deep in this scenario, while the detector is about $4.5T$ deep for the 5GeV showers. The errors were extracted from the fitting algorithm and the green lines correspond to the predictions as calculated in (3.40), (3.41) and (3.42). The peculiar behaviour of the R_C and R_T parameter is explained in [9] as mentioned before. The decrease of p with the shower depth indicates the diminishing contribution of the core component with increasing depth as expected.

It is clear that though the data qualitatively shows the same features as the parametrizations the quantitative agreement with the predictions is very poor. Concluding the two component Ansatz proposed in [2] is very well suited to fit the radial profile data. However the parametrization of its parameters is not very convincing for the FoCal data.

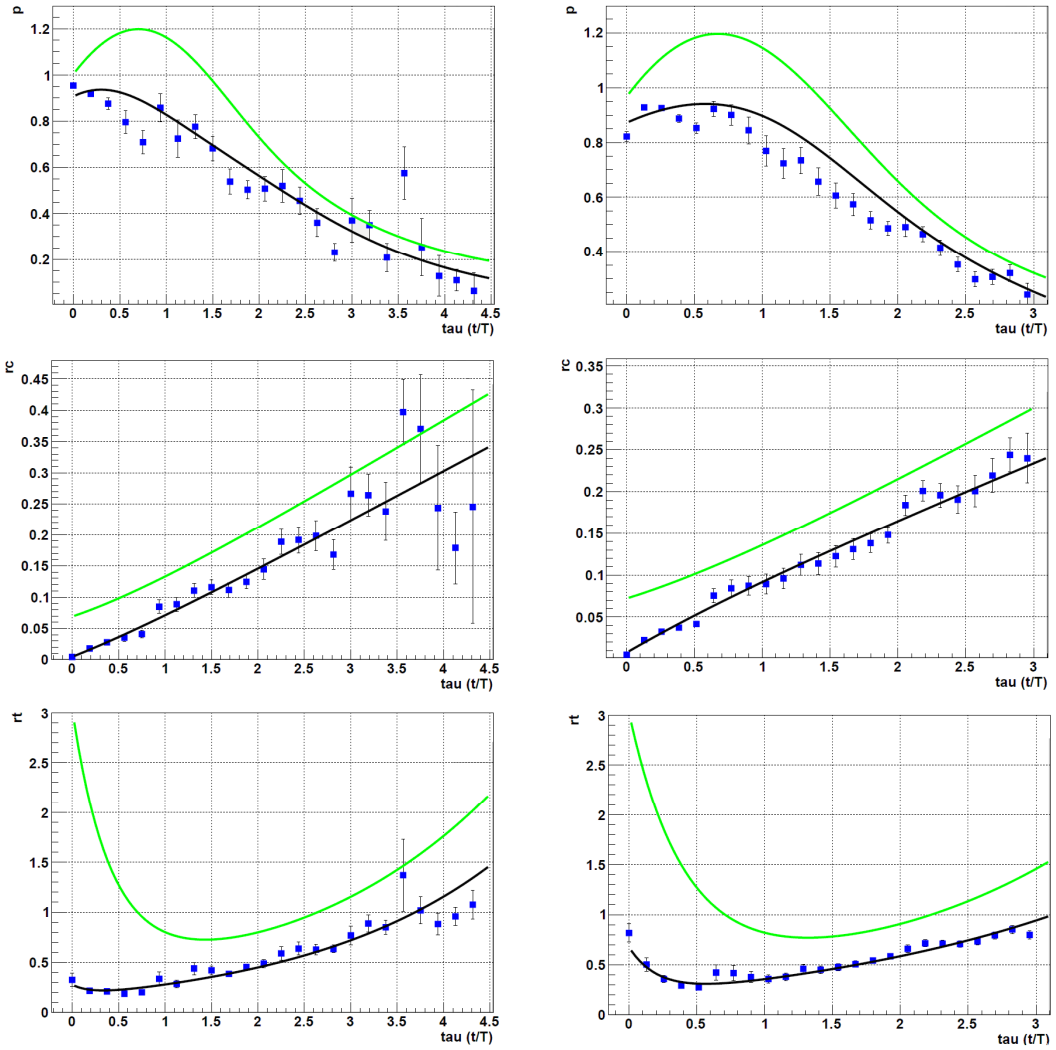

Figure 24: Panel 1 (up left), *p*-fit for 5GeV showers. Panel 2 (up right), *p*-fit for 50GeV showers. Panel 3 (middle left), R_c-fit for 5GeV showers. Panel 4 (middle right), R_c -fit for 50GeV showers. Panel 5 (down left), R_t-fit for 5GeV showers. Panel 6 (down right), R_t -fit for 50GeV showers. Parametrization predictions from (3.40), (3.41) and (3.42)represented by green lines.

The discrepancy between the predicted parametrizations and the found parametrizations seems quite dramatic. In order to investigate this difference in more detail the predicted constants and the fit constants were extracted from the 50GeV simulations in Figure 24 for $\tau = 0.5$ and $\tau = 2$ and used to explicitly compare the radial profiles they parameterize. In Figure 25 the results of this exercise are shown. For $\tau = 2$ the radial profiles are remarkably similar even though the parameters for both profiles differ significantly. For $\tau = 0.5$ the differences between the 2 parameterizations are more pronounced. The significantly lower R_c and R_t parameters found through the fit cause the distribution to be significantly narrower and closer to 0. This leads to the conclusion that after the shower maximum ($\tau > 1$) the distributions from [2] and those presented in this thesis really match very well, while

in front of the shower maximum the showers generated here are slightly narrower then the ones presented in [2].

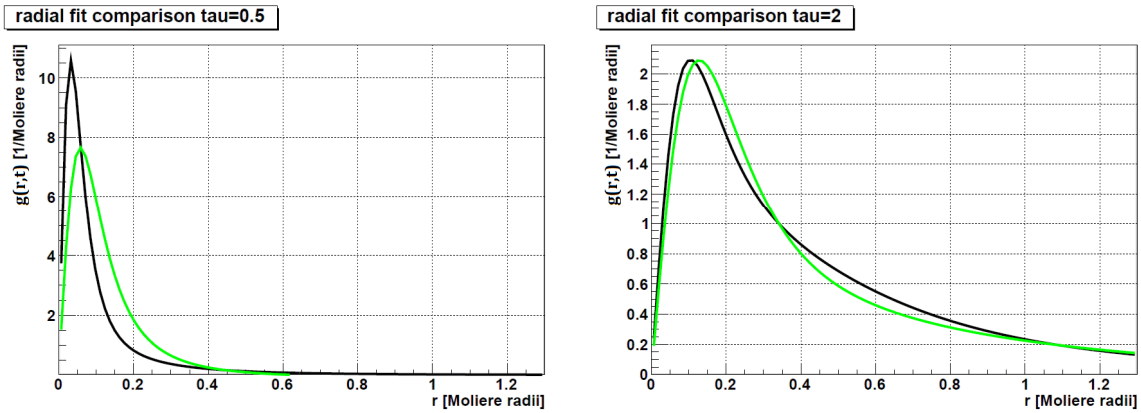

Figure 25: Panel 1 (left), Comparison of calculated radial profile with fit radial profile for τ = 0.5. Panel 2 (right), Comparison of calculated radial profile with fit radial profile for τ = 2.

3.4 Total Response

In Figure 26 the total response of FoCal as a function of energy is shown. The total response here is defined as the total number of hit pixels. The results presented in Figure 26 were extracted from the same 7 simulations as the shower shape data presented above. Note that in these simulations no discriminators were applied. The specifics of the implemented running scenario can be found in the introduction of the shower shape section. At each simulated energy the average number of hit pixels was determined. The uncertainty in this measurement is given by

$$\sigma_{\bar{r}} = \frac{\sigma_r}{\sqrt{N_{evt}}} \tag{3.50}$$

With σ_r the standard deviation of the total response distribution and N_{evt} the number of events. There are no horizontal errors since the primary energy is controlled precisely. The response turns out to be linearly dependent on the primary energy up to very high energies and is therefore a very good measure for the total primary energy, while regular sampling calorimeters suffer from saturation and recombination effects that cause the total response to deviate from its linear path [1]. This is probably a consequence of the high granularity of the FoCal prototype. Saturation effects will start to influence the digital measurements as the

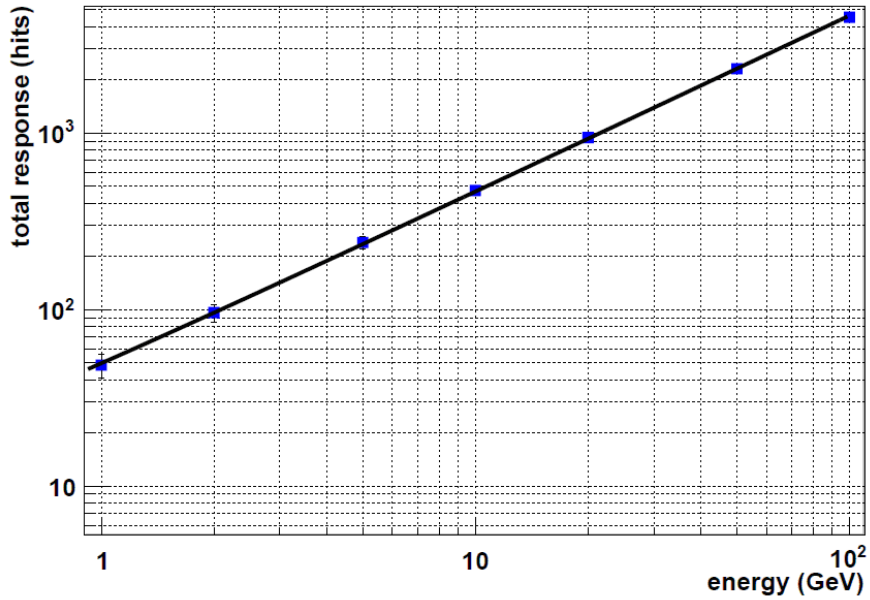

Figure 26: Total response of detector as function of primary electron energy

shower particle density increases to levels where several shower particles hit a single pixel or the charge leaking from adjacent hit pixels cause secondary non-hit pixels to generate a signal. However since the granularity of the MIMOSA chips is very high these processes are very unlikely to occur at the relevant energies. Considering the energy deposition results presented above the total number of electrons and positrons hitting any chip at one time for a 5GeV primary electron is on the order of 10^2. Given that each MIMOSA chip has 640x640 pixels it becomes evident that FoCal is impervious to the previously mentioned saturation effects up to very high energies. This is finally also confirmed by the fact that the average number of energy depositions for the 5GeV showers as discussed in the previous section matches the number of pixel hits. Thus no multiple hits occur on a single pixel, which leads to the conclusion that saturation effects do not play a role in the considered energy regime.

It is important to note here that as the primary energy increases and the showers grow in size the lateral shower leakage increases rather strongly in the relatively narrow prototype tower. However given that independent of the energy approximately 90% of the energy is deposited within 1 Molière radius of the shower axis, the lateral shower leakage should be roughly proportional to the energy. Therefore in the eventual wider FoCal design where there is no significant lateral shower leakage the total response curve is probably steeper though still linear. Finally it is worthwhile to notice that the fit passes through the origin as expected.

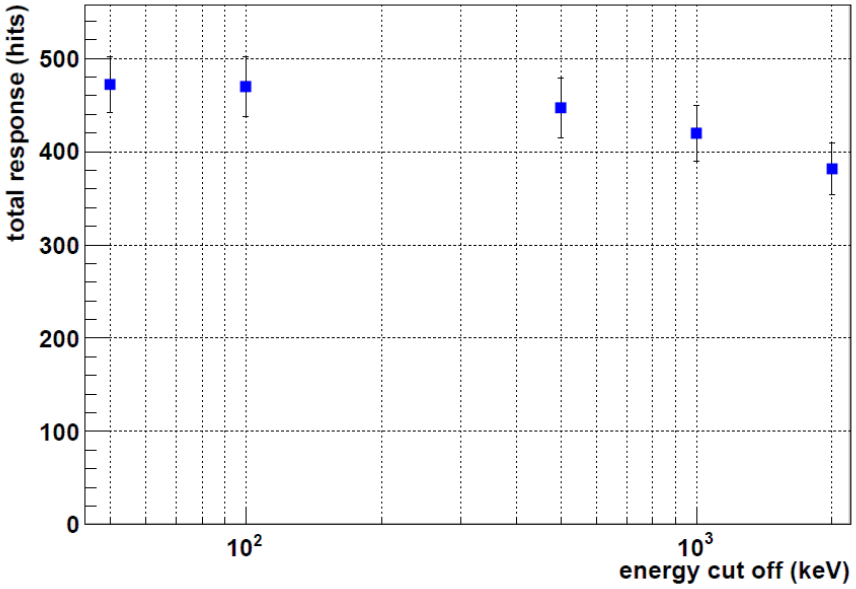

Figure 27: Total response of the detector as a function of photon and electron cut off value

In Figure 27 the total response of the detector is displayed for several 1000 event simulations of 10GeV showers caused by electrons. The total response is plotted as function of the energy cut off of the electrons, positrons and photons. There are no horizontal errors for the energy can be set with arbitrarily large precision. The vertical errors represent the standard deviation of the total hits distribution. As can be seen the response is constant for cut off values below 100keV indicating that the low energy (<100keV) electrons and positron barely interact with the chips or produce particles that do. Apparently the range of the very low energy particles is so small in the tungsten absorber that they despite their inevitable large number do not reach the chips. This is also evident from Panel 5 and 6 of Figure 17 where can be seen that only a very small fraction of the energy depositions in the chips is deposited by particles with an energy below 100keV. If the cut off is chosen larger then 100keV a gradual decrease of the response occurs. This is caused by a reduced particle flux due to the earlier termination of particles that would have otherwise traversed the chips and by the reduced particle production due to this higher cut off value. This plot indicates the importance of using a properly small energy cut off since the default value of 1MeV for both photons and electrons does not allow a realistic simulation.

3.5 Energy Resolution

Finally for the sake of completeness the energy resolution results are displayed in Figure 28. These results were derived from the same 7 simulations that were used for the shower shape analysis and the determination of the total response as a function of the energy. The

exact details on the running scenario can be found in the introduction of section 3.3.3. Important again is to note that no discriminator was applied in these simulations. The energy resolution is generally defined as

$$R(E) = \frac{\sigma(E)}{E} \tag{3.51}$$

with *R(E)* the energy resolution and *σ(E)* the standard deviation of the energy measurements at primary electron energy *E.* As was shown in Figure 26 the measured energy is proportional to the total number of hits (*H*). Therefore the resolution can be expressed in the total number of hits per event (*H*) in the following way

$$\frac{\sigma(E)}{E} = \frac{\sigma(cH)}{\langle cH \rangle} = \frac{|c|\sigma(H)}{c\langle H \rangle} = \frac{\sigma(H)}{\langle H \rangle} \tag{3.52}$$

were the average is taken over all 1000 simulated events and *c* is the proportionality constant that relates *H* and *E*. This quantity is shown below in Figure 28 for several energies. The data points are fit with the general expression for the energy resolution [10]

$$R(E) = \frac{a}{\sqrt{E}} \oplus \frac{b}{E} \oplus c \tag{3.53}$$

were ⊕ denotes the quadratic sum and the following constants were found a = 0.026, b = 0.00016 and c = 0.041. The first term dominates the energy resolution and is related to inherent sampling fluctuations. The second term takes into account instrumental effects like noise, however since no noise was implemented in the simulations this term is almost negligible and the last term is caused by geometrical imperfections like dead detection areas. The last term sets the resolution limit for very high energies. As can be seen the resolution levels out at approximately 5% for very high energies.

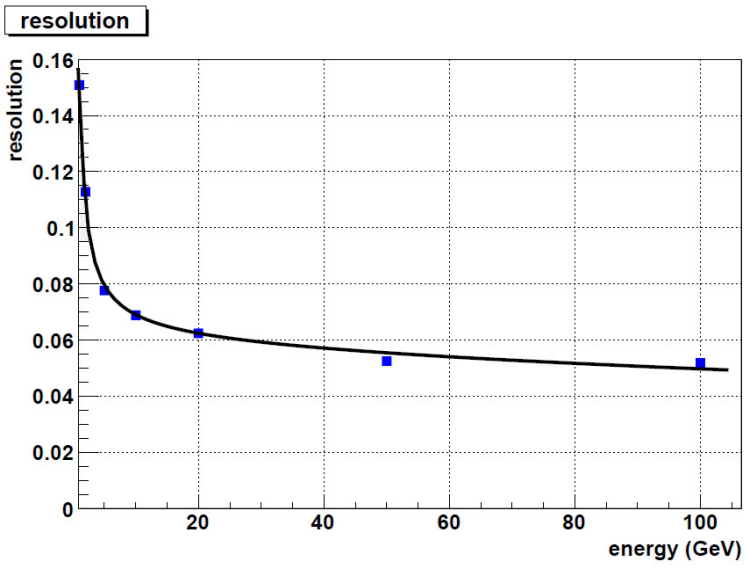

Figure 28: FoCal resolution at various energies according to simulations without a discriminator threshold

4. Conclusion

In the first results section on the sampling fraction and the energy distribution over the volumes it became clear that the amount of energy deposited is within 10% of the expected amount based on the [2] estimate. In the subsequent section on the energy deposition in thin layers it was concluded that the energy deposition processes for the 30micron thick epitaxial layer of the MIMOSA chips are accurate down to the 20% level for the low energy particles (<5MeV) that deposit the overwhelming majority of the total energy in the chips. Finally in the last results section on the total response it turned out that saturation effects do not play any role at the energies up to 100GeV. Now the conclusion can be drawn given that the total energy deposition in the chips is about 10% too high and the amount of energy deposited per hit is approximately 20% too high that the total response of the simulated detector should roughly be accurate down to the 10% level. In addition in the results section on the shower shape it was shown that the spatial distribution of these hits also very nearly matches the parametrizations presented in [2]. Thus the simulation framework developed in this thesis yields an accurate tool for the FoCal R&D process.

5. Further research

Several upgrades and adaptations that came up in the last two months are the following.

- A thorough investigation into the influence of the step size parameters on the simulation results should be conducted. In this thesis the recommendation of the GEANT manual was followed not to alter the standard step size settings in the tracking parameters unless their function was well understood.
- The geometry interface allows for an easy geometry manipulation by the user. This offers the opportunity to investigate a large variety of geometries without much difficulty for new users.
- The implementation of multipixels is an ongoing subject of discussion in the FoCal design process. This method implies the automatic summation of the hits of clusters of pixels effectively reducing the data stream. This aspect is not yet an integral part of the simulation process, however it can be fairly easily investigated using user scripts.
- A more thorough energy cut off investigation researching the individual roles of the photon and electron/positron cut off values should be useful, since higher cut offs imply reduced simulation times.
- Charge diffusion over multiple pixels might strongly affect the total response of the detector. A comparison with the total response of the prototype is therefore of paramount importance to determine whether this effect should be taken into account in the simulations.
- The implementation of noise is still quite rudimentary. As more data is gathered by the actual FoCal prototype the noise generation method as described in this thesis probably needs adequate updates.
- Once enough data is gathered by the FoCal prototype a comparison of the shower shapes as presented in this thesis with said data would serve as another consistency check of the simulation framework.
- Finally the implementation of layers of analogue silicon pads seems very likely at this stage in the FoCal R&D process. Therefore an easy way of simulating these should be included in the simulation framework to allow for more comprehensive simulation capabilities.

6. Bibliography

[1] R. Wigmans. *Calorimetry, Energy Measurement in Pariticle Physics*. New York, Oxford University Press. (2000)

[2] G. Grindhammer, S. Peters. *The Parameterized Simulation of Electromagnetic Showers in Homogeneous and Sampling Calorimeters.* arXiv:hep-ex/0001020v1, 1-42, München (2000)

[3] M. Berger, S. Seltzer. *Tables of energy losses and ranges of electrons and positrons.* NAS-NRC 1133, 3-18, (1964)

[4] R. Brun et al. *GEANT Detector Description and Simulation Tool.* wwwasd.web.cern.ch/wwwasd/geant/, 256-274, Geneva (1993)

[5] R. Sternheimer, M. Berger, S. Seltzer. *Density effect for the ionization loss of charged particles in various substances.* Atomic Data and Nuclear Data Tables, Vol.30 No.2, (1984)

[6] C. Leroy, P. Rancoita. *Principles of radiation interaction in matter and detection.* World Scientific Publishing Co. Pte. Ltd. Singapore (2004)

[7] K.Lassila-Perini, L.Urbán Nucl.Inst.Meth. A362 416 (1995)

[8] J. Apostolakis, S. Giani, L. Urbán, M.Maire, A. Bagulya, V. Grichine. *An implementation of ionisation energy loss in very thin absorbers for the GEANT4 simulation package*. Nucl. Instr. & Meth. , A453 597-605, (2000)

[9] S. Peters, PhD thesis, University of Hamburg; MPI-PhE/92-13 (1992)

[10] C.Fabjan, F. Gianotti. *Calorimetry for Particle Physics.* CERN-EP/2003-075 (2003)

7. Appendix

7.1 Noise implementation

The most precise method to add noise pixels to the frames would be the following method. First the noise energy deposition distribution per unit time for each individual pixel is determined. Secondly at each readout time every pixel is assigned a noise energy deposition according to its individual distribution. Finally the total energy deposition in a pixel is compared to the discriminator setting of the column it belongs to. This method however would demand far too much computing time. For this reason the implementation of noise pixels is approached in the following way. When adding the noise energy depositions to the assumption is made that the size of the energy deposition through noise mechanisms per time between readouts of a pixel is distributed according to a poissonian. Also this distribution is assumed to be the same for all pixels in each column, since the average of the poissonian is set per column. Now given this distribution and the discriminator setting of a column the probability of a non-hit pixel becoming a noise pixel can be calculated. This probability is equal for all the pixels in this column. Next the number of pixels in the column is chosen according to a binomial distribution Bin(n,p) with n the number of pixels in the column and p the previously calculated probability for that column. However since n is large (>100) the following approximation is used
Bin(n,p)≈Norm(np+0.5,sqrt(np(1-p)))

$$\mathrm{Bin}(n, p) \approx \mathrm{Norm}(np + \frac{1}{2}, \sqrt{np(1-p)}) \tag{6.1}$$

Next the row numbers of this number of noise pixels is chosen according to a uniform distribution since all configurations of noise pixels in the column are equally likely to occur. Finally the frame pixels are added to the FocalFrame object with a large energy deposition to make sure they exceed the discriminator setting. In addition an energy deposition is added to all the frame pixel objects that were already present in the FocalFrame object. These frame pixels correspond to the actual hits by traversing particles. The added energy deposition to these pixels is also chosen according to the poissonian mentioned before. This final step is important because the pixels that already contain a small energy deposition might be pushed over the discriminator threshold by only a small noise energy deposition. There is a fundamental problem with this method however. The energy deposition of pre existing frame pixels thus the ones that were actually hit by particles have two chances of exceeding the discriminator threshold. First they can be picked as noise pixel and secondly the extra added noise energy deposition can push them over the threshold. The solution to this problem would be to exclude these pixels from the determination of the number of noise pixels in a column. And, to exclude them from the selection of the noise pixel. However the implementation of these considerations would introduce additional computing time, since these calculations have to be executed in high quantities.

7.2 Geometry interface manual

DEFINE MEDIUM----------

#MEDIUM name density -1
element abbreviation element weight fraction
element abbreviation element weight fraction
element abbreviation element weight fraction
ETC. ETC.

EXPLANATION:

GENERAL
First of all it's essential all individual media have a unique name. This name should be a string of characters without any spaces. All characters including all punctuation marks may occur in this string. The order of subcommands like density, isvol, CUTGAM does not matter. Don't use any commas or other punctuation marks, all commands should be seperated by spaces, tabs or put on different lines. Commands can also be put on the same line as long as they're seperated by at least a space. (The command is read in as a single string and subsequently tokenized using space, \n (end of line) and \t (tab) as delimiters. Finally the position of the seperated strings determine whether a subcommand or a numerical value is expected). The program will give error messages if the described layout conditions aren't met.

DENSITY
default value is -1, so if not defined otherwise program will generate error message density should be spelled without capitals. The unit of the density is gr/cm^3.

TRACKING PARAMETERS
The parameters isvol, ifield, fieldm, tmaxfd, stemax, deemax, epsil and stmin are the so called tracking parameters. These parameters should be spelled without capitals. These parameters should be defined for each medium since the default values are set for quick test runs, so NOT for detailed simulations. In GEANT3 these parameters are normally automatically calculated, when using the geometry-interface however the calculated values will be overwritten by the default values further stressing the importance of making a well considered choice for the size of these parameters
for all individual volumes. Also by controlling these parameters ourselves the results of simulations will be more consistent, ruling out any descrepancies due to differing calculations of the tracking parameters by GEANT3 itself. Underneath the tracking parameters and their default values are defined. More detailed information on the tracking parameters and their implementation by GEANT3 can be found in the GEANT3 manual at

http://wwwasdoc.web.cern.ch/wwwasdoc/geant/geantall.html in the CONS200 chapter on tracking medium parameters.

isvol (integer) sensitivity flag:
default 0
= 0 not a sensitive volume
>0 sensitive volume

ifield (integer) magnetic field flag:
default 0
=0 no magnetic field
=1 strongly inhomogeneous magnetic field: tracking performed with the Runge-Kutta method
by the routine GRKUTA;
=2 inhomogeneous magnetic field tracking along a helix performed by the routine GHELIX;
=3 uniform magnetic field along the z axis of strength FIELDM, tracking performed along a helix by the routine GHELX3;

fieldm (float) maximum field value (in Kilogauss):
default 0

tmaxfd(float) maximum angular deviation due to the magnetic field permitted in one step (in degrees):
default 0.1

stemax (float) maximum step permitted (cm):
default 0.1

deemax (float) maximum fractional energy loss in one step (0<DEEMAX=1):
default 0.1

epsil (float) boundary crossing precision (cm):
default 0.1

stmin (float) minimum value for the maximum step imposed by energy loss, multiple scattering,
Cerenkov or magnetic field effects (cm):
default 0.1

SPECIAL TRACKING PARAMETERS

The parameters CUTGAM, CUTELE, CUTNEU, CUTHAD, CUTMUO, BCUTE, BCUTM, DCUTE, DCUTM, PPCUTM, PAIR, COMP, PHOT, PFIS, DRAY, ANNI, BREM, HADR, MUNU, DCAY, LOSS, MULS, SYNC, and STRA are the so called special tracking parameters. These parameters should be spelled with capitals. These parameters don't have to be defined for each medium since the default values are set for a realistic simulation, however do make sure that for your simulation important processes aren't by default ignored. The default values as given below are also the values that are used by GEANT3 if not defined otherwise by the user. Underneath the special tracking parameters and their default values are defined. More detailed information on the tracking parameters and their implementation by GEANT3 can be found in the GEANT3 manual at

http://wwwasdoc.web.cern.ch/wwwasdoc/geant/geantall.html in the CONS210 chapter on special tracking parameters.

CUTGAM (float) threshold for gamma transport (in GeV):
default 0.001
CUTELE (float) threshold for electron and positron transport (in GeV):
default 0.001
CUTNEU (float) threshold for neutral hadron transport (in GeV):
default0.01
CUTHAD (float) threshold for charged hadron and ion transport (in GeV):
default0.01
CUTMUO (float) threshold for muon transport (in GeV):
default0.01
BCUTE (float) threshold for photons produced by electron bremsstrahlung (in GeV):
default 0.001
BCUTM (float) threshold for photons produced by muon bremsstrahlung (in GeV):
default 0.001
DCUTE (float) threshold for electrons produced by electron delta -rays (in GeV):
default 10000
DCUTM (float) threshold for electrons produced by muon or hadron delta -rays (in GeV):
default 10000
PPCUTM (float) threshold for direct pair production by muon (in GeV):
default 0.01
DCAY (integer) Decay in flight. The decaying particles stops:
default 1
=0 No decay in flight.
=1 Decay in flight with generation of secondaries.
=2 Decay in flight without generation of secondaries.
MULS (integer) Multiple scattering:
default 1
=0 No multiple scattering.
=1 Multiple scattering according to Molière theory.
=2 Same as 1. Kept for backward compatibility.
=3 Pure Gaussian scattering according to the Rossi formula.
PFIS (integer) Nuclear fission induced by a photon. The photon stops:
default 0
=0 No photo-fission.
=1 Photo-fission with generation of secondaries.
=2 Photo-fission without generation of secondaries.
MUNU (integer) Muon-nucleus interactions. The muon is not stopped:
default 1
=0 No muon-nucleus interactions.

=1 Muon-nucleus interactions with generation of secondaries.
=2 Muon-nucleus interactions without generation of secondaries.

LOSS (integer) Continuous energy loss:
default 2
=0 No continuous energy loss,IDRAY is forced to 0.
=1 Continuous energy loss with generation of d-rays above DCUTE and restricted Landau fluctuations below DCUTE.
=2 Continuous energy loss without generation of d-rays and full Landau-Vavilov-Gauss fluctuations. In this case the variable DRAY is forced to 0 to avoid double counting of fluctuations.
=3 Same as 1, kept for backward compatibility.
=4 Energy loss without fluctuation. The value obtained from the tables is used directly.

PHOT (integer) Photoelectric effect. The interacting photon is stopped:
default 1
=0 No photo-electric effect.
=1 Photo-electric effect with generation of the electron.
=2 Photo-electric effect without generation of the electron.

COMP (integer) Compton scattering:
default 1
=0 No Compton scattering.
=1 Compton scattering with generation of .
=2 Compton scattering without generation of .

PAIR (integer) Pair production. The interacting gamma is stopped:
default 1
=0 No pair production.
=1 Pair production with generation of /.
=2 Pair production without generation of /.

BREM (integer) bremsstrahlung. The interacting particle (, , mu+ , mu-) is not stopped. The variable IBREM controls this process.
default 1
=0 no bremsstrahlung.
=1 bremsstrahlung with generation of gamma.
=2 bremsstrahlung without generation of gamma.

DRAY (integer) d-ray production:
default 1
=0 No d-rays production.
=1 d-rays production with generation of .
=2 d-rays production without generation of .

ANNI (integer) Positron annihilation. The is stopped:
default 1

=0 No positron annihilation.
=1 Positron annihilation with generation of photons.
=2 Positron annihilation without generation of photons.

HADR (integer) Hadronic interactions. The particle is stopped in case of inelastic interaction,
while it is not stopped in case of elastic interaction:
default 1
=0 No hadronic interactions.
=1 Hadronic interactions with generation of secondaries.
=2 Hadronic interactions without generation of secondaries.
>2 Can be used in the user code GUPHAD and GUHADR to chose a hadronic package. These values
have no effect on the hadronic packages themselves.

STRA (integer) This flag turns on the collision sampling method to simulate energy loss in thin
materials, particularly gases:
default 0
=0 Collision sampling switched off.
=1 Collision sampling activated.

SYNC (integer) Synchrotron radiation in magnetic field:
default 0
=0 The synchrotron radiation is not simulated.
=1 Synchrotron photons are generated, at the end of the tracking step.
=2 Photons are not generated, the energy is deposit locally.
=3 Synchrotron photons are generated, distributed along the curved path of the particle.

NOT YET IMPLEMENTED:

LABS Light ABSorption. This process is the absorption of light photons (particle type 7) in dielectric
materials. It is turned on by default when the generation of Cerenkov light is requested (data
record CKOV). For more information see [PHYS260].
=0 No absorption of photons.
=1 Absorption of photons with possible detection.

GHCOR1 see [PHYS700] not yet implemented
BIRK1 see [PHYS337] not yet implemented
BIRK2 see [PHYS337] not yet implemented
BIRK3 see [PHYS337] not yet implemented

ELEMENT

Elements are specified by their standard abbreviation from the periodic table in capitals only. With the only addition of VACUUM which is also a valid ELEMENT. The numerical

argument following the abbreviation is the weight fraction of the element in the medium. Make sure that the different fractions add up to exactly 1, otherwise an error messages will be generated and the medium will not be defined properly.

EXAMPLE
Define the medium air with adjusted CUTGAM and CUTELE in the following way:

```
#MEDIUM     air  density 0.0012
            O      0.2
            N      0.8
```

DEFINE MARS----------

#MARS halflength halfwidth halfheigth Xorigin Yorigin Zorigin
EXPLANATION:

GENERAL
The command MARS defines the mother reference frame in which the detector will be created. The MARS consists of a box with certain heigth in z-direction, width in y direction and length in x direction. The origin parameters specify the position of the origin inside the box. For 0 0 0 the origin will in the middle of all 3 dimensions of
the box. The X-, Y- and Zorigin floating numbers now specify a translation of the MARS box in relation to this central origin position, which will cause the origin to shift in exactly opposite direction (see example below). It is necessary to define MARS before you try to POSITION any volumes, since the command POSITION will position
the volume in MARS. Also make sure the MARS box is sufficiently large to prevent the detector from extruding this frame, since this will generate an overlap error which in turn will lead to unpredictable tracking results. All the numerical parameters in this command should be floating point numbers and the unit of these numbers is cm.
EXAMPLE:
A mother reference frame box with a total width, heigth and length of 100 with the origin in the bottom-front-left corner is defined in the following way

#MARS 50 50 50 50 50 50

DEFINE VOLUME----------

#VOLUME name BOX fDx fDy fDz fOrigin[0] fOrigin[1] fOrigin[2] "NAME MEDIUM"
#VOLUME name PARALLELEPIPED fDx fDy fDz fAlpha fTheta fPhi "NAME MEDIUM"
#VOLUME name TRAPEZOID1 fDx1 fDx2 fDy fDz "NAME MEDIUM"
#VOLUME name TRAPEZOID2 fDx1 fDx2 Fdy1 fDy2 fDz "NAME MEDIUM"
#VOLUME name GENERALTRAPEZOID fDz fTheta fPhi fH1 fBl1 fTl1 fAlpha1 fH2 fBl2 fTl2 fAlpha2 "NAME MEDIUM"

#VOLUME name TWISTEDTRAPEZOID fDz fTheta fPhi fTwist fH1 fBl1 fTl1 fAlpha1 fH2 fBl2 fTl2 fAlpha2 "NAME MEDIUM"
#VOLUME name TUBE1 fRmin fRmax fDz "NAME MEDIUM"
#VOLUME name TUBE2 fRmin fRmax fDz fPhi1 fPhi2 "NAME MEDIUM"
#VOLUME name TUBE3 fRmin fRmax fDz fPhi1 fPi2 Nlow Nhigh "NAME MEDIUM"
#VOLUME name TUBE4 fA fB fDz "NAME MEDIUM"
#VOLUME name HYPERBOLOID fRmin fStin fRmax fStout "NAME MEDIUM"
#VOLUME name CONE1 fDz fRmin1 fRmax1 fRmin2 fRmax2 "NAME MEDIUM"
#VOLUME name CONE2 fDz fRmin1 fRmax1 fRmin2 fRmax2 fPhi1 fPhi2 "NAME MEDIUM"
#VOLUME name SPHERE fRmin fRmax fTheta1 fTheta2 fPhi1 fPhi2 "NAME MEDIUM"
#VOLUME name TORUS fR fRmin fRmax fPhi1 fDphi "NAME MEDIUM"
#VOLUME name PARABOLOID fRlo fRhi fDz "NAME MEDIUM"
#VOLUME name POLYGON1 fPhi1 fDphi fNz fZ[0] fZ[1] fZ[2] fZ[3] ... "NAME MEDIUM"
#VOLUME name POLYGON2 fPhi1 fDphi fNedes fNedges fZ[0] fZ[1] fZ[2] fZ[3] fZ[4] fZ[5] fZ[6] fZ[7] ……NOT YET IMPLEMENTED
#VOLUME name COMPOSITE ..... NOT YET IMPLEMENTED

EXPLANATION:

GENERAL
The command VOLUME will create a volume of specified shape and medium. These VOLUMES can then be positioned in MARS to form the detector geometry. It's essential all individual volumes have a unique name. This name should be a string of characters without any spaces. All characters including all punctuation marks may occur in this string. Secondly the shape of the volume should be defined using only capitals in one of the following subcommands. Subsequent to the shape name below you'll find the shape class that implements the respective shapes in the ROOT framework. These classes are described in detail in the geometry package user guide at http://root.cern.ch/drupal/content/users-guide

BOX	TGeoBBox
PARALLELEPIPED	TGeoPara
TRAPEZOID1	TGeoTrd1
TRAPEZOID2	TGeoTrd2
GENERALTRAPEZOID	TGeoTrap
TWISTEDTRAPEZOID	TGeoGtra
TUBE1	TGeoTube
TUBE2	TGeoTubeSeg
TUBE3	TGeoCtub
TUBE4	TGeoEltu
HYPERBOLOID	TGeoHype

CONE1	TGeoCone
CONE2	TGeoConeSeg
SPHERE	TGeoSphere
TORUS	TGeoTorus
PARABOLOID	TGeoParaboloid
POLYGON1	TGeoPcon
POLYGON2	TGeoPgon not yet implemented
COMPOSITION	TGeoCompositeShape not yet implemented
VERTICESHAPE	TGeoArb not yet implemented

The shape name should be followed by the appropriate number of numerical arguments. These arguments can be floating numbers or integers and should be separated by spaces, (\n) enters or (\t) tabs, don't use any punctuation marks for separation. The number of parameters can be found above, the exact definition of these variables are listed in the user guide at http://root.cern.ch/drupal/content/users-guide in the geometry package chapter. Note here that the number of variables of POLYGON1, POLYGON2 and composite can vary. Below an example of these three shapes will be given. Also the order of the arguments is essential. The order should match the order as presented in the user guide, which can also be found above. In addition it is essential the right number of arguments is handed to the program otherwise an error message will be
generated and since the program doesn't implement any default values for the volumes, they will not be generated correctly. Finally the medium of the volume has to be defined. This medium should be declared before it is needed in the creation of a volume. Also it's important the names match exactly. When placing a certain volume inside another volume with the command POSITIONIN the inner volume will have its own medium and the complement of the smaller volume in the larger volume will be filled with the larger volume medium.

EXAMPLE POLYGON1:

```
#VOLUME     polygon1test_1        POLYGON1    330 610 5      (*polygon with 6 sections,
see user guide*)
                                        0  10 15 20
                                        1  30 15 30
                                2  30 15 30
                                        3  50 15 16
                                        4  50 15 20
                                        5  80 15 40
                                        air
```

EXAMPLE POLYGON2:

```
#VOLUME polygon2test_1 POLYGON2
```

EXAMPLE COMPOSITION:

```
#VOLUME compositiontest_1 COMPOSITION
```

CREATE COMPOSITE VOLUME----------

#COMPOSITE name NAME OBJECT/COMPOSITE1 X Y Z PHI THETA PSI copynr
NAME OBJECT/COMPOSITE2 X Y Z PHI THETA PSI copynr
NAME OBJECT/COMPOSITE3 X Y Z PHI THETA PSI copynr (*see tgeorotation for specification angles*)

EXPLANATION:

GENERAL
The command COMPOSITE is used to 'glue' together multiple volumes (not necessarily with equal media) to form a larger volume with it's own name that can then be placed in the MARS box to form part of the detector or be used in another larger composite volume. It is ideal for constructing layers or units of a calorimeter that can then be placed multiple times in MARS. Say we want to make a composite of two boxes one bigger then the other. First we define the volumes box1 and box2 with the VOLUME command. Next we add box1 to the composite by specifying x, y, z, phi, theta and psi. These parameters give the translation and rotation that generate the transformation of the reference frame of the volume in relation to the motherframe of the composite. The x, y and z parameters correspond to normal translation of the volume frame in the composite motherframe. The phi, theta and psi parameters correspond to rotations of the volume frame in relation to the composite motherframe. First a rotation about Z axis with angle phi, then a rotation with theta about the rotated X axis, and finally a rotation with psi about the new Z axis. Note that the rotations are executed before the translations. Subsequently repeat the procedure for box2, position the composite of box1 and box2 in MARS using POSITION. By running the program the composite can be checked for any relative positioning errors or overlaps. Finally when a certain volume is used multiple times in one composite volume it's important to indicate the different instances of the volume with a different copynumber. This is important since the function MISALIGN has to be able to uniquely identify a certain volume by its name and copynumber. The composite function operates in the following way: First using
the shapes and transformations of the involved volumes a composite shape is created. This shape is then turned into a empty virtual volume. Finally the empty virtual volume is filled with the respective volumes again using their transformations. So summarizing a virtual composite volume is created that exactly accommodates the involved volumes.
When a volume needs to misaligned eventually do make sure that it is positioned inside another possibly virtual and most importantly larger volume (using POSITIONIN), since misaligning the smaller volume will shift it possibly causing overlaps that will in turn generate error messages and unpredictable tracking results. For this reason it is also not a good idea to put a volume that needs to be misaligned in a composite volume. This because the composite volume will consist of a composite shape virtual volume that exactly contains the other volumes. So if in this scenario one of the volumes is misaligned it will extrude its virtual container. Therefore whenever you have a volume A that needs to be both

misaligned and part of a composite volume operate in the following manner. First create a virtual container that is large enough to contain volume A also when it is misaligned and subsequently add the virtual container volume to the composite volume. The virtual container can be considered as the room volume A has for misalignment, make sure any misalignments don't cause volume A to extrude its container.

EXAMPLE

```
#COMPOSITE compositetest_1      box1 0  0 0 0 0 0 0
                                box1 1  0 0 0 0 0 1
                                box1 0  1 0 0 0 0 2
                                box2 -4 0 0 0 0 0 0
                                box2 -2 0 0 0 0 0 1
```

POSITION VOLUMES IN MARS----------

#POSITION "NAME OBJECT/COMPOSITE" X Y Z PHI THETA PSI copynr

EXPLANATION:

GENERAL
The command POSITION can be used when a volume and MARS are defined properly. The x, y and z correspond to the translation of the reference frame of the volume in relation to the MARS reference frame. The phi, theta and psi are again the rotations
of the volume frame in relation to the MARS frame. First a rotation about Z axis with angle phi, then a rotation with theta about the rotated X axis, and finally a rotation with psi about the new Z axis. Note that the rotations are executed before the translations. Finally when a certain volume is positioned multiple times in MARS it's important to indicate the different instances of the volume with a different copynumber. This is important since the function MISALIGN has to be able to uniquely identify a certain volume by its name and copynumber.

EXAMPLES

```
#POSITION compositetest_1  1  2 3 10 20 30 0
#POSITION box1                  0  0 0 0  0  0  0
#POSITION box1          10 9 8 10 10 10 1
```

POSITIONIN----------

#POSITIONIN "name mothervolume" "name daughter volume" X Y Z PHI THETA PSI copynr

EXPLANATION:

GENERAL
The command POSITIONIN is used to position a volume inside another volume. The larger

volume can be virtual meaning its medium is VACUUM and it merely serves as a container for other volumes for positioning or misalignment purposes. However the larger volume can also have a real medium in which case only the complement of the smaller volume will still contain the medium of the larger volume. The x, y and z correspond to the translation of the reference frame of the smaller volume in relation to the reference frame of the larger volume. The phi, theta and psi are again the rotations of the smaller volume frame in relation to the larger volume frame. First a rotation about Z axis with angle phi, then a rotation with theta about the rotated X axis, and finally a rotation with psi about the new Z axis. Note that the rotations are executed before
the translations. Finally when a certain volume is positioned multiple times in another volume it's important to indicate the different instances of the smaller volume with a different copynumber. This is important since the function MISALIGN has to be
able to uniquely identify a certain volume by its name and copynumber. When a volume needs to misaligned eventually do make sure that it is positioned inside another possibly virtual and most importantly larger volume, since misaligning the smaller volume
will shift it possibly causing overlaps that will in turn generate error messages and unpredictable tracking results. For this reason it is also not a good idea to put a volume that needs to be misaligned in a composite volume. This because the composite volume will consist of a composite shape virtual volume that exactly contains the other volumes. So if in this scenario one of the volumes is misaligned it will extrude its virtual container. Therefore whenever you have a volume A that needs to be both misaligned and part of a composite volume operate in the following manner. First create a virtual container that is large enough to contain volume A also when it is misaligned and subsequently add the virtual container volume to the composite volume. The virtual container can be considered as the room volume A has for misalignment, make sure any misalignments don't cause volume A to extrude its container.

EXAMPLE
#POSITIONIN box2 box1 0 0 0 0 0 0 0
#POSITIONIN box2 box1 0 0 -1 0 0 0 1
#POSITIONIN box2 box1 0 0 1 0 0 0 2

COMMENTS----------

#// this is a comment

EXPLANATION:

comments cannot be placed randomly everywhere in the geometry file. They should be put on their own command line, so they
should be preceded by #. A comment should start with "// " as shown above (the space after // is important), this way the
program will recognize the command line as a comment and not generate an error. If you

just put a comment directly after #
without the use of "// " the program will generate the error "error:: -command not recognized- line : " this has no further
implications for the generations of the geometry, but generating unnecessary error messages isn't very helpfull.

EXAMPLES
#// this is a correct way of commenting
// this is a correct way of commenting
//this is an incorrect way of commenting, because of the missing space

---

MISALIGN UNITS IN THEIR MOTHER REFERENCE FRAME----------

MISALIGN path X Y Z PHI THETA PSI

EXPLANATION:

GENERAL
Volumes can be misaligned using the command MISALIGN. When a volume needs to misaligned do make sure that it is positioned inside another possibly virtual and most importantly larger volume, since misaligning the smaller volume will shift it possibly causing overlaps that will in turn generate error messages and unpredictable tracking results. For this reason it is also not a good idea to put a volume that needs to be misaligned in a composite volume. This because the composite volume will consist of a composite shape virtual volume that exactly contains the other volumes. So if in this scenario one of the volumes is misaligned it will extrude its virtual container. Therefore whenever you have a volume A that needs to be both misaligned and part of a composite volume operate in the following manner. First create a virtual container that is large enough to contain volume A also when it is misaligned and subsequently add the virtual container volume to the composite volume. The virtual container can be considered as the room volume A has for misalignment, make sure any misalignments don't cause volume A to extrude its container. To specify the volume to be misaligned use it's path in the geometry. This is a list of composite volumes or normal volumes the volume is part of or positioned into including MARS. For example suppose we want to misalign volume A_2 that is positioned in volume B_1 which is in turn a part of composite volume C_4 we get the path: /MARS_1/C_4/B_1/A_2 . Note here that the numbers are the copynumbers as specified by the user, upon defining the respective volumes. If you are not completely sure about the names and copynumbers of the different volumes or of MARS just check TBrowser by executing "new TBrowser" on the ROOT command line. The browser will allow you to navigate through the geometry enabling you to establish the right path names. Make sure you check the MARS copynumber since this number might vary throughout different ROOT versions. It is also important to use the MISALIGN commands exclusively at the very end of the geometryfile, since the geometrymanager needs to close the geometry before the

misalignment procedure can be executed. So including a MISALIGNMENT command before the geometry has been completely defined will prevent the geometry from being defined completely. Finally the x, y and z correspond to the translation of the reference frame of the volume that needs to be misaligned in relation to the reference frame of the larger volume by which it is contained. So this is the original transformation plus any offsets. The phi, theta and psi are again the rotations of the smaller volume frame in relation to the larger volume frame. First a rotation about Z axis with angle phi, then a rotation with theta about the rotated X axis, and finally a rotation with psi about the new Z axis. Note that the rotations are executed before the translations. These rotations may also include any offsets now. Underneath you'll find a complete example of a simple geometry involving misalignments. A small box1 is positioned inside a bigger box2 that is positioned in MARS 3 times. Subsequently using the MISALIGN command the smaller boxes will all get their own misalignment with respect to their containing box.

EXAMPLE
```
#MEDIUM     air O 0.2
            N 0.8
            density 0.0012
#MARS 100 100 100 0 0 0
#VOLUME box1 BOX 1 1 1 0 0 0 air
#VOLUME box2 BOX 2 2 2 0 0 0 air
#POSITIONIN box2 box1 0 0 0 0 0 0 0
#POSITION box2 0 0 0 0 0 0 0
#POSITION box2 0 1.2 0 0 0 0 1
#POSITION box2 0 10 0 0 0 0 2
#MISALIGN /MARS_1/box2_0/box1_0 0 0 0 10 0 0
#MISALIGN /MARS_1/box2_1/box1_0 0 0 0 10 10 0
#MISALIGN /MARS_1/box2_2/box1_0 0 0 0 10 10 10
```

NAMING INDIVIDUAL VOLUMES AND MARKING THEM SENSITIVE----------

#NAME path name sensitivityflag layernumber

EXPLANATION:

GENERAL
Individual volumes can be set as sensitive volumes, which means that any energy depositions in these volumes are considered as hits in the detector. Upon setting a volume sensitive it's possible to assign a name and layer number to the volume. The default name and layer number are "0" and "0". Make sure however that a volume can be uniquely identified using only its name and layer number. Of each hit the coordinates in the MARS frame, the volume name, layer number and energy deposition are saved. The sensitivity flag has value 0 or 1. 0 means this is not a sensitive volume and 1 means this is a

sensitive volume.

EXAMPLE
Suppose we have box1 positioned inside box2 and we want to set box1 as a sensitive volume with the name "chip_left" and layernumber 15, we'd proceed in the following manner:

#NAME /MARS_1/box2_0/box1_0 chip_left 1 15

SETTING OVERALL processes----------

RAYL Rayleigh effect. The interacting ? is not stopped. The variable IRAYL controls this process. RAYL not present in special tracking
parameters, however is present in physical processes in geant manual
=0 (D) No Rayleigh effect.
=1 Rayleigh effect.

EXPLANATION:

GENERAL
not yet implemented

7.3 Primary interface manual

#NumberOfEvents x
Always start the primary file with this command. It defines the number of events that are generated by the simulation framework. Make sure x is an integer.

#Primary
The '#NumberOfEvents' command is always followed by at least one of these commands. The Primary command defines the number of particles of a specific type having similar features that are used as the primary particles in the simulation. The primary command is always followed by a sequence of subcommands the first of which is NumberOfParticles.

NumberOfParticles
This command defines the number of primaries of that will be generated with the features that'll be defined subsequently. Next use the ParticleType command to define the primary type.

ParticleType
The ParticleType subcommand defines the primary particle type. This is done using the pdg-code of the particle. So an electron would be 11 and an anti-muon would be -13. So far we have defined the number of events, the primary particle type and the number of these specific primaries to be generated. The subcommands that follow do not have to be order in any specific way as long as they are present.

The following subcommands define the origin, momentum/energy and polarization of the primary particle(s). All the parameters have 3 options that determine their values. Namely exact, gaussian or flat. 'exact x' is used when you want to set the value of the respective parameter for all particles in the Primary command to value 'x'. 'gaussian a b' is used when you want the respective parameter to be distributed according to a Gaussian with an average 'a' and standard deviation 'b' for the particles in the Primary command. Finally 'flat a b' is used when you want the respective parameter to be distributed uniformly between the values 'a' and 'b'.

x, y, z
These subcommands define respectively the x-, y- and z-coordinate of the origin of the primaries

polx, poly, polz
These subcommands define respectively the x-, y- and z-polarization of the primaries. Make sure that the vector (polx,poly,polz) is normalized. This is also why the distribution options cannot be used in these polarization subcommands.

px, py, pz
These subcommands define respectively the x-, y- and z-momentum of the primaries in GeV/c^2. In this case the energy of the particle will be calculated using the mass from the pdg table. If you DO NOT use these 3 subcommands to directly define the momentum, make sure you use the following 3 subcommands. If you DO use these 3 commands you should NOT implement the following 3 subcommands.

e, phi, theta
If you did not use the px, py, pz subcommands, you will have to use these subcommands. 'e' defines the energy of the particle in GeV. Make sure this energy exceeds its mass. The theta and phi subcommands are used to determine the direction of the primaries. 'theta' defines the angle of the primaries with the z-axis. 'phi' defines the angle of the projection of the trajectory in the xy-plane with the x-axis.

So now we have the following scheme contains the general form of a primary file including all options:

```
#NumberOfEvents    a
#Primary       NumberOfParticles a
                                    ParticleType a
                                    x       exact a/gaussian a b/flat a b
                                    y       exact a/gaussian a b/flat a b
                                    z       exact a/gaussian a b/flat a b
                                    t       exact a/gaussian a b/flat a b
                                    e       exact a/gaussian a b/flat a b
                                    phi     exact a/gaussian a b/flat a b
                                    theta exact a/gaussian a b/flat a b
                                    polx    exact a
                                    poly    exact   a
                                    polz    exact   a
#Primary       NumberOfParticles a
                                    ParticleType a
                                    x       exact a/gaussian a b/flat a b
                                    y       exact a/gaussian a b/flat a b
                                    z       exact a/gaussian a b/flat a b
                                    t       exact a/gaussian a b/flat a b
                                    e       exact a/gaussian a b/flat a b
                                    phi     exact a/gaussian a b/flat a b
                                    theta exact a/gaussian a b/flat a b
                                    polx    exact a
                                    poly    exact   a
                                    polz    exact   a
#Primary       NumberOfParticles a
```

```
                    ParticleType a
                    x       exact a/gaussian a b/flat a b
                    y       exact a/gaussian a b/flat a b
                    z       exact a/gaussian a b/flat a b
                    t       exact a/gaussian a b/flat a b
                    e       exact a/gaussian a b/flat a b
                    phi     exact a/gaussian a b/flat a b
                    theta exact a/gaussian a b/flat a b
                    polx    exact a
                    poly    exact   a
                    polz    exact   a
```

etc.

Example 1:
The following primary file would generate 10 events of 3 muons each of them originating from the point (0,0,-5) at time t=0. All muons have an energy of 1GeV, an angular spread of 5 degrees around the z-axis and a polarization of (1,0,0).

```
================================================================
#NumberOfEvents    10
#Primary       NumberOfParticles   3
                    ParticleType            13
                    x       exact   0
                    y       exact 0
                    z       exact   -5
                    t       exact   0
                    e       exact   1
                    phi     flat    0 360
                    theta flat      -5 5
                    polx    exact   1
                    poly    exact   0
                    polz    exact   0
================================================================
```

Example 2:
The following primary file would generate 10 events consisting of 1 muon and 2 electrons. Each muon originates from (-1,-1,-5) at time t=0s, has a momentum of 1GeV in the z-direction and has a polarization vector (1,0,0). Each electron originates from a random position in the square -2<x<2, -2<y<2 and z=-5 at time t = 0.0001s. The positions are distributed uniformly. Each electron has an energy of 4.5GeV also in the z-direction with a polarization vector (1,0,0).

```
================================================================
#NumberOfEvents    10
```

```
#Primary      NumberOfParticles  1
                                 ParticleType          13
                                 x       exact   -1
                                 y       exact  -1
                                 z       exact   -5
                                 t       exact   0
                                 px      0
                                 py      0
                                 pz      1
                                 polx    exact 1
                                 poly    exact   0
                                 polz    exact   0
#Primary      NumberOfParticles  2
                                 ParticleType          11
                                 x       flat     -2       2
                                 y       flat  -2 2
                                 z       exact   -5
                                 t       exact   0.0001
                                 e       exact   4.5
                                 phi     exact   0
                                 theta exact 0
                                 polx    exact 1
                                 poly    exact   0
                                 polz    exact   0
================================================================
```

7.4 Analysis interface manual

General explanation

The analysis file contains all of the information about the exact pixel structure of the chips in the detector. This information is used by the pixelmanager class to convert the pattern of energy depositions in the detector to an actual hit pattern on the chips. In order to accomplish this the program executes the following actions.

First it determines for all of the hit objects in the hitarray the exact pixel that they occured in. Next it constructs the so called frames. A frame is an object that contains a layer number, chip name, start time, end time, event number and a framepixelarray that in turn contains framepixel objects that consist of a x, y and energy deposition value. These frames can be considered as pictures of the hit pattern at a given time taken by a certain chip. Subsequently a number of noise pixels is added to the framepixelarray of each frame according to a Poisson distribution. And finally the discriminator function of the focalframe class is applied. If multiple hits occured on a single pixels this function will add their energy depositions. In addition it checks for all the framepixel objects whether their energy deposition exceeds the discriminator setting of the relevant column. If this condition isn't met by a framepixel object it will be removed from the framepixel array. Finally the array containing the frame objects is saved.

This is a very concise description of the functioning of the program. I believe it is important to be a bit more specific about the way the frames are constructed prior to moving on the exact explanation on the construction of an analysis file. The construction of the frames is namely approached in a quite specific manner. It is not merely a matter of picking all the hits that occurred between the start and end time of a frame. The MIMOSA chips are namely read out using a so called rolling shutter mechanism. This mechanism reads out one row at a time. So all the pixels on a row are read out simultaneously, after which the following row is read out. Given this mechanism a scenario can occur where the rolling shutter is halfway through its cycle when a shower thus a hit pattern occurs on a chip. All the hits in the chip of a single shower occur almost simultaneously compared to the read out time of a single row. So in this scenario first one half of the hit pattern will be stored in the frame that is constructed at that time and the other half of the hit pattern will present itself in the subsequent frame. In order to take this mechanism with its inherent effects into account the program determines a so called 'hitdeterminator' value for each of the hits which is a function of the space-time coordinates of the hits. This hitdeterminator then determines to which frame the hit belongs. Finally it is important to mention that the rolling shutter starts rolling on row 0 at the exact time of the earliest hit in the entire hit array.

Constructing an analysis file

As mentioned previously the analysis file contains the information about the exact pixel structure of all of the chips. The analysis file only makes use of the #Chip command. This #Chip command is followed by all the information of a certain chip. The entire format of a chip command is as follows:

#Chip layernr chipname xnrpixels ynrpixels xpixelwidth(cm) ypixelwidht(cm) noiserate(average noise pixels per frame) readouttime(s) discriminatorsetting(deposited energy keV) layernr

The layer number is the number of the layer that contains the chip. This layer number should correspond a layer number of a sensitive volume as defined in the geometry file. From here on i'll use the terms chip and sensitive volume interchangeably, since obviously only hits inside the sensitive volumes are saved and can therefore function as chip volumes.

chip name
Is the name of the sensitive volume in the layer with layernr as defined in the geometry file. Using the layernr and chip name a certain sensitive volume is determined uniquely. Make sure that all sensitive volumes with the same layernr have different volume names in the geometry file.

xnrpixels
First of all it's important to note that in the analysis framework the sensitive volumes are assumed to be boxes of which the origin is located in a corner in such a way that the volume is contained in the positive xy-plane. This is important since the x pixel coordinate is calculated by dividing the x-coordinate in the coordinate frame of the sensitive box by the pixel width in the x-direction (xpixelwidth, see below). If you do not define the sensitive volumes in this way the hit patterns on the chips will not be calculated correctly. Row 0 is the row that borders on the y-axis of the origin, see picture below.

ynrpixels
First of all it's important to note that in the analysis framework the sensitive volumes are assumed to be boxes of which the origin is located in a corner in such a way that the volume is contained in the positive xy-plane. This is important since the y pixel coordinate is calculated by dividing the y-coordinate in the coordinate frame of the sensitive box by the pixel width in the y-direction (ypixelwidth, see below). If you do not define the sensitive volumes in this way the hit patterns on the chips will not be calculated correctly. Column 0 is the row that borders on the x-axis of the origin, see picture below.

xpixelwidth
This is the width of a pixel row in centimetres (size in x direction). Assuming all pixel rows have the same width.

ypixelwidth

This is the width of a pixel column in centimeters (size in the y direction). Assuming all pixel columns have the same width.

noiserate
Is the average of the poisson distribution that determines the number of noise pixels per frame for each frame of that specific chip. At the moment the noise pixels are just added to the frame after discrimination, so the effect of noise pixels pushing small energy depositions of certain hits over the discriminator threshold is not taken into account yet.

readouttime
Is the time in seconds it takes the rolling shutter to finish one full cycle, which corresponds to one readout of the entire chip and thus to one frame. For further explanation of the rolling shutter mechanism see the general explanation above.

discriminatorsetting
The discriminator setting can occur in 2 formats. The first format is just the word 'default'. When you set the discriminatorsetting to default all of the columns will have a discriminator threshold of 4keV of deposited energy, which is approximately 0.5MIP a 30 micron silicon layer. However you can also define a specific discriminator setting for each of the individual pixel columns. This is done by a row containing ynrpixels(see above) entries. The unit of these entries are automatically in keV.

If the origin of a sensitive volume is positioned correctly we have the following situation:

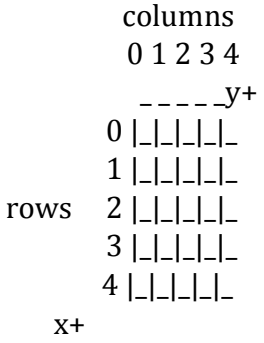

Example1:
In the following example we defined the readout features of a hypothetical detector that consists of 2 layers. Each layer contains 4 chips that are named chip1, chip2, chip3 and chip4. All the chips have 320 pixel rows and 320 pixel columns. All the pixels in these 2 layers are 0.006x0.006cm in size and are readout in 0.0001 seconds. Finally on average per chip we have 3 noise pixels per frame and the discriminator setting for all of the columns equals the default value of 4E-6 GeV.

==========

#Chip 0 chip1 320 320 0.006 0.006 3 0.0001 default

#Chip 0 chip2 320 320 0.006 0.006 3 0.0001 default
#Chip 0 chip3 320 320 0.006 0.006 3 0.0001 default
#Chip 0 chip4 320 320 0.006 0.006 3 0.0001 default
#Chip 1 chip1 320 320 0.006 0.006 3 0.0001 default
#Chip 1 chip2 320 320 0.006 0.006 3 0.0001 default
#Chip 1 chip3 320 320 0.006 0.006 3 0.0001 default
#Chip 1 chip4 320 320 0.006 0.006 3 0.0001 default
==========

Example2:
In the following example we defined the readout features of a hypothetical detector that consists of 3 layers. Each layer contains 2 chips that are named chip1 and chip2. All the chips have 320 pixel rows and 320 pixel columns. All the pixels in the chips are 0.1x0.1cm in size and are readout in 0.0001 seconds. On average we have 3 noise pixels per frame for every chip. Finally in this example we defined unique discriminator settings for each of the 10 columns per chip. ==========
#Chip 0 chip1 10 10 0.1 0.1 3 0.0001 4.4 3.2 8.8 7.6 5.4 5.1 8.5 4.5 3.4 9.1
#Chip 0 chip2 10 10 0.1 0.1 3 0.0001 8.5 2.6 3.4 7.5 4.6 8.1 2.1 5.8 6.2 6.3
#Chip 1 chip1 10 10 0.1 0.1 3 0.0001 1.4 4.5 2.5 8.6 9.2 4.3 3.2 1.2 5.3 4.4
#Chip 1 chip2 10 10 0.1 0.1 3 0.0001 2.2 3.5 8.2 6.3 2.3 1.4 2.4 5.7 1.2 3.1
#Chip 2 chip1 10 10 0.1 0.1 3 0.0001 8.8 2.9 3.9 1.8 2.5 4.3 7.3 6.2 5.3 1.5
#Chip 2 chip2 10 10 0.1 0.1 3 0.0001 5.2 3.6 5.5 4.6 2.5 2.8 6.8 7.3 2.9 5.6
==========

7.5 Draw interface manual

#DrawDetector
Draws the detector geometry, useful feature during the construction of your geometry. Just run the simulation for a single simple event and use this command to draw the detector for inspection.

#DrawTracksPhotons eventnr
Draws in the detector geometry all the tracks including de photon tracks that are usually great in number effectively obscuring the other tracks. Eventnr is the number of the event of which the tracks are drawn, the count always starts at 0.
blue = photon track
yellow = muon track
red = electron track
green = positron track
black = other particle track

#DrawTracksNoPhotons eventnr
Draws in the detector geometry all the tracks excluding the photon tracks that are usually great in number effectively obscuring the other tracks. Eventnr is the number of the event of which the tracks are drawn, the count always starts at 0.
blue = photon track
yellow = muon track
red = electron track
green = positron track
black = other particle track

#DrawTrackHits eventnr
Draws the detector geometry in addition to all the locations of the energy depositions in the sensitive volumes. Eventnr is the number of the event of which the hits are drawn, the count always starts at 0.

#DrawEnergyDepositionsLayers layerbegin layerend eventnr
Draws the location of all of the energy depositions that occurred in the layers with a layer number between layerbegin and layerend of event with number eventnr. The locations are drawn in a 2D graph and the coordinates are the MARS reference frame (see geometry manual).

#DrawEnergyDepositionsLayer layernr event
Draws the location of all of the energy depositions that occurred in the layer with layer number layernr of event with number eventnr. The locations are drawn in a 2D graph and the coordinates are the MARS reference frame (see geometry manual).

#DrawAllFrames eventnr
Draws all the frames that were constructed by the pixelmanager class for the event with number eventnr. A frame is a 2D plot of all the hit pixels of a single read out of a single chip. A frame can be identified by it's event number, layer number, chipname and start time of the read out (see also the analysis manual for more detailed info on the precise readout mechanism involving the rolling shutter).

#DrawChipFrame eventnr starttime endttime layernr chipname
Draws the sum of all the frames with starttime between starttime and endttime that occurred in the chip with chipname in layer with number layernr. A frame is a 2D plot of all the hit pixels of a single read out of a single chip. A frame can be identified by it's event number, layer number, chipname and start time of the read out (see also the analysis manual for more detailed info on the precise readout mechanism involving the rolling shutter).

#DrawChipFrames eventnr starttime endtime layerbegin layerend chipname
Draws the sum of all the frames with a start time between starttime and endttime that occurred in the chip with chipname in layer with number between layerbegin and layerend. A frame is a 2D plot of all the hit pixels of a single read out of a single chip. A frame can be identified by it's event number, layer number, chipname and start time of the read out (see also the analysis manual for more detailed info on the precise readout mechanism involving the rolling shutter).

EXAMPLE:

_____

#DrawDetector

#DrawTracksPhotons 0
#DrawTracksNoPhotons 0
#DrawTrackHits 0

#DrawTracksPhotons 1
#DrawTracksNoPhotons 1
#DrawTrackHits 1

#DrawEnergyDepositionsLayers 0 23 0

#DrawEnergyDepositionsLayer 12 0
#DrawEnergyDepositionsLayer 13 0
#DrawEnergyDepositionsLayer 14 0
#DrawEnergyDepositionsLayer 15 0

#DrawAllFrames 0

#DrawChipFrame 0 0 0.0001 15 chip0

#DrawChipFrames 0 0 0.0001 0 23 chip0
#DrawChipFrames 0 0 0.0001 0 23 chip1
#DrawChipFrames 0 0 0.0001 0 23 chip2
#DrawChipFrames 0 0 0.0001 0 23 chip3
